Bio-Inspired Morphing Aircraft Mechanisms and Applications on Soaring Bat Wing Aerodynamics

by Justin Edward Manzo

BIO-INSPIRED MORPHING AIRCRAFT MECHANISMS AND APPLICATIONS ON SOARING BAT WING AERODYNAMICS

A Dissertation

Presented to the Faculty of the Graduate School

of Cornell University

In Partial Fulfillment of the Requirements for the Degree of

Doctor of Philosophy

by

Justin Edward Manzo

August 2010

BIO-INSPIRED MORPHING AIRCRAFT MECHANISMS AND APPLICATIONS ON SOARING BAT WING AERODYNAMICS

Justin Edward Manzo, Ph. D.

Cornell University 2010

Recent advances in smart materials have allowed for the design of low-profile actuators suitable for use in aerospace structures. In conjunction with these innovations, aerodynamic modeling tools have afforded designers new insights into the advantages of changing a platform's geometry while in flight, in order to better adjust aerodynamics to meet instantaneous mission requirements. This type of gross adaptation, known as morphing, forms the basis for the research presented in this dissertation. Sources of inspiration for new airframe designs come from biological examples such as bird and bat wing planforms.

The first chapter of this dissertation focuses on the development, modeling, and fabrication of a morphing wing mechanism inspired by shore bird morphology. In this work, wing morphing using shape memory alloy actuators is achieved, and aerodynamic performance is tested experimentally. The actuator used in this work is designed for a finite number of energetically inefficient cycles, and is intended to prove out the concept of employing smart materials to effect gross shape change.

The next chapter examines the advantages of bat wing morphology across various species and planforms. A study on bat wing aerodynamics suitable for use in man-made structures takes advantage of heuristic optimization to illustrate that through

morphing, significant enhancements in lift and lift-to-drag ratio can be achieved.

The final three chapters of this work focus on the development of an actuator system suited to integration onto the aforementioned morphing platforms, incorporating a passive rigidity in order to reduce energy loss during and after wing morphing. The third chapter presents a preliminary model on the active rigidity joint, outlining basic principles of operation, key materials, and correlation with finite element results in predicting deflection behavior. The fourth chapter expands this model, allowing for more accurate prediction of joint behavior under loading and with arbitrary geometry. It also employs heuristic optimization to develop a thorough understanding of expected joint performance over all geometric configurations. The fifth and final chapter describes joint fabrication and experimental results, showing agreement with the analytical model of chapter four under particular conditions.

BIOGRAPHICAL SKETCH

Justin Manzo received a Bachelor's of Science degree in Mechanical Engineering from Cornell University in 2003. He went on to pursue a Master of Science there, also in Mechanical Engineering. As an undergraduate, he concentrated in robotics, founding the Cornell University Battlebots team.

Justin joined the Laboratory for Intelligent Machine Systems, directed by Prof. Ephrahim Garcia, in 2003. During the same year, he was admitted into the Graduate Student Research Program at NASA Langley Research Center, receiving a four-year fellowship for work on morphing aircraft mechanisms and biologically-inspired design. As part of this program, he worked at NASA Langley during the summers of 2003-2006 in the Dynamics & Controls Branch, under the advisement of Drs. Lucas Horta and Garnett Horner. In May 2006, he received a Master of Science degree in Aerospace Engineering for his research entitled "Analysis and Design of a Hyper-Elliptical Cambered Span Morphing Aircraft Wing".

Justin focused his subsequent research on bat inspired wing shapes and appropriate shape change mechanisms, conducting research on biological specimens in conjunction with the Syracuse Zoo, and drafting a paper on bat-inspired aerodynamics for the Journal of Aircraft. In 2006, Justin was featured on Animal Planet's *Chasing Nature* for his work with biologically-inspired robotics. From 2007 through 2010, Justin served as a teaching assistant trainer for the Office of Engineering Learning Initiatives. During this time, he was awarded the Lead Teaching Assistant Trainer Fellowship from 2008 through 2010, where he focused on promoting active learning techniques and effective presentation skills in the classroom.

Justin was responsible for developing an analytical model and subsequent prototypes of an induced strain actuator suitable for use in biologically inspired shape changing wing mechanisms. He combined aerodynamics, structural modeling, and thermal modeling in an interdisciplinary program to design and build a morphing bat wing aircraft, which he leaves behind in a prototype stage. During his doctoral studies, Justin co-authored one published paper in the Journal of Aircraft, published two papers in Smart Materials and Structures and submitted a third, and published one paper in the Journal of Intelligent Material Systems and Structures.

To all of the people who made ten years in Ithaca that much more enjoyable.

ACKNOWLEDGMENTS

First and foremost, I would like to thank my advisor , Dr. Ephrahim Garcia, for getting it into my head that I could pursue a doctorate. Second, I would like to thank my labmates Dr. Adam Wickenheiser, Tim Reissman, and John Dietl, whose assistance was invaluable, intellect unparalleled, and combined time in graduate school rivaling my age upon departure. I would like to thank Jason Harris for teaching me the foundations for what would later become a career. I would like to acknowledge Dr. Garnett Horner (rtd.) and Dr. Lucas Horta of the Structural Dynamics branch of NASA Langley for their guidance in developing a research direction and for fellowship support under NASA Graduate Student Research Program (GSRP) grant NGT-1-03021. I would also like to thank Jason Hermiller and Ernie Havens of Cornerstone Research Group, as well as Jeff Brown of Dynalloy, for fielding technical questions as well as granting us access to their products and services. In addition, I would like to thank my excellent fellow researchers over the years – Emily Leylek, Franklin Geeng, Nidhi Rathi, Richard Callahan, and Lee Morgan – without whom I would have undoubtedly still been a perpetual graduate student. I would like to express my gratitude to our department house-moms Nanette Peterson and Marcia Sawyer for supporting me every step of the way, including seeing enough potential to let me transfer in from another department. Finally, I would like to thank my Teaching Assistant Training staff at the Office of Engineering Learning Initiatives, specifically Linda Tompkins and her team, who taught me that being a teacher can, in fact, be fun. May you all live a thousand years.

TABLE OF CONTENTS

LIST OF FIGURES

CHAPTER 1

CHAPTER 2

CHAPTER 3

CHAPTER 5

LIST OF TABLES

CHAPTER 5

CHAPTER 1

DEMONSTRATION OF AN IN SITU MORPHING HYPER-ELLIPTICAL CAMBERED SPAN (HECS) WING MECHANISM[1]

1. Abstract

Research on efficient shore bird morphology inspired the hyper-elliptical cambered span (HECS) wing, a crescent-shaped, aft-swept wing with vertically oriented wingtips. The wing reduces vorticity-induced circulation loss and outperforms an elliptical baseline when planar. Designed initially as a rigid wing, the HECS wing makes use of morphing to transition from planar to furled configuration in flight, similar to a continuously curved winglet. A morphing wing concept mechanism is presented employing shape memory alloy actuators to create a discretized curvature approximation. Aerodynamics for continuous wing shapes are validated quasi-statically through wind tunnel testing, showing enhanced planar HECS wing lift-to-drag performance over an elliptical wing, with the furled HECS wing showing minimal enhancements beyond this point. Wind tunnel tests of the active morphing wing prove the mechanism capable of overcoming realistic loading, while further testing may be required to establish aerodynamic merits of the HECS wing morphing maneuver.

2. Introduction

Only three vertebrate groups throughout evolution have developed flight as a primary means of locomotion – bats, birds, and pterosaurs. Evolved wings manipulate lift

[1] From Manzo, J. and Garcia, E., "Demonstration of an *in situ* morphing hyperelliptical cambered span wing mechanism"; reprinted by permission of the Institute of Physics, Inc.

forces and minimize drag using passive and active elements – either full-time advantageous devices, or morphing elements that can be called upon on demand in order to drastically alter flight characteristics to suit flight requirements.

The evolved flight abilities of birds provide insight into improvements on fixed wing aircraft, inspiring aircraft design since the Wright Brothers' 1905 wing warping flier, which employed active camber and twist changes. Many studies have been conducted on avian wings for applications to engineering, from replicating wing geometry (Liu *et al.*, 2004) to developing morphing vehicles with the ability to modify sweep, dihedral (Abdulrahim and Lind, 2004), chord, twist (Majii *et al.*, 2007), and even span changes (Blondeau and Pines, 2004; Love *et al.*, 2004). Even ornithopters have allowed engineers to take to the sky through careful study of aeroelasticity, periodic thrust and lift cycles, and unsteady transient fluid dynamics (Delaurier, 1999; Dietl and Garcia, 2008).

Research at NASA Langley has been investigating natural morphologies through the Morphing Aircraft Structures (MAS) program to create multiple, efficient geometries on single airframes (Siochi *et al.*, 2002; Wlezien *et al.*, 1998). One candidate wing shape is the Hyper-Elliptical Cambered Span (HECS) wing modeled on the albatross, a soaring bird with high lift-to-drag ratio (Lazos, 2005). In passive rigid wing analysis, the HECS wing has two configurations of the same span, one with a planar shape and one with downward pointing wingtips (with increased surface area due to the extension in total arc length) similar to a blended winglet. Due to its beneficial aerodynamic properties, the HECS wing was chosen as a testbed structure for vehicle morphing (Manzo *et al.*, 2004), in which a mechanism changes wing shape in flight from planar but aft-swept planform to the positive anhedral 'furled' wing shape, as in

Figure 1.1, allowing both aerodynamic regimes in flight. Unlike the initial studies of Lazos, the morphing wing of this research preserves wetted surface area and arc length at the expense of wingspan and planform area during shape change, a deviation from the initial study where span constant between planar and furled wings as in Liersch *et al.* (2009). With this type of morphing maneuver, the HECS wing transitions from planar to furled state with a span decrease of 14%, an 8% decrease in projected area, and a 20.7% decrease in aspect ratio.

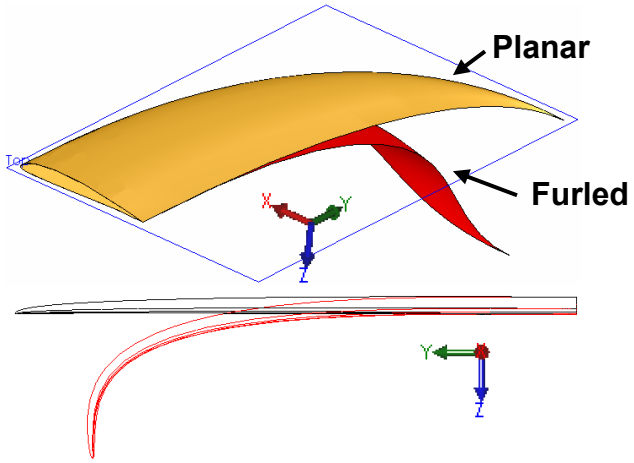

Figure 1.1 - Planar (flat) and furled (downward pointing tips) HECS wings

The aerodynamics of the HECS wing are addressed without implementation of shape change devices in Section 3. An experimental study on continuous wings, conducted quasi-statically in the wind tunnel, compares snapshots of wing performance before morphing is implemented. With an understanding of expected lift and drag for each wing shape, a mechanism proposed in Section 4 is implemented on a wing subjected to aerodynamic loads to demonstrate effectiveness. Feedback control is used to increase the response speed of the shape memory alloy-based actuator system, allowing for collection of and control over wing shape and gross aerodynamic regime. While the HECS wing aerodynamics in the morphed configuration may not be optimal

for airframe design, the shape change concept mechanism yields successful results with applications to future morphing maneuvers.

3. Aerodynamics and Motivation

Many biological flight mechanisms provide inspiration for improvements in aircraft performance. For example, a bird's wingtip feathers ('primaries') are used to alleviate tip vortex shedding, reducing total wing drag by 12% by spreading the wing vortex wake more evenly along the wing (Tucker, 1993). These primaries are also canted slightly downwards in order to produce a slight degree of lift in the direction of thrust, which might be sufficient to overcome the induced drag component of total wing drag (March *et al.*, 2005). Flow visualization has confirmed that spreading the tip feathers will greatly reduce the vorticity trailing from the wingtips, as was validated experimentally on a retrofitted Cessna Centurion when rigid tip 'feathers' (Spillman, 1987). This method of drag reduction has been one motivation for the development of winglets (Whitcomb, 1976), which increase the effective span of a wing. Increased effective span occurs when the vertical endplates reduce wingtip vortex intensity by forming a physical barrier to vortex roll-up, decreasing drag and also preventing significant lift losses.

Building on these and other drag studies, the HECS wing arose from study on induced drag at NASA Langley (Lazos, 2005). Based on crescent-shaped planar wing theory (Burkett, 1989; Van Dam, 1987) and nonplanar lifting systems (Cone, 1963), the claim was made that the lift-to-drag ratio of the crescent-shaped HECS wing with tips pointed downwards (as in Figure 1.1) could exceed that of an elliptical wing by up to 15% with only a 10% increase in surface area for a given span. This is due to the

alteration of the trailing vortex sheet away from the lifting plane wing to reduce induced drag as predicted by inviscid, potential flow theory. One of the principal drag components on a lifting system is induced drag, caused when lift forces not fully perpendicular to the free stream air velocity create an additional drag component. The angle of this deviation is the induced downwash angle, affected by wingtip vortices as well as vehicle angle of attack, α. Induced drag can account for as much as 50% of total cruising aircraft drag (Henderson and Holmes, 1989), so evolutionary solutions to this problem provide new inspirations for efficient man-made wings. Based on induced drag studies compiled by Henderson and Holmes (1989) and Rokhsaz (1993), the HECS wing was modeled on the soaring albatross shape for two reasons. First, the crescent-like shape of the planar HECS wing is highly effective at reducing induced drag. From Munk (1923) and later Cone (1962), induced drag is related to a wing's spanwise efficiency of the wing in the form:

$$C_{Di} = \frac{1}{e\,\pi\,AR}\frac{C_L^2}{}, \tag{1}$$

where C_L is wing lift coefficient and AR is wing aspect ratio. The spanwise efficiency factor e traditionally assumes a maximum of 1, found with an elliptical wing using planar vortex wake assumptions (Munk, 1923). However, this parameter can increase above unity for crescent-shaped planar wings (Van Dam, 1987; Burkett, 1989). Second, the spanwise efficiency factor is increased with nonplanar wings morphed at the tips, effectively yielding a winglet of continuous curvature. Similar to the use of endplates already mentioned, HECS morphing decreases induced drag by reducing tip vortex effects. The continuous HECS curvature experiences less total drag than a pure winglet in previous testing (Lazos and Visser, 2006), and is akin to blended winglets found on the Boeing Business Jet and the 737-800, which avoids interference drag

penalties due to less discontinuity at the winglet interface (Faye *et al.*, 2002). Equation (1) also indicates that preservation of planar HECS span and aspect ratio is critical when considering this effective winglet as noted in Manzo *et al.* (2005), though this geometry change would be impractical, requiring extension of the crescent-shaped span along with anhedral curvature. Instead, constant arc length HECS studies on morphing are readily found in the literature, with a geometry change that yields effects beyond induced drag reductions. These effects and studies are discussed at the end of Section 3.3 and the beginning of Section 4.

The HECS wing realizes shape enhancements by using hyperelliptical (ellipsoid raised to a power greater than 2) leading and trailing edge distributions in the planar state, bending the wings in theater into a nonplanar hyperellipse curve along the span according to the equations:

$$\left(\frac{9.522-x}{9.522}\right)^{2.5}+\left(\frac{y}{15.121}\right)^{2.5}=1 \tag{2}$$

$$\left(\frac{4.727-x}{4.727}\right)^{2.5}+\left(\frac{y}{15.121}\right)^{2.5}=1 \tag{3}$$

$$\left(\frac{z+3.884}{3.884}\right)^{3.5}+\left(\frac{y}{13}\right)^{3.5}=1 \tag{4}$$

for leading edge, trailing edge, and spanwise furl, respectively, with the standard aircraft coordinate system as shown in Figure 1.1. Equations (2)-(4) correspond to a wing of planar span 30.2" and furled span 26", and can be scaled to match desired vehicle configurations. They represent a slight change from the work of Lazos (2005) by accentuating the furled hyperellipse, providing a larger fraction of the original span as a downward pointing wingtip through morphing. Distinct from Lazos' work, the

HECS wing studies presented in this paper deal with a constant arc length and wetted area approach as opposed to constant span between shapes, as the wing transitions between its two geometric configurations by bending without elongation. This is a much more physically attainable morphing maneuver, and forms the basis of mechanism study.

The wing morph follows avian morphological changes for different flight regimes as opposed to rigid, furled wings with downward-pointing wingtips. In avian gliding, maximum span should be used for maximum performance to a critical speed, but above this critical speed span decreases for best lift-to-drag ratio. The highest overall ratio for each bird, however, always occurs below the critical speed (Tucker, 1987). Allowing wings to decrease span through furling allows for different performance regimes at different flight speeds, as well as the ability to change the amount of available lifting surface for various mission parameters.

The airfoil used on the HECS wing is the Selig-Donovan 7032, which has 3.66% camber and 9.95% maximum thickness. This airfoil was designed for thermal-duration sailplanes, similar in contour to the commonly used NACA 4410 or more common NACA 4412 (Figure 1.3), though optimized for low Reynolds number flight more than either NACA airfoil. Airfoil data for the SD 7032 is based on experimental results conducted by the designer (Selig *et al.*, 1989; reprinted Simons, 1999) at a Reynolds number flow of 100,000-200,000, with minor differences between these two regimes in terms of lift or drag coefficient. Presented in Figure 1.2, the SD 7032 airfoil demonstrates comparable drag and noteworthy lift characteristics when compared to the NACA 4412, based on experimental data for low Reynolds number flows of 75,000-200,000 (Lnenicka, 1974; reprinted Simons, 1999). The SD 7032 has

a peak lift coefficient of approximately 1.3 at low speeds associated with 100,000 Reynolds number flow, compared with 1.15-1.2 for the NACA 4412 for similar flows.

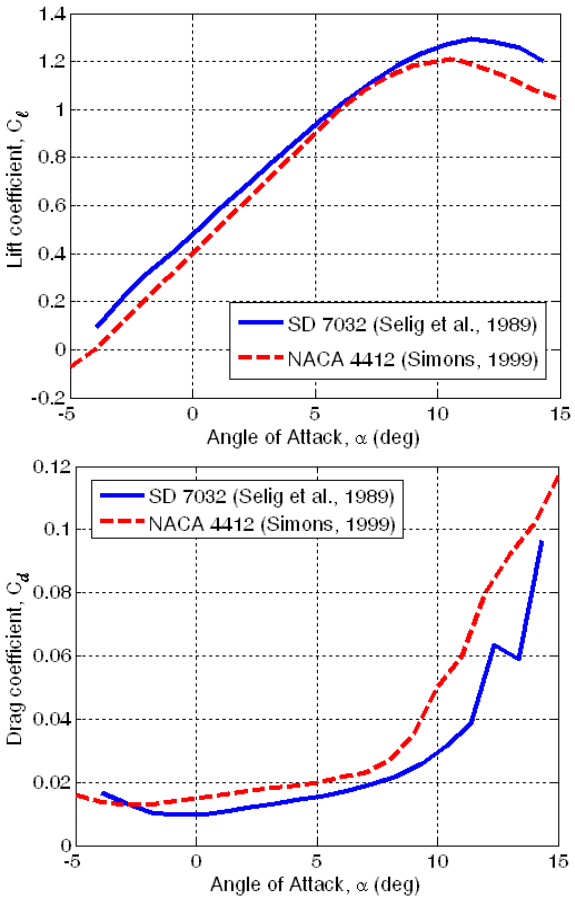

Figure 1.2 – Airfoil data for SD 7032 used on HECS wing and NACA 4412 at Reynolds numbers of 200,000 and 250,000, respectively. Lift (left) and drag coefficient (right). Data from Simons (1999) and Selig *et al.* (1989).

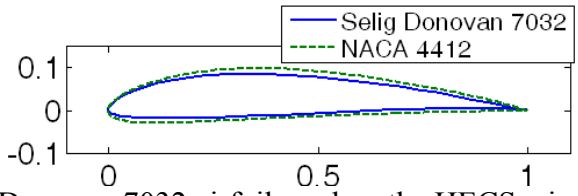

Figure 1.3 - Selig-Donovan 7032 airfoil used on the HECS wing, and NACA4412 airfoil of similar geometry

Because the effects of aft swept curvature and cambered span (continuously curved dihedral) strongly influence the trailing vortex wake, analytical results using lifting line methods (Wickenheiser and Garcia, 2007) are limited in their ability to confirm the theory of Burkett and the results of Lazos and Visser (2006), in part due to their restriction to prescribed planar vortex wakes. As a result, preliminary analyses of the wings compute induced drag coefficients that do not match theoretical expectations. Merits of the HECS wing stem from combination of crescent-like efficiencies with the nonplanar ellipsoid arcs due to furling pushing the trailing vortex wake from the lifting line while minimizing its intensity, akin to the use of vertical wingtips in use today (Whitcomb, 1976) but with more rounded curvature. These merits are best seen through experimental study.

3.1. Experimental Rigid Wing Test Setup

Aerodynamic properties of the HECS wing were tested quasi-statically in the Cornell University Environmental Wind Tunnel facility. This open circuit tunnel has a test section 10 feet long, with a closed rectangular cross section of geometry 48" wide by 43.5" high. Nominal velocity capabilities are 7.5 to 75 mph, controlled by six 15 HP axis-flow fans with variable inlet guide vanes. The tunnel has a turbulent intensity of up to 2% at moderate speeds. Maximum tunnel blockage was 5%, accounting for a dynamic pressure drop well below 0.01% based on the simplified method for blockage effects presented in Rae and Pope (1984). The test specimens for rigid wings were made of ABS plastic generated on a Dimension Stratasys rapid prototyping machine, and were mounted in the upright configuration with sufficient clearance from the tunnel boundary layers. Three wings were tested - the planar and furled HECS wing shapes, along with an elliptical wing of identical surface area and aspect ratio to the

planar HECS wing - to compare the HECS wing morphed and unmorphed snapshots against both each other and the elliptical wing baseline. The three wings were all constructed with Selig-Donovan 7032 airfoil for consistency, and were finished to the same surface quality. Load data was extracted using a JR3 six axis robotic load cell with accuracy of at least four decimal places. The experimental setup is shown in Figure 1.4.

The wingspan is 32" for the elliptical and planar HECS shape and 27.5" for the furled wing (preserving arc length due to morphing from planar to furled), representing a rescaling of 105.8% scale of outside research and Equations (2)-(4). The elliptical wing chord length and quarter-chord distribution is described by

$$c(y) = \frac{S_{HECS}}{\pi\, b_{HECS}} \sqrt{1 - \left(\frac{2y}{b_{HECS}} \right)^2} \tag{5}$$

$$c_{1/4}(y) = 0 \tag{6}$$

such that spanwise lift distribution is elliptical given the linear quarter-chord line. The tunnel tests are run at a wind speed of 23-24 mph, corresponding to Reynolds number flows between 90,000 and 100,000 at the wing root and tapering out along the span. Relevant geometry parameters are summarized in Table 1.1, matched to the wings shown in Figure 1.4. Planform area is equivalent for the elliptical and planar HECS model, while the furled HECS wing planform is reduced by 8.2% from the other models, accompanying the 14% span change mentioned earlier while preserving wetted surface area, S_{WET}. This reduced planform area is used in the nondimensional analysis of the furled HECS wing, which can be a deceptive value if considered independent of morphing change. Because morphing is concerned with a single

vehicle, lift coefficients appear similar in presented results, although wings will experience a lift force change. Regardless, dimensionless coefficients provide the most useful description of wing behavior, and remain scaled by their respective planform areas and spans.

Table 1.1 - Geometry parameters for three rigid wings tested, all with SD7032 airfoil cross-sections

Wing Model	Span	Planform Area, S	MAC	Wetted Area, S_{WET}
Elliptical	32”	136.4 in^2	4.61”	273.6 in^2
HECS, Planar	32”	136.4 in^2	4.47”	279.0 in^2
HECS, Furled	27.5”	125.3 in^2	4.63”	279.0 in^2

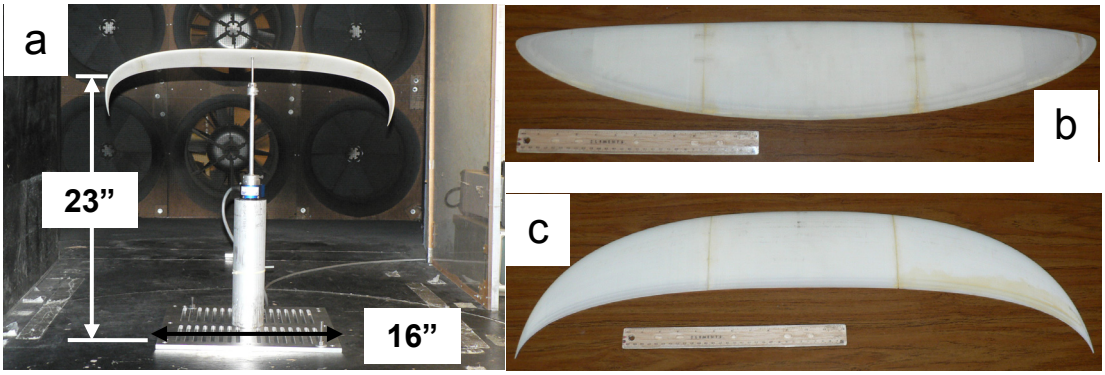

Figure 1.4 – Experimental setup of rigid wing testing in the Cornell University low-speed wind tunnel with installed furled HECS wing (a). Loads measured with JR3 load cell, shown at bottom, with high-intensity light (behind wing) removed during testing. Elliptical wing (b) and HECS planar wing (c) shapes with matched span also tested.

The data from the load cell was collected at 250 Hz and filtered using an eighth order Butterworth filter with the passband below 6 Hz to remove the effects of wind tunnel noise and mechanical vibrations measured by initial tests above 10 Hz. Experimental results are plotted with post-filtered 1-σ standard deviations, indicating statistically significant differences between the performance of the three wings tested. For lift-to-drag ratio, the standard deviation is found through statistical analysis to be:

$$\sigma_{L-D} = \mu_{L-D}\sqrt{\left(\frac{\sigma_L}{\mu_L}\right)^2 + \left(\frac{\sigma_D}{\mu_D}\right)^2} \tag{7}$$

3.2. Wind Tunnel Corrections and Limitations

Corrections are made for the dynamic pressure change due to area blockage, a function of frontal area exposed to flow in the tunnel. This modification has minor effects, but is included for rigor. More significant effects are based on the scaling of the wing relative to the tunnel. Due to a tradeoff between data resolution from the load cell and model accuracy from the prototyper at small scales, the wing has a span-to-tunnel ratio of 0.66. This introduces wall effects due to interference with the vortex wake, which can be corrected for under certain assumptions. A simplified method following Rae and Pope (1984) uses a wall effect correction factor based on the Glauert method, assuming a planar vortex arc for a wing with uniform loading in a closed rectangular tunnel of aspect ratio 0.9. This yields values of 0.14 and 0.147 for the boundary correction factor δ used in corrections for the planar wings and furled wing, respectively. Upwash angle, measured through calibration testing on an upright and inverted elliptical wing, is determined to be 0.29 degrees. This angle is added to the measured α, as well as used for adjustment to the measured drag values. The wing root is located 23" from the ground plane of the tunnel, yielding a height-to-span ratio of 0.84 for the furled wing and 0.72 for the planar wings. While no ground effect corrections are included, there may exist elevated lift and depressed drag values inherent in the data. While these calculations make broad assumptions regarding wing loading, vortex wake shape, and the impact of blockage and the vertical planes on aerodynamics, they provide some sense of data reliability. Drag corrections on the order of 0.5% and corrections for α of less than one degree with these methods

informs measurement uncertainty to within one or two percent error, coupled with up to a 3% windspeed measurement error and potential ground effect error. As such, performance changes between wings presented in Section 3.3 of less than 5% may not be statistically valid given the constraints of available tunnel facilities, though in this paper results exceed this threshold.

3.3. Experimental Rigid Wing Testing Results

By first comparing the planar HECS wing to the elliptical wing with HECS airfoil, the lift and drag data, non-dimensionalized to coefficients, is shown along with lift-to-drag ratio in Figures 1.5-1.7. The lift coefficient results demonstrate better performance for the experimental planar HECS wing compared to the elliptical wing over most angles tested, with a possible measurement error at 8 degrees α, accounting for the dip at that point. In terms of overall characteristics, the trends agree well with the theory of Burkett (1989) and Van Dam (1987), and show a strong similarity to the infinite wing airfoil data also overlaid. The results are plotted alongside a theoretical model for a finite span elliptical wing using an approximation following Katz and Plotkin (2001) for lift coefficient:

$$C_L = \frac{m_0}{1 + \frac{m_0}{\pi\, AR}}(\alpha - \alpha_0) \tag{8}$$

where m_0 is the lift curve slope with respect to α and is estimated from the SD 7032 airfoil data of Figure 1.2 to be 5.30 rad^{-1} over the linear range from -5 to 6 degrees, and AR is the aspect ratio as determined by the geometry given in Table 1.1.

Though the elliptical wing demonstrates reduced lift compared to the theoretical model, the similarities in fabrication and testing between elliptical and planar HECS wings are sufficient to conclude that the planar HECS wing is the superior of the two, showing a higher peak lift coefficient of 1.25 compared with 1.1 for the elliptical wing, a high stall angle of 15 degrees (though the elliptical wing is not yet stalled in presented results), and a lift improvement of around 0.1 for most pre-stall angles. The discrepancy from theory, as well as the offset with identical curvature between HECS airfoil and 3-D wing shapes, may serve as an indication of experimental error in precise measurement of the wing α as discussed in Section 3.2, although the error is within 1 degree. As well, the theoretical model is based on flat plate theory with a constant lift curve slope, which is only an approximation of the true airfoil behavior, and which doesn't take into account viscous effects. The linear assumption results in the discrepancy between theory and experiment for high α, but agreement for low α lends credibility to the experimental results, as the 2-D lift curve slope is based on observed flow at the appropriate Reynolds number. Other potential sources of experimental error may come from turbulence in the tunnel, fluctuating wind speed measurements with a documented measurement error of up to 3%, and oscillations of the wing as based on the single-point sting attachment. These oscillations will decrease laminar flow attachment, but were observed to have low amplitudes observed at around 15-20 Hz before filtering, and were believed to have only minor effects on the overall wing behavior.

As seen in Figure 1.6, the drag coefficients are comparable for both wings below 5 degrees α, above which the elliptical wing drag begins to increase faster than that of the HECS wing. This is in excellent agreement with the experimental findings of Lazos and Visser (2006) as well as Liersch *et al.* (2009), confirming the early

theoretical studies of Burkett (1989) and Van Dam (1987) which show that the induced drag can be significantly reduced by pushing the trailing vortex sheet below and away from the lifting surface, in turn decreasing the downwash angles over a significant portion of the wing by decreasing both the intensity and proximity of the tip vortices to the lifting line. Assuming the tunnel data to be an accurate reflection of ideal wing performance, the difference between the airfoil data and the finite 3-D wing data primarily represents the contribution of induced drag on the wing. This induced drag accounts for a large portion of the total wing drag; as such, a drag coefficient decrease of up to 50% appears between elliptical and planar HECS wing at the higher angles of attack. The error bars indicate that the drag improvement is again statistically valid, even given the noise and other sources of error in the tunnel mentioned above.

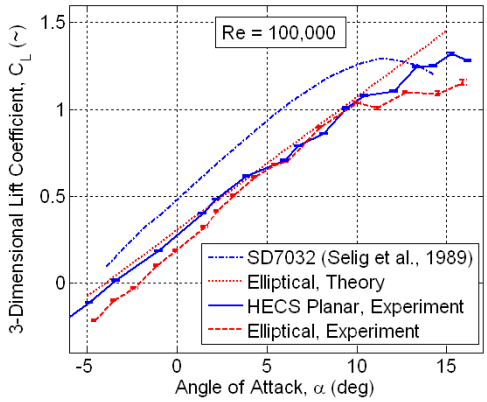

Figure 1.5 - Experimental lift coefficient for elliptical and planar HECS wing with flat plate model from Katz and Plotkin (2001) for elliptical finite wing and HECS wing airfoil (SD 7032) data

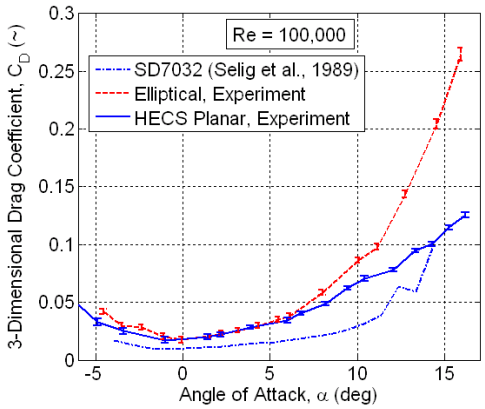

Figure 1.6 – Experimental drag coefficients for elliptical and planar HECS wings with HECS (SD 7032) airfoil

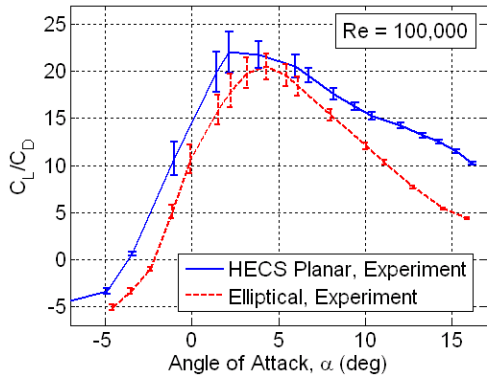

Figure 1.7 – Experimental lift-to-drag ratio for elliptical and planar HECS wing

As seen in the lift-to-drag ratio (Figure 1.7), the planar HECS wing outperforms the elliptical wing by a wide margin. Even with potential angle imprecision, the HECS wing reaches a maximum lift-to-drag ratio of approximately 22 compared with 20 for the elliptical wing in the range of 2-4 degrees α (±1 degree for combined angle discrepancy) for both wings. Above this range, HECS wing performance margins increase even further, with a lift-to-drag ratio over 10 at 15 degrees α, compared with 4-5 for the elliptical wing. Results confirm with strong statistical significance that the planar, aft-swept HECS wing outperforms the classically optimal elliptical wing with regard to both lift and induced drag - a significant contributor to total drag - and that

consequently the planar HECS wing yields higher lift-to-drag values over the full range of α.

For the furled HECS wing, nondimensional results demonstrate similar improvement over the elliptical wing compared to the planar HECS wing. Figures 1.8-1.10 show differences between furled and planar HECS experimental results, along with similar experimental results from NASA Langley (Lazos, 2005). Lift coefficients between furled and planar HECS wings are almost identical over the entire range tested, though slightly lower than results of outside experimentation. This overlap is surprising, given the 14% wingspan reduction when morphing from planar to furled wing shape. One explanation for this the trade-off between larger span when planar and more efficient wingtip effects when furled. When furled, span decrease is offset by the blended winglet effect, which moves tip vortices away from the lifting line and reduces their intensity more efficiently than with planar HECS shape alone. However, experimental similarity in lift coefficient indicates that lift forces experienced by the wing are lower when furled. Due mainly to increases in planform area and span, lift forces seen on the planar HECS wing are 8 to 10% higher than those of the furled HECS wing. Further testing may yield results in better agreement with Lazos (2005), presenting higher furled HECS wing lift coefficients than are seen in this work.

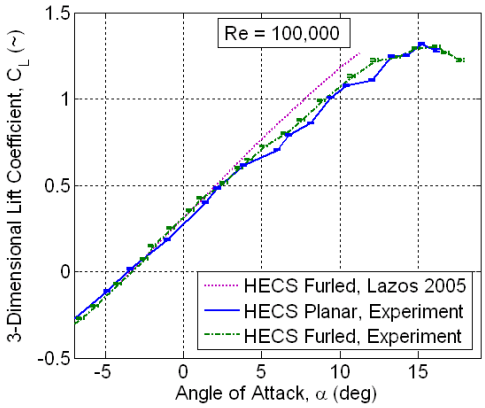

Figure 1.8 - Experimental lift coefficient for planar and furled HECS wings

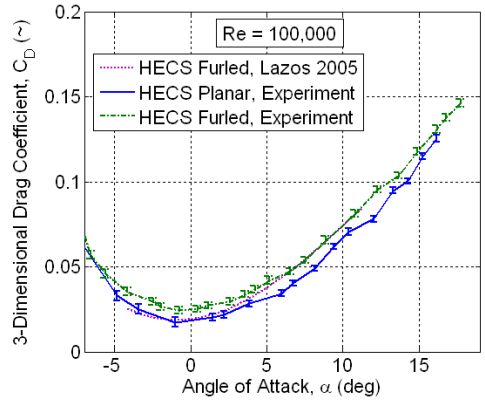

Figure 1.9 – Experimental drag coefficient results for planar and furled HECS wings

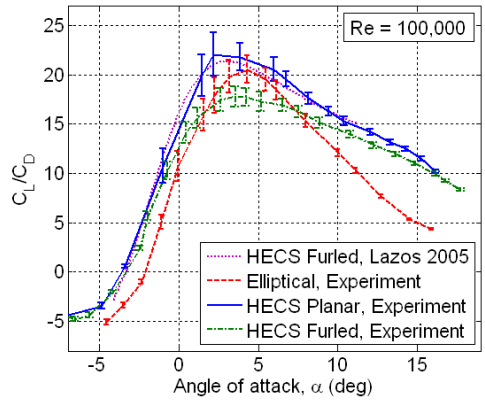

Figure 1.10 - Experimental results lift-to-drag ratio of all tested wings

Figure 1.9 shows furled HECS drag coefficient close to that of planar HECS drag over all angles tested, shifted higher by almost a constant value across all angles tested,

though still an improvement from the elliptical wing. More importantly, since planform area has also decreased by 8% when morphing to furled shape, actual drag forces are lower for the furled wing than for the planar HECS wing for higher angles of attack(crossover around 9 degrees α). This drag decrease comes with no change in wetted surface area, implying that the downward pointing wingtips are effective at decreasing induced drag at high angles of attack, though at the expense of lift force due to span decrease. Lazos (2005) presents lower drag coefficient values for the furled HECS wing than in this work at low angles of attack, most likely due to vortex reduction and migration effects away from the lifting surface discussed in a later paper (Lazos and Visser, 2006).

The results from all three rigid wing tests are presented in the lift-to-drag plot of Figure 1.10, showing valued realized in the Cornell wind tunnel along with those found through outside experimentation. While the results of the planar HECS wing shape and, above 7 degrees α, the furled HECS wing shape are an improvement over the elliptical wing, the results presented imply that the planar HECS wing seems the more viable candidate for rigid wing construction. Given the drag force reduction only at high α coupled with an 8-10% lift force reduction for all α while furled, this morphed configuration seems less attractive as a rigid wing shape than the planar HECS wing. The regions with enhanced drag reductions through furling may not be as critical as the preserved lift at cruise configurations of 0 to 5 degrees α, although Lazos finds higher lift coefficients in this range with the furled HECS wing in a more ideal experimental environment.

There are, however, multiple factors under consideration beyond vehicle lift and drag, motivating dynamics and controls studies of morphing wing vehicles at NASA

Langley (Bowman *et al.*, 2002; Davidson *et al.*, 2003) that led to selection of this wing for morphing actuation study in this research. The furled HECS wing preserves a lift-to-drag advantage over the elliptical wing below 1 degree and above 7 degrees α (and potentially more with cleaner data), and experiences the minimum drag force of all three wings tested for high α. Furthermore, when combined with the ability to use the furled HECS wing's vertical wingtips for lateral stability (Davidson *et al.*, 2003) or in place of conventional ailerons for asymmetric activation of roll effectors, the furled wing shape demonstrates a second flight regime with increased maneuverability and reduced drag at high angles of attack, and with reduced roll damping at the expense of decreased lift. Roll rate can be increased over that of the planar HECS wing because of the decreased wing-root bending moment, as discussed by Wiggins *et al.* (2004) and observed in the morphing experiments of Section 5. As morphing of the HECS wing can replace conventional ailerons, interference drag and noise may be reduced due to a more continuous curvature. Therefore, morphing the HECS wing complements a high efficiency cruise configuration in the planar state with a maneuverability configuration for high angles of attack in the furled state, as well as creating new control surfaces with enhanced lateral stability and roll rate characteristics. The morphological changes are similar to the aerodynamic changes seen in birds when transitioning from an extended wing, slow-speed flier to a folded wing configuration with enhanced dive and maneuverability characteristics, either to avoid predation with the latter or to take off, loiter, and land with the former wing shape (Tennekes, 2000).

In total, though the planar HECS wing is the best standalone wing of the three studied, it is the characteristics afforded by morphing, as well as the challenge of prescribing the hyperelliptical curvature, which led to selection of this wing for morphing

mechanism study. It is not within the scope of this research to address increased complexity and weight penalties associated with a rigid furled HECS wing or a full morphing wing structure compared to the simple construction of a square or tapered wing, nor are the objective functions of multi-functional aircraft considered when selecting the furled HECS wing as a target for morphing wing design.

4. Morphing Mechanism Design

As mentioned above, due to its complex curvature and unique aerodynamic characteristics in different configurations, the HECS wing has been studied by multiple investigators to better explore concepts for morphing airframe designs. The work of Wiggins *et al.* (2004) accomplishes shape change with a chain of four-bar linkages that approximate the curvature as a function of a single degree of freedom, and presents the mechanism concept and structural studies given predicted aerodynamic loading. The work of Moored and Bart-Smith (2007) focuses on the use of tensegrity structures and develops shape change by varying individual tendon lengths. It presents a study in determining the form of the tensegrity structure, and uses the HECS shape more as one potential realization of such a form than as the ultimate goal of the research.

In order to achieve the required shape change in the present research, the morphing mechanism at Cornell presents a new concept for a design with a discretized approximation to the spanwise HECS curvature, as shown in Figures 1.11 and 1.12. While initial attempts to use a varying radius spool concept are able to reduce shape change to a single degree of freedom (Manzo *et al.*, 2004), this scheme is replaced with individual shape memory alloy-actuated segments to be actuated in tandem from

a central microcontroller in order to reduce system complexity. This mechanism, using 0.015" diameter Flexinol® shape memory alloy wires from Dynalloy, achieves motion by rotating progressively more distal wing sections about hinge joints located in the terminal rib of the more proximal sections, as shown in the mechanism photograph of Figure 1.12. The distal section contains a large diameter spool used to increase the moment arm developed by the SMA wire, constrained by the maximum chord thickness of each section to keep the profile consistent. With the mechanism in place, the entire gapped section was covered with a latex fairing stretched between the two segments to reduce drag sources. Mechanism weight accounts for only 10% of the total wing weight including batteries, as compared to 15-20% for a DC motor-driven system. Additional study is required to assess the extent to which discrete approximation compromises performance, though skin systems help reduce wing discontinuity effects and future iterations can discretize the wing more finely.

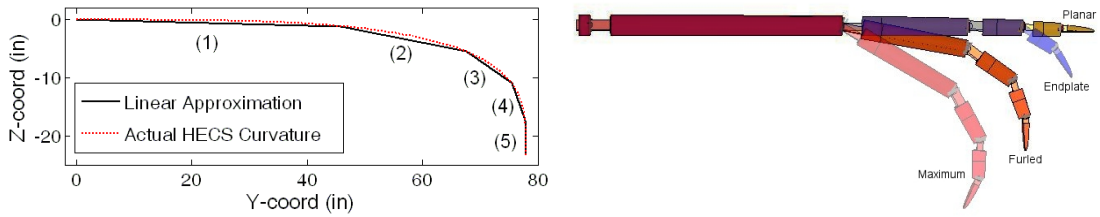

Figure 1.11 - Discretized approximation of curvature (left) and schematic of achievable workspace using SMA implementation (right)

The SMA is arranged in bays within each segment as shown in Figure 1.12, sized to overcome aerodynamic forces based on aerodynamic analysis of Section 3. Each joint contains the minimal required SMA length necessary for operation, reducing power requirements. Each bay is housed within a composite foam and fiberglass cavity, such that SMA wire length required for proper rotation of each joint is not exceeded. This

assumes 5% contraction for high SMA cycle life used for applying moments on each joint, with no two-way training.

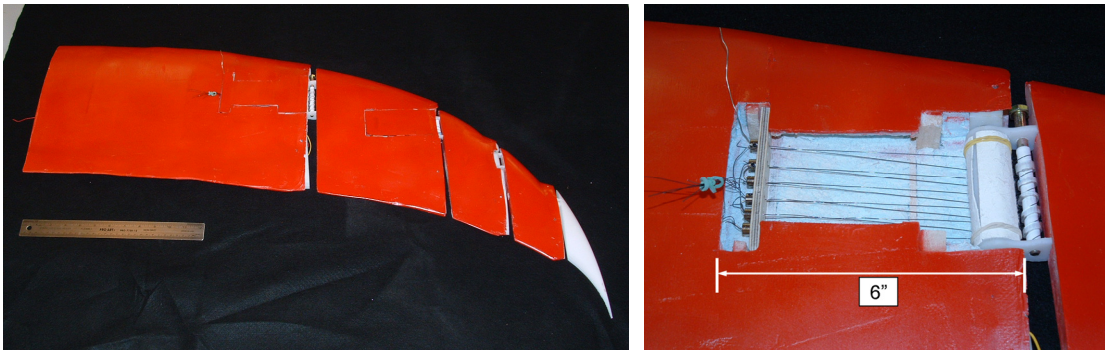

Figure 1.12 - HECS wing prototype before applying latex fairings over gaps (left), and close up view of SMA wire bay showing actuator configuration and moment arm (right)

The wire bays are powered via pulse-width-modulated (PWM) signals using proportional-integral control. This controller minimizes steady state error and response time, with potential overshoot during settling. Position sensing is achieved with a rotational potentiometer coaxially located at the joint hinges. The relative angle change at each joint determines the duty cycle yielding desired angular setpoints for each section. This electrical means of generating prescribed shape change allows for greater flexibility than mechanically constraining sections to move in tandem, as in the four-bar linkage approach of Wiggins or the tensegrity approach of Moored and Bart-Smith. Also, angular setpoint control allows testing of alternate configurations or for fine adjustments to deflection while under loading. Voltage input supplied by the PWM controller and flight-capable 12 volt supply convert thermal input to actuator strain, following Manzo (2006). While this can be achieved open loop, faster response is achieved with feedback, allowing higher voltages to quickly raise the temperature and consequent SMA strain. Figure 1.13 highlights control advantages for one

segment of the morphing wing; open loop control requires 10 times longer reach the desired angle versus closed loop control.

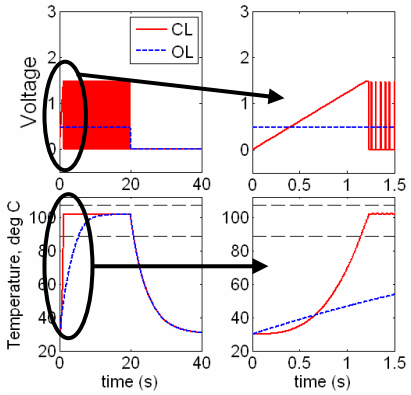

Figure 1.13 – Open and closed loop time history simulation of SMA voltage and temperature for segment of morphing HECS wing

A nonlinearity in on-off control exists due to cooling periods, leading to passive response when the SMA is strained by air loads into elongated detwinned martensite as in the temperature data at the 20 second mark of Figure 1.13. Because of this uncontrollable region, it is important to maintain precise position control by operating at high frequency. Therefore, the controller updates at 200 Hz to avoid large temperature changes, and controller gains are tuned to achieve complete shape change of each joint within 1-3 seconds.

Since each segment is controlled independently by changing angle setpoints θ_i, a family of wing shapes can be achieved in addition to the HECS wing configuration. Reachable shapes within maximum SMA contraction are shown in Figure 1.11, indicating potential endplate-like shape, approximate furled shape once discretized, and bounding deflection for a full 5% contraction of all SMA wire segments.

5. Morphing Results

The morphing wing is a 240% scale, 36.2" semispan starboard wing of planform area 350 in^2 (half-wing area). Root wing chord is 11.4", and Reynolds numbers range from 175,000 to 440,000 at the proximal 80% of the wing for airspeeds of 30 mph to 50 mph. A splitter plate forms a symmetry plane, collinear with the tunnel wall despite boundary layer interference at the test section (8" thickness) due to the scale required for mechanism precision. Tunnel blockage is a maximum of 4.9%, comparable to rigid wing tests due the smaller range of α tested before load cell saturation. The wing only actuates downwards; aerodynamic forces raise the wing to the planar shape and the unloaded wing rests in the tunnel as in Figure 1.14(a). This passive behavior, along with increased wing weight, requires that windspeed be higher than for the smaller rigid wings.

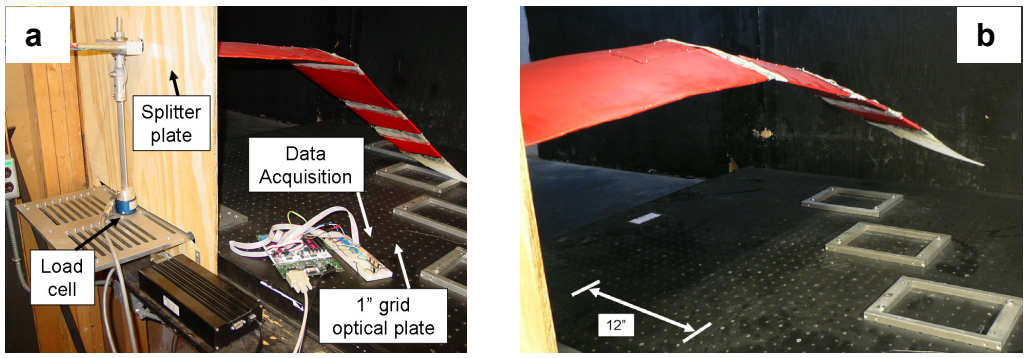

Figure 1.14 - Morphing HECS wing installation in Environmental Wind Tunnel facility, wing inactive (a) and active under aerodynamic loading in 'furled' configuration (b)

The wind tunnel wing specimen is smoothed and finished with a filling compound and sealed with latex paint to ensure minimal roughness, and latex fairings preloaded to over 100% tensile strain ensure tautness at hinge points shown in Figure 1.14(b). An ABS plastic wingtip ensures that proper tip shape is achieved. The finished half-wing

with actuators weighs 2.14 pounds without fairings (30% coming from finishing compound and paint layers), brought to a total weight of 2.45 pounds with added fairings. The wing was designed for tunnel tests, and is not refined to the point of a flightworthy system. By contrast, a full rigid planar HECS wing built with traditional wooden rib-and-spar construction weighs 1.47 lb with control surfaces and related hardware (Manzo *et al.*, 2005), weighing 70% less than the current morphing wing.

Unlike rigid wing testing, the morphing wing experiences significant wall and ground effects due to tunnel size limitations. In order to fabricate mechanisms with embedded sensor equipment at a workable scale, the wing was built with a half-span accounting for 75% of the tunnel width. In addition, the actuated wing places the tips within a height-to-span ratio of only 20% and the entirety of the wing within a semispan of the ground plane, placing it well within ground effect. This decreases downwash and significantly reduces induced drag, as well as artificially enhances wing lift. Therefore, aerodynamic loads are not a valid comparison with rigid wing tests, and are used predominantly to test mechanism performance. Morphing wing data is presented without correction for upwash, ground effect, or wall effects, as corrections would be inherently flawed.

System response is shown for a representative wing section in Figure 1.15(a). This plot shows raw angle data from the potentiometer, a filtered signal for clarity, and desired morphing period when reference angle, θ_{ref}, jumps from planar to furled setpoint. The SMA reaches desired angular position within 3 seconds, with slight overshoot due to sensor precision issues. The SMA model of Manzo (2006) is also overlaid assuming zero friction, highlighting the overshoot and actuator friction in the real system. This morph is achieved at 0 degrees α (uncorrected for upwash and ground effects) at 43 mph. For most angles of attack, wing lift follows a trend similar

to that of Figure 1.15(b), a different test run from Figure 1.15(a) with longer morphed shape duration. As morphing signal is sent, lift decreases due to span reduction associated with angle change, reaching a steady-state value of 3.4 lbf (15.1 N) compared to planar wing lift of 3.7 lbf (16.5 N) for the case shown. Wing lift center is also known based on torques on the load cell, shown in Figure 1.15(c). Lift center with respect to span moves inboard by approximately 1" (around 3% span), reflecting that during morphing the loss of horizontal wingtips will not significantly affect lift distribution, although it will scale the net lift down by almost 10%. Morphing can, however, be beneficial in rolling maneuvers due to decreased wing root moment – lift forces are both lower and closer to the fuselage, aiding in rolling the craft in the direction of a furled wing as discussed in Section 3.

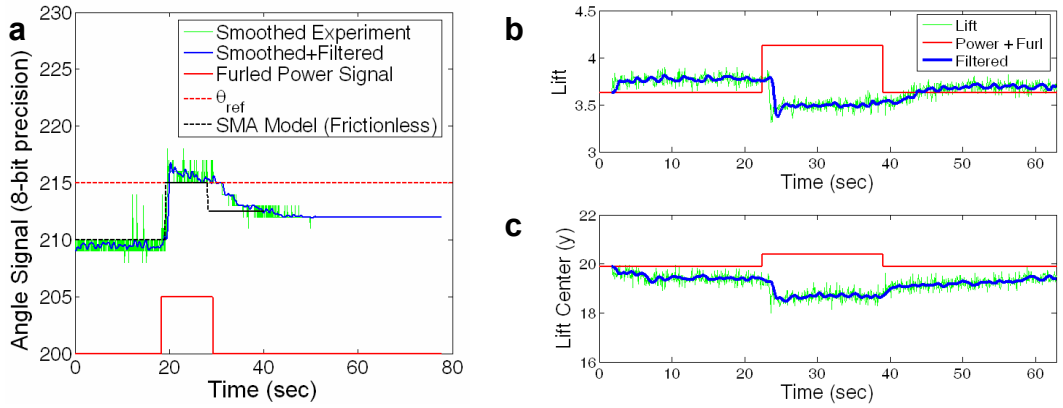

Figure 1.15 - Experimental time history deflection response of HECS wing section 2 at 43 mph, $\alpha=0^{o}$ (a), as well as wing lift (b) and change in wing lift center (c) over time for half-wing for a similar test with longer duration

Two points can be drawn from morphing experiments. First, the actuation system is capable of overcoming significant aerodynamic loads. Even in ground effect, when lift forces may be artificially augmented, SMA tendons are able to deform the structure. The discretized morphing wing demonstrates repeatable, precisely controlled shape change with the shape memory actuation system. Second, even in ground effect the furled HECS wing does not demonstrate overall lift improvements

compared to the planar HECS wing, due potentially to aspect ratio decrease. This may strengthen the findings of Section 3 in concluding that the furled wing offers little or no improvement over the planar HECS wing. While further testing is required under better flow conditions to definitively claim this result, morphing tests provide additional evidence that the planar HECS wing may be the better aerodynamic performer of the two states.

6. Conclusions

Designed for induced drag reduction, crescent-shaped planar HECS wings display net drag reductions over similar elliptical wings at angles above 5 degrees, with over 50% drag reduction at higher angles of attack. The flat HECS wing exceeds peak lift for a similar elliptical wing by 19% and overall lift by as much as 100% in trimmed flight. Due to aspect ratio decrease, the furled HECS wing decreases these merits, questioning the merits of morphing compared to the rigid, planar HECS wing. Testing without ground effect is required to assess advantages of increasing spanwise efficiency in tandem with span decrease, though lift and drag enhancements through morphing would be small at best. For use on this or other adaptive wings, a shape memory alloy actuated morphing mechanism is presented using angular position feedback and pulse width modulated control to overcome lift forces on a UAV-scale morphing wing. In initial testing with moderate friction, the mechanism provides sufficient torque to yield shape change in a lightweight, low complexity package. With user reconfigurable setpoints and integral feedback control, wing shape can be set to any location within the SMA actuation envelope, with accurate reorientation within 1-3 seconds useful for slow-speed gross shape change. Improvements using antagonistic actuators can expedite cooling response and may increase bandwidth to that sufficient for use as a control effector.

REFERENCES

Abdulrahim, M. and Lind, R., 2004, "Flight Testing and Response Characteristics of a Variable Gull-Wing Morphing Aircraft," AIAA 2004-5113, AIAA Guidance, Navigation, and Control Conference and Exhibit, August 16-19, Providence, RI.

Blondeau, J. and Pines, D., 2003, "Wind Tunnel Testing of a Morphing Aspect Ratio Wing Using an Pneumatic Telescopic Spar," AIAA 2003-6659, 2nd AIAA 'Unmanned Unlimited' Systems, Technologies, and Operations – Aerospace, Land, and Sea Conference and Workshop & Exhibit, Sept. 15-18, San Diego, CA.

Bowman, J., Sanders, B., and Weisshaar, T., 2002, "Evaluating the Impact of Morphing Technologies on Aircraft Performance", AIAA 2002-1631.

Burkett, C., 1989, "Reductions in Induced Drag by the Use of Aft Swept Wing Tips," *Aeronautical J* Dec.: 400-405.

Cone, C., 1963, "The Theory of Induced Lift and Minimum Induced Drag of Nonplanar Lifting Systems," NASA TR R-139.

Davidson, J., Chwalowski, P., Lazos, B., 2003, "Flight Dynamic Simulation Assessment of a Morphable Hyper-Elliptic Cambered Span Winged Configuration", AIAA 2003-5301, AIAA Atmospheric Flight Mechanics Conference and Exhibit, Austin, Texas, August 11-14.

DeLaurier, J., 1999, "The Development and Testing of a Full-Scale Piloted Ornithopter." *Canadian Aeronautics and Space Journal* (45): 72-82.

Dietl, J. and Garcia, E., 2008, "Stability in Ornithopter Longitudinal Flight Dynamics", *J. Guid., Control, and Dyn.* (31): 1157-1162.

Faye, R., Laprete, R., and Winter, M., 2002, "Blended Winglets for Improved Airplane Performance", *Aero Magazine* (17): 16-31.

Henderson, W. and Holmes, B., 1989, “Induced Drag – Historical Perspective,” SAE Paper 892341.

Katz, J, and Plotkin, A., 2001, "Finite Wing: The Lifting Line Model," *Low-Speed Aerodynamics,* 2nd ed, Cambridge University Press: 173–178.

Lazos, B., 2005, “Biologically Inspired Fixed-Wing Configuration Studies,” *J. Aircraft* 42: 1089-1098.

Lazos, B. and Visser, K., 2006, “Aerodynamic Comparison of Hyper-Elliptic Cambered Span (HECS) Wings with Conventional Configurations,” *AIAA*: 2006-3469.

Liersch, C., Streit, T., and Visser, K., 2009, “Numerical Implications of Spanwise Camber on Minimum Induced Drag Configurations”, AIAA 2009-898, 47th AIAA Aerospace Sciences Meeting, January 5-8, Orlando, FL.

Liu, T., Kuykendoll, K., Rhew, R., and Jones, S., 2004, “Avian Wings,” AIAA 2004-2186, 24th AIAA Aerodynamic Measurement Technology and Ground Testing Conference, June 28 - July 1, Portland, OR.

Lnenicka, J., 1974, "Report to Pierpont of NASA Langley on the Critical Reynolds Number of the NASA 4412 Airfoil." Czechoslovakia.

Love, M., Zink, P., Stroud, R., Bye, D., and Chase, C., 2004, “Impact of Actuation Concepts on Morphing Aircraft Structures,” AIAA 2004-1724, 45th AIAA Structures, Structural Dynamics & Materials Conference, April 19-22, Palm Springs, CA.

Majii, M., Rediniotis, O., and Junkins, J., 2007, “Design of a Morphing Wing: Modeling and Experiments,” AIAA 2007-6310, AIAA Atmospheric Flight Mechanics Conference and Exhibit, Aug. 20-23, Hilton Head, SC.

March, A., Bradley, C., and Garcia, E., 2005, "Aerodynamic Properties of Avian Wings as a Function of Wing Shape," IMECE 2005-83011, Orlando, FL.

Manzo, J., Garcia, E., Wickenheiser, A., and Horner, G. 2004, "Adaptive structural systems and compliant skin technology of morphing aircraft structures", Smart Structures and

Materials 2004: Smart Structures and Integrated Systems, March 14-17, San Diego, CA. published in: *Proc. SPIE* Vol. 5390, pp. 225-234.

Manzo, J., Garcia, E., Wickenheiser, A., and Horner, G., 2005, "Design of a shape-memory alloy actuated macro-scale morphing aircraft mechanism", Smart Structures and Materials 2005: Smart Structures and Integrated Systems, March 6-10, San Diego, CA. published in: *Proc. SPIE* 5764, pp. 232-240.

Manzo, J. 2006. "Analysis and design of a hyper-elliptical cambered span morphing aircraft wing." Masters Thesis. Cornell University, Ithaca, NY.

Moored, K. and Bart-Smith, H., 2007, "The Analysis of Tensegrity Structures for the Design of a Morphing Wing," *Trans. ASME* 74: 668-676.

Munk, M., 1923, "The Minimum Induced Drag of Airfoils," NACA Report 121.

Rae, W. and Pope, A., 1984, *Low-Speed Wind Tunnel Testing*. New York, NY: John Wiley & Sons. Pg. 200-203, 362-432.

Rokhsaz, K., 1993, "A Brief Survey of Wingtip Devices for Drag Reduction," SAE Paper 932574.

Selig, M., Donovan, J., and Fraser, D., 1989, *Airfoils at Low Speeds (Soartech 8)*. Virginia Beach, VA: H.A. Stokely. Pg. 81-82, 122, 320-329.

Simons, M., 1999, *Model Aircraft Aerodynamics, 4th Ed*. Poole, Dorset: Special Interest Model Books. Pg. 245, 258.

Siochi, E., Anders, J., Cox, D., Jegley, D., Fox, R., and Katzberg, S., 2002, "Biomimetics for NASA Langley Research Center," NASA TM-2002-211445.

Spillman, J.J., 1987, "Wing Tip Sails, Progress to Date and Future Developments," *Aeronautical Journal* Dec. 91: 445-453.

Tennekes, H., 2000, *The Simple Science of Flight: From Insects to Jumbo Jets*. Cambridge, MA: MIT Press.

Tucker, V., 1987, "Gliding Birds: The Effect of Variable Wing Span," *J. Exp. Biol.* 133: 33-58.

Tucker, V., 1993, "Gliding Birds: Reduction of Induced Drag by Wing Tip Slots Between the Primary Feathers," *J. Exp. Biol.* 180: 285-310.

van Dam, C.P., 1987, "Induced-Drag Characteristics of Crescent-Moon-Shaped Wings," *J. Aircraft* 24: 115-119.

Whitcomb, R., 1976, "A Design Approach and Selected Wind-Tunnel Results at High Subsonic Speeds for Wing-Tip Mounted Winglets," NASA TN D-8260, July.

Wickenheiser, A. and Garcia, E., 2007, "Aerodynamic Modeling of Morphing Wings Using an Extended Lifting-Line Analysis," *J. Aircraft* 44: pp 10-16.

Wiggins, L., Stubbs, M., Johnston, C., Robertshaw, H., Reinholtz, C. and Inman, D., 2004, "A Design and Analysis of a Morphing Hyper-Elliptic Cambered Span (HECS) Wing," AIAA 2004-1885, 45th AIAA Structures, Structural Dynamics and Materials Conference, April 19-22, Palm Springs, CA.

Wlezien, R., Horner, G., McGowan, A., Padula, S., Scott, M., Silcox, R., and Simpson, J., 1998, "The Aircraft Morphing Program," AIAA 1998-1927, 39th AIAA Structures, Structural Dynamics, and Materials Conference and Exhibit, April 20-23, Long Beach, CA.

This chapter originally appeared as:

Manzo, J., and Garcia, E., "Demonstration of an *in situ* morphing hyperelliptical cambered span wing mechanism," *Smart Materials and Structures*, Vol. 19, No. 2, 2010.

CHAPTER 2

BAT-INSPIRED WING AERODYNAMICS AND OPTIMIZATION[1]

1. Introduction

As engineers search to make micro air vehicles more stable, maneuverable, and efficient, many are turning towards biology for inspiration. Bats adapt to their environment by morphing their wings in flight. Depending on their niche, certain species soar and glide [1] while others perform barrel rolls in nature [2] and can pull up to 4.5 g's in obstacle courses [3]. Morphological changes afford bats great agility at low speeds, and they are able to maintain stability and control at low Reynolds numbers, where viscous effects and leading edge laminar separation bubbles cause nonlinearities in lift [4-6]. Bats achieve these feats with finger-like jointed bone structures and flexible wing membranes. These unique traits allow them to change camber and twist in flight, unlike avian span changes.

Recent studies investigate replicating flapping bat flight [7-9], while others focus specifically on flexible, membrane wing benefits at low Reynolds numbers for improvements in gust alleviation and delayed stall characteristics [10-12]. These wings are passive elements, and it is difficult to attach control surfaces to them for flight authority. By actively controlling and morphing flexible wings, conventional controllers can be replaced. Aircraft morphing allows single vehicles to have multiple functions, ideally with continuous lifting surfaces to alleviate drag and vibration and increase efficiency. This is the focus of Garcia *et al*. [13], which proposes a non-

[1] From Leylek, E., Manzo, J. and Garcia, E., "Bat-inspired wing aerodynamics and optimization"; reprinted by permission of the American Institue of Aeronautics and Astronautics, Inc.

flapping wing with twist capabilities. Morphing enables tailoring of wing shapes to multiple flight regimes, from take-off through cruise to landing [14-16]. Many mechanisms have been proposed for morphing such as the *smart joint*, an active rigidity composite suited to actuating a bat-like membrane wing in flight [17]. This low-profile device can be embedded at joints in the finger-like skeletal wing structure as a bimorph actuator [18]. While this work focuses on static wing configurations rather than morphing behavior, results help specify actuator requirements used for a variable camber and twist wing.

In this work, two key features of bat flight are studied – uniquely evolved bat wing planforms adapted to environments, and capabilities afforded through variable camber and twist – and are applied to rigid, fixed wing designs for small man-made craft. The goal of this study is not to mimic natural bat flight, but to understand how certain aspects of bat flight apply to the engineering problem of wing design for micro air vehicles.

2. Background and Motivation

To perform maneuvers unprecedented in animal flight, bats primarily control wing shape by using the 5^{th} digit of their hand-like bone structure to vary camber, analogous to conventional aircraft flaps [1-3,19-22]. They also create leading edge slats using their thumb and propatagium, the wing membrane in front of the arm. This device also changes wing camber, helps keep the boundary layer attached, and prevents flow separation, particularly at high angle of attack, α [3,21,22]. To initiate turns, bats morph their wings to create asymmetric lift, increasing α on one wing and decreasing it on the other by modifying twist distribution. Asymmetric lift distribution is also

achieved by increasing or negating camber, or by stalling all or part of one wing. These twist and camber morphology changes and their aerodynamic effects on bat wing planforms are the focus of this research.

2.1. Morphological Correlations to Flight Performance

Maneuverability is defined as the space required for turns at fixed speed, and agility is maximum roll acceleration available to initiate a turn [2]. Wings favoring maneuverability have large area, low aspect ratio, and rounded wingtips. Similar to human aircraft, agile wings produce large rolling torque by creating asymmetric lift as described above. This is accomplished either by reducing wing inertia or by creating large rolling moments [2]. Bat flight performance can also be measured by cost of transport, a measure of efficiency. Highly efficient bat wings require minimal thrust and produce minimal drag, factors particularly important for migratory or commuting bats. Their wings usually have a high aspect ratio and pointed wingtips [2]. Generally, bat wings are not this simply defined, and represent additional morphological adaptations to succeed in their niche.

2.2. Bat Species Studied

In this research three diverse species are selected, embodying different wing forms and flight functions. Performance of these species is compared, including evaluation of wing morphing utility. Wing planforms are shown in Figure 2.1, extracted from Norberg *et al.* [1,2].

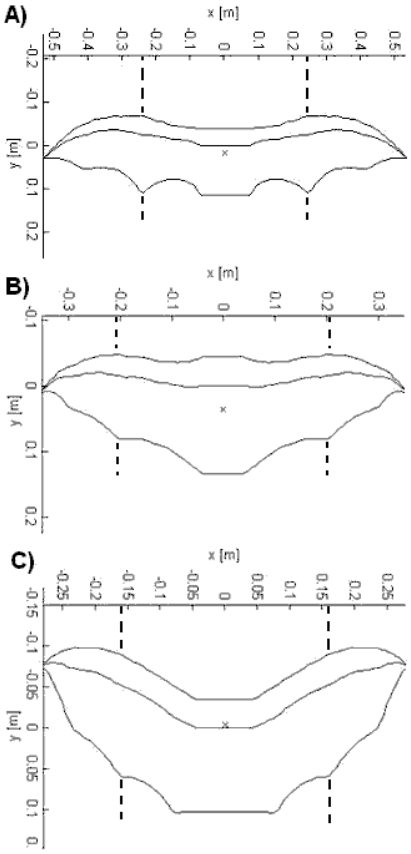

Figure 2.1 - Bat wing planforms studied, fifth finger location at dashed lines. A) *Noctilio leporinus*, B) *Pteropus livingstonii*, C) *Nycteris hispida*

The first bat of Figure 2.1 is the piscivorous (fish-hunting) *Noctilio leporinus*. Its high aspect ratio wing allows efficient flight during commutes to water sources but also has large, rounded wingtips providing stability and control for prey capture [2]. *Pteropus livingstonii* is a soaring fruit bat, with mid-range aspect ratio and pointed wingtips for increased efficiency [1]. *Nycteris hispida* hunts for insects in heavy vegetation, with short wings of low aspect ratio. Its flight is slow but maneuverable and agile, with large, rounded wingtips [2]. The shape of the wings suggests that *Noctilio leporinus* combines characteristics for low cost of transport with maneuverability, *Pteropus. livingstonii* is evolved for efficient flight, and *Nycteris hispida* has wings designed for high maneuverability and agility.

3. Computational Analysis

Wing topology, in the form of quarter chord location and chord length distribution, was measured from reference drawings [1,2] using CorelDraw 8.0 and entered into MATLAB to create digital planforms (Figure 2.1). Diverging from natural flapping flight to fixed wing designs, topology is mapped onto a solid airfoil distribution. An in-house lifting line analysis is used to evaluate the flight characteristics of entire wings [23].

3.1. Methodology

Data based on XFOIL studies best determines airfoil distribution using thin, cambered NACA airfoils. XFOIL is a computational solver for 2-D airfoils combining an inviscid panel method with a boundary layer formulation to predict lift, drag, and pitching moment for airfoils in viscous flows [24]. Airfoils of the 4-digit NACA family, all with 3% thickness-to-chord ratio and maximum camber located at 30% chord (NACA *x*303), are investigated to study how camber affects lift coefficient and lift-to-drag ratio for low Reynolds numbers. The turbulence transition is free, and wings are studied at a Reynolds number of 100,000 - the upper end of bat and MAV flight regimes (10^4-10^5) [11,20]. Results of this study are presented in Reference 25. In addition to thickness limitations prohibiting quasi-membrane study, XFOIL is known to over-predict lift and under-predict drag, a common result yielding artificially enhanced theoretical results [4].

A lifting-line analysis, based on Weissinger's method for straight, swept wings, decomposes 3-D wings into a series of 2-D airfoils. Each bat wing consists of 101 spanwise stations, with lifting line assumed at the quarter chord point. Potential flow theory calculates wing circulation and consequent lift by relating downwash at each station to horseshoe vortex intensity acting at the quarter chord and projected to a semi-infinite trailing vortex sheet [23]. This method allows for curved wing planforms, taking into account variable profile wing shapes by incorporating look-up tables for 2-D airfoil data from XFOIL. The code yields lift and drag forces, as well as pitch, roll, and yaw moments. Lifting-line analysis assumes a planar trailing vortex sheet and, being a potential flow method, is valid at high Reynolds numbers with minimal viscous effects and no separation [23]. However, using airfoil data incorporating XFOIL's boundary layer formulation accounts for some viscous effects apparent in low Reynolds number flight. While numerical solutions may not be exact, the code has utility for initial design and comparison of wing shapes given its speed and simplicity.

Each wing is scaled by mean chord to a Reynolds number of 100,000 flying at 10 m/s, matching bat flight speeds. Two topologies are tested for each species' planform - an "unmorphed" and a "morphed" snapshot. The unmorphed shape is a flat wing consisting of symmetric NACA 0003 airfoils without twist to be a baseline for comparison. The morphed configuration models bat wing shapes in gliding flight, graphically interpolated from flight images as an 'initial guess' for morphed wing shape used in analysis. Camber and twist distributions provide sufficient information to prescribe 3-D wing shapes from digitized planforms.

For the morphed wing shape, the midsection representing bat body is assumed to produce zero lift in level flight, such that root is an untwisted NACA 0003 airfoil. A NACA 7303 airfoil is placed at the fifth digit, representing camber actuation marked by dashed locations in Figure 2.1. This airfoil is selected through XFOIL study as having the highest lift-to-drag ratio, a requirement for gliding. Wingtip profile assumes airfoils of 1% camber, or NACA 1303. Airfoil distribution is indicated by points A, B, and C in Figure 2.2 for each wing, with linear interpolation between points. Regions of positive and negative twist are shown qualitatively in Figure 2.2, magnified for clarity. Observed in bat flight images, at the fifth digit the wing trailing edge deflects below the X-Y plane and the leading edge deflects upwards, while at the tips wings have a slightly negative α, suspected to reduce induced drag. Overall twist has a linear distribution from 0° at the center to +5° at the fifth digit to -2° at the tip.

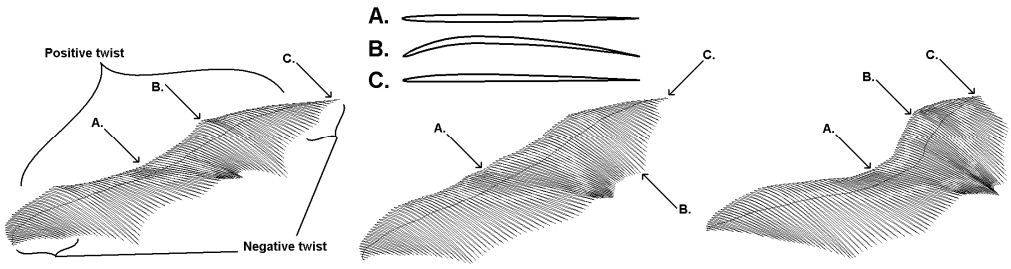

Figure 2.2 - Bat wings (not to scale) from 2-D airfoils, twist magnified 5x. Left to right: *N. leporinus, P. livingstonii, N. hispida*

3.2. Computational Results

Working with pre-stalled performance based on airfoil studies, Weissinger analysis sweeps from -2° to 12° by increments of 0.2°. Lift coefficient versus α for the flat unmorphed and cambered and twisted morphed wings is shown in Figure 2.3, and lift-to-drag ratio versus α for both configurations is compared in Figure 2.4. The morphed

shape is strongly favored in these plots. Both lift and lift-to-drag are higher in the morphed configurations for each species across all α. Maximum lift coefficient increases over 50% for each species when morphed. Due to increased camber through morphing, drag coefficient (not pictured) also increases; however, lift-to-drag ratio still increases around 34% in the morphed shape for each species. Further details of this study are given in Ref. 25.

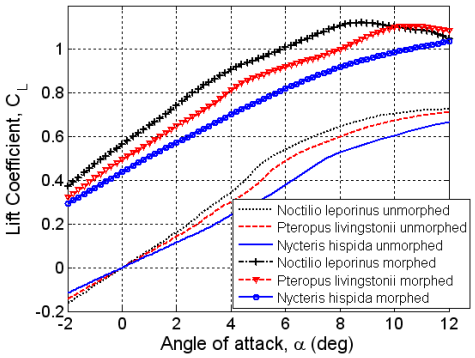

Figure 2.3 - Lift coefficient vs. α for morphed and unmorphed wings

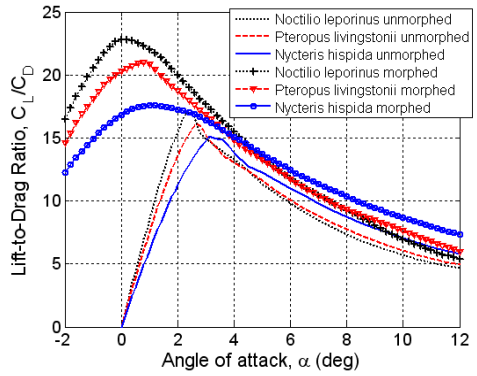

Figure 2.4 – Lift-to-drag ratio vs. α for morphed and unmorphed wings

Results predicted through Weissinger analysis for morphed configurations correspond well to expected natural flight for the three bat species. *Noctilio leporinus* has the highest lift coefficient, fitting given its need to carry prey. It also has high lift-to-drag ratio, which would be consistent with its nature as it must have efficient flight to

commute to water sources. *Pteropus livingstonii* also has high lift-to-drag ratio, expected since efficiency is necessary for soaring but aspect ratio is lower than that of *N. leporinus*. Insectivorous *Nycteris hispida* must be agile and maneuverable, and it has evolved its wing shape as such. Its wings have forward sweep, causing the inboard wing portion to stall first. This sweep allows it to maintain roll control and resist spins by using outboard fingers to control camber [26]. As noted by Raymer [27], combination of these effects delays overall wing stall, as does its low aspect ratio. It has the lowest peak lift-to-drag ratio of the three species, though at high α lift-to-drag is highest. This high α advantage allows for higher bank angles and more extreme turn capabilities than other bats. Lift distributions in Figure 2.5 also give insight to *N. hispida*'s maneuverability - peaks center in the middle of each wing for the more efficient *N. leporinus* and *P. livingstonii*, whereas with *N. hispida* lift concentrates towards the tips.

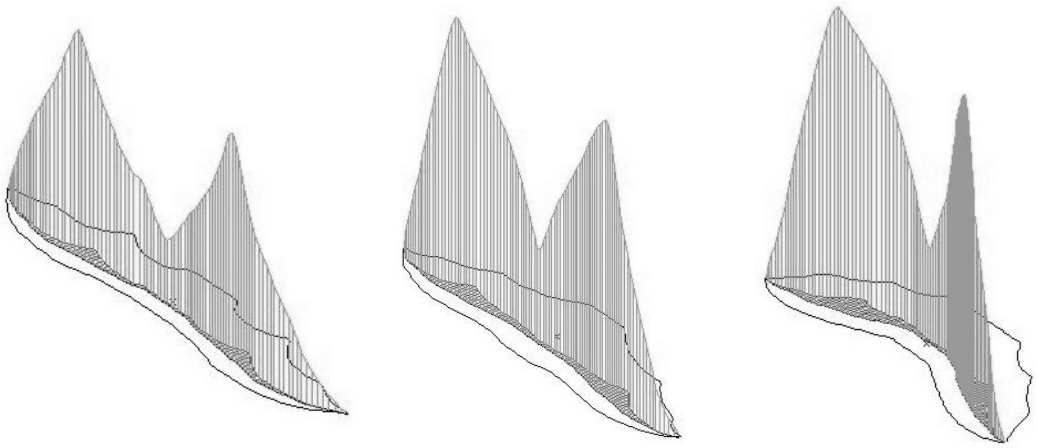

Figure 2.5 - Lift distributions across the wings of *N. leporinus*, *P. livingstonii*, and *N. hispida* (left to right)

4. Experimental Validation

4.1. Experimental Methods

To assess Weissinger method accuracy, wind tunnel models of morphed and unmorphed *Pteropus livingstonii* wings were fabricated using a Stratasys Dimension rapid prototyper of ABS plastic, with steel dowels for added rigidity. Wings connect to an aerodynamic sting atop a six degree-of-freedom JR3 load cell, which measures lift to 25 pounds with a resolution of less than 0.01 pound. Tests use the Cornell University Environmental Wind Tunnel Facility, an open return wind tunnel with a 48" x 43" test section. Test speeds are approximately 10.8 m/s (24 mph), with α ranging from -2° to 14° by increments of about 1°. Lift, drag, and pitch data is sampled at 250 Hz for 90 seconds at each α and a Butterworth filter with cut-off frequency at 20 Hz filters tunnel noise.

4.2. Experimental Results

Figures 2.6 – 2.8 show experimental data compared to computational results. The 1-σ bounds from filtered data are also shown. Since the Weissinger method has limitations discussed in Section 3, it was expected that analysis would not capture exact values but rather trends, as is apparent in results. In Figure 2.7, computed drag is within experimental error for the unmorphed wing, proving the Weissinger method numerically accurate for this simple case. Experiments confirm that lift and drag coefficients are higher for the morphed wing than unmorphed. Lift coefficient increases more than drag coefficient, such that lift-to-drag ratio is higher with morphed shape. The maximum lift-to-drag ratio occurs at the same α in

computational and experimental results, indicating a correlation with the Weissinger method.

Experimental results show a 34% increase in maximum lift coefficient and a 72% increase in maximum lift-to-drag ratio, compared to 51% and 30%, respectively, through Weissinger analysis. Although experimental maxima are less than anticipated results from analysis, significant improvements exist in the morphed topology compared to unmorphed.

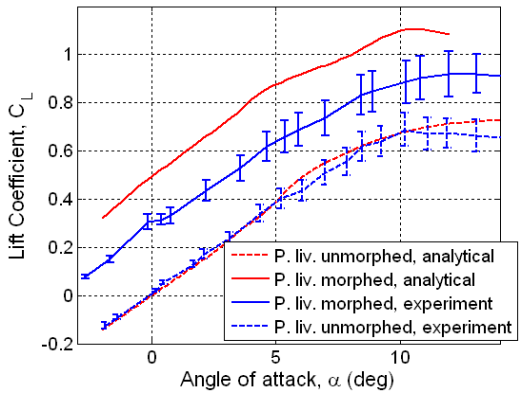

Figure 2.6 - Lift coefficient vs. α for morphed and unmorphed configurations of *P. livingstonii*

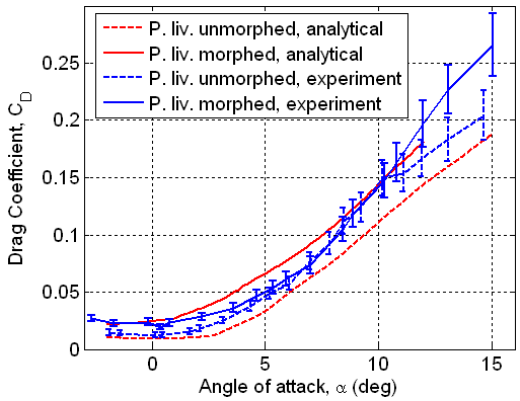

Figure 2.7 - Drag coefficient vs. α for morphed and unmorphed configurations of *P. livingstonii*

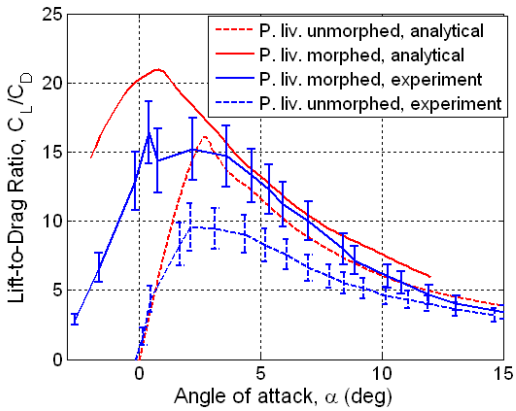

Figure 2.8 - Lift-to-drag ratio vs. α for morphed and unmorphed configurations of *P. livingstonii*

4.3. Accuracy of Results

Errors in experimental results come in part from the wind tunnel, which can have an unsteady and changing flow. There is also some degree of turbulence in the wind tunnel, and the wing surface may not be perfectly smooth. The thin, plastic model is subject to vibrations, some of which are removed through filtering. The method of measuring α is imperfect, causing the entire lift curve to be shifted up to 1° along the α–axis. Though area blockage and side wall effects are minimal, the wing height-to-span ratio is only 0.5, placing it in ground effect and increasing lift coefficients above their true values.

5. Optimization

5.1. Optimization Method

Heuristic optimization can determine wing morphing parameters yielding enhanced flight performance and expanded flight envelopes. Here we consider wings optimized

without fuselage contributions. Performance metrics are reduced to aerodynamic parameters, similar to optimization of 2-D airfoils [4,16,27]. These metrics and their correlations to flight performance are summarized in Table 2.1. The bat wing model is modified from the initial guess for morphed configuration of Section 3.1. The root is again modeled as a non-lifting element, so a symmetric NACA 0003 with zero twist is maintained in the midsection of the wing. Table 2.2 provides summary of design parameters and bounds. Camber and twist angles are linearly interpolated between the root and fifth digit as well as between the fifth digit and wingtip.

Table 2.1 - Summary of optimized cost functions and correlations to flight performance

Performance Metric	**Correlated Performance Characteristics**
1. Maximum lift coefficient	Take-off Instantaneous Turns Turn radius
2. Minimum drag	Climb Acceleration Dash
3. Maximum lift-to-drag	Cruise Range Powered Loiter/Endurance Sustained Turns
4. Minimum power consumption ($C_L^{(3/2)}/C_D$)	Power Consumption Gliding Endurance Sinking Rate

Table 2.2 - Design parameters and their bounds

Parameter and Bounds	
1. Camber at wing root	$[0,9] \in \mathbf{Z}$
2. Camber at 5^{th} digit	$[0,9] \in \mathbf{Z}$
3. Twist at 5^{th} digit	$[0,6] \in \mathbf{Z}$
4. Twist at wingtip	$[-3,3] \in \mathbf{Z}$
5. Angle of attack, α	$[-2,14] \in \mathbf{Z}$

To reduce the number of calculations, simulated annealing is chosen as the optimization method, proven robust and reliable in finding global optima [28]. The MATLAB code written and used by Goffe *et al*. [29] is adapted to the outlined design variables and forms a shell around the extended Weissinger method. As the Weissinger method only allows integer values for camber, all state variables lie in discrete space. This reduces final state accuracy, but also decreases search space size and runtime.

5.2. Optimization Results

Each cost function was tested three times with different initial morphed wing shapes, ensuring that optimization yields consistent convergence to the global maximum. Results of tested cost functions and improvement over initial guess morphology for *P. livingstonii* are presented in Table 2.3, with other species omitted for brevity. Optimized state follows the order of Table 2.2.

Table 2.3 - Optimization Results for *Pteropus livingstonii*

Cost	**Optimum found**	**Improvement**	**State**
Maximum lift	1.43	29.4%	[8;9;5;3;14]
Min C_D	0.00920	58.1%	[0;0;0;1;0]
Max C_L/C_D	22.79	8.89%	[6;5;2;-2;2]
Max $C_L^{(3/2)}/C_D$	17.761	13.3%	[6;7;1;0;3]

To maximize lift, the wing morphology approaches the upper bound of all design parameters. Aerodynamic theory predicts that lift is increased as camber, twist, and/or α increases, continuing until flow separates on the upper side of the wing. In agreement with this, optimization yields camber and α at maximum lift before stall. Optimized wings for each species have not only higher peak lift than the initial guess

morphed configuration, but higher lift coefficients at every α considered. For both lift-to-drag ratio and $C_L^{3/2}/C_D$ metrics, wings have moderate camber values, coinciding with XFOIL results from Reference 25, wherein airfoils with 5-7% camber are the most efficient.

Wings optimized for minimum drag are different than those for other flight parameters, and more closely resemble the unmorphed shape. With minimum drag, all three species need very slight or no camber, a tip twist of 1 or 2°, and a small cruise α of 0 to 2°, all expected since these almost symmetric wings have minimal lift at this α and minimal lift-induced drag. The drag metric reveals the necessity for wings morphing between symmetric, untwisted shapes when minimum drag is critical, and with added camber and twist for enhancing other metrics. Further results are given in Reference 30.

In general, performance improves by the same amount for wing planforms representing each species. For example, in all three planforms, drag decreases by about 60% after morphed shape optimization. Trends between species generally remain the same: *N. leporinus* has highest lift-to-drag ratio and *N. hispida* has the lowest, except at higher α, as with the behavior of initial guess morphologies. This suggests that wing shape characteristics such as aspect ratio and tip shape have a dominant effect in determining and limiting flight performance of a particular bat species.

6. Conclusion

This research adapts bats' characteristic planforms and morphological change capabilities to man-made fixed wings with future morphing potential. Even using an initial guess for bat wing shape change, morphing from a flat to cambered and twisted state yields significant lift and efficiency improvements. Experimental snapshot data of morphed and unmorphed wing states validates qualitative trends seen through analysis, while morphed shape optimization further expands capabilities by prescribing shape change suited not just to ecological niche, but to maximizing key flight parameters. While the piscivorous *Noctilio leporinus* has the best lift-to-drag ratio and endurance characteristics, its maximum lift and minimum drag are very close to those achieved by the soaring *Pteropus livingstonii*. Agile *Nycteris hispida* has the best performance relative to the other two bat species at high angles of attack, useful for navigation in tight spaces. Results define morphologies that bat-like wings should adopt for different mission objectives and can inform actuator requirements in terms of deflection, sizing, and load carrying capability. Findings indicate that engineered wings inspired by bat planforms and morphologies can provide significant merits to the aerospace community, in terms of both aerodynamic efficiency and an increased and highly adaptable flight envelope.

REFERENCES

[1] Norberg, U.M., Brooke, A.P., and Trewhella, W.J. "Soaring and non-soaring bats of the family pteropodidae (flying foxes, pteropus spp.): wing morphology and flight performance," *Journal of Experimental Biology,* Vol. 203, 2000, pp. 651-664.

[2] Norberg, U.M. and Rayner, J.M.V. "Ecological Morphology and Flight in Bats (Mammalia; Chiroptera): Wing Adaptations, Flight Performance, Foraging Strategy and Echolocation," *Philosophical Transactions of the Royal Society of London. Series B, Biological Sciences*, Vol. 316, No. 1179, 1987, pp. 335-427.

[3] Bullen, R., and McKenzie, N.L. "Bat airframe design: flight performance, stability and control in relation to foraging ecology," *Australian Journal of Zoology*, Vol. 49, 2001, pp. 235-261.

[4] Shyy, W., Klevebring, F., Nilsson, M., Sloan, J., Carroll, B. and Fuentes, C. "Rigid and Flexible Low Reynolds Number Airfoils," *Journal of Aircraft*, Vol. 36, No. 3, 1999, pp. 523-529.

[5] Lee, C.S., Pang, W.W., Srigrarom, S., Wang, D., and Hsiao, F. "Classification of airfoils by abnormal behavior of lift curves at low Reynolds number," AIAA 2006-3179, *24th Applied Aerodynamics Conference*, 2006.

[6] Reid, M.R., and Kozak, J. "Thin/cambered/reflexed airfoil development for micro air vehicle applications at Reynolds numbers of 60,000 to 100,000," AIAA 2006-6832, *AIAA Atmospheric Flight Mechanics Conference and Exhibit*, 2006.

[7] Willis, D.J., Persson, P., Israeli, E.R., Peraire, J., Swartz, S.M., and Breuer, K.S., "Multifidelity Approaches for the Computational Analysis and Design of Effective Flapping Wing Vehicles," AIAA 2008-518, *46th AIAA Aerospace Science Meeting and Exhibit*, Reno, Nevada, Jan. 7-10, 2008.

[8] Swartz, S.M., Iriarte-Diaz, J., Riskin, D.K., Song, A., Tian, X., Willis, D.J., and Breuer, K.S. "Wing Structure and the Aerodynamic Basis of Flight in Bats," *45th AIAA Aerospace Sciences Meeting and Exhibit*, Reno, Nevada, Jan. 8-11, 2007.

[9] Bunget, G. ""BATMAV: A Biologically-Inspired Micro-Air Vehicle for Flapping Flight," Masters Thesis, North Carolina State University, Raleigh, NC, 2007.

[10] Song, A.J. and Breuer, K.S. "Dynamics of a Compliant Membrane as Related to Mammalian Flight," AIAA 2007-665, *45th Aerospace Sciences Meeting and Exhibit*, Reno, Nevada, Jan. 8-11, 2007.

[11] Ifju, P.G., Jenkins, D.A., Ettinger, S., Lian, Y., Shyy, W., and Waszak, M.R. "Flexible-Wing-Based Micro Air Vehicles," AIAA 2002-0705, *40th AIAA Aerospace Sciences Meeting and Exhibit*, Jan. 14-17, 2002.

[12] Lian, Y. and Shyy, W. "Numerical Simulations of Membrane Wing Aerodynamics for Micro Air Vehicle Applications," *Journal of Aircraft*, Vol. 42, No. 4, July-Aug. 2005, pp. 865-873.

[13] Garcia, H.M., Abdulrahim, M., and Lind, R. "Roll control for a micro air vehicle using active wing morphing," AIAA-2003-5347, *AIAA Guidance, Navigation, and Control Conference and Exhibit*, Austin, Texas, Aug. 11-14, 2003.

[14] Wlezien, R.W., Horner, G.C., McGowan, A.R., Padula, S.L., Scott, M.A., Silcox, R.J., and Simpson, J.O. "The aircraft morphing program," AIAA-98-1927, *39th AIAA/ASME/ASCE/AHS/ASC Structures, Structural Dynamics, and Materials Conference and Exhibit*, 1998.

[15] Bowman, J., Sanders, B., and Weisshaar, T. "Evaluating the impact of morphing technologies on aircraft performance," AIAA-2002-1631, *43rd AIAA/ASME/ASCE/AHS/ASC Structures, Structural Dynamics, and Materials Conference*, 2002.

[16] Joshi, S.P., Tidwell. Z., Crossley, W.A., and Ramakrishnan, S. "Comparison of Morphing Wing Strategies Based Upon Aircraft Performance Impacts," AIAA 2004-1722, *45th AIAA/ASME/ASCE/AHS/ASC Structures, Structural Dynamics, and Materials Conference*, 2004.

[17] Leylek, E.A., Manzo, J.E., and Garcia, E. "A Bat-Wing Aircraft Using the Smart Joint Mechanism," *Advances in Science and Technology*, Vol. 58, 2008, pp. 41-46.

[18] Manzo, J.E., and Garcia, E. "Methodology for Design of an Active Rigidity Joint," *Journal of Intelligent Material Systems and Structures*, Vol. 20, 2009, pp. 311-327.

[19] Norberg, U.M. "Some advanced flight manoeuvres of bats," *Journal of Experimental Biology*, Vol. 64, 1976, pp. 489-495.

[20] Pennycuick, C.J. "Gliding flight of the dog-faced bat *Rousettus aegyptiacus* observed in a wind tunnel," *Journal of Experimental Biology,* Vol. 55, 1971, pp. 833-845.

[21] Norberg, U.M. "Morphological Adaptations for Flight in Bats," *Bat Biology and Conservation*, Smithsonian Institute Press, Washington, 1998, pp. 93-108.

[22] Neuweiler, G. *The Biology of Bats*, Oxford University Press, New York, 2000, pp. 9-40.

[23] Wickenheiser, A.M. and Garcia, E. "Aerodynamic Modeling of Morphing Wings Using an Extended Lifting-Line Analysis," *Journal of Aircraft*, Vol. 44, No. 1, 2007, pp. 10-16.

[24] Drela, M. "XFOIL: An Analysis and Design System for Low Reynolds Number Airfoils," *Low Reynolds Number Aerodynamics*, Springer-Verlag, New York, 1989, pp. 1-12.

[25] Leylek, E.A., Manzo, J.E, and Garcia, E. "Analysis of Bat Wings for Morphing", Smart Structures and Materials 2008: Active and Passive Smart Structures and Integrated Systems II, March 10-13, San Diego, CA., *Proceedings SPIE*, Vol. 6928, 2008.

[26] Pamadi, B.N. *Performance, Stability, Dynamics, and Control of Airplanes*, AIAA, Reston, 1998, p. 56.

[27] Raymer, D.P. *Aircraft Design: A Conceptual Approach*, AIAA, Washington, 1989, pp. 50-51,467.

[28] Corona, A. Marchesi, M., Martini, C., and Ridella, S., "Minimizing multimodal functions of continuous variables with the 'simulated annealing algorithm,'" *ACM Transactions on Mathematical Software* 13, 1987, pp. 262-280.

[29] Goffe, W.L., Ferrier, G.D., and Rogers, J. "Global optimization of statistical functions with simulated annealing," *Journal of Econometrics*, Vol. 60, 1994, pp. 65-99.

[30] Manzo, J.E., Leylek, E.A., and Garcia, E. , "Drawing Insight from Nature: A Bat Wing for Morphing Aircraft," ASME Conference on Smart Materials, Adaptive Structures and Intelligent Systems, October 28-30, Ellicott City, MD, 2008.

This chapter originally appeared as:

Leylek, E., Manzo, J., and Garcia, E., "Bat-inspired wing aerodynamics and optimization," *Journal of Aircraft*, Vol. 47, No. 1, 2010, pp. 323-328.

CHAPTER 3

METHODOLOGY FOR DESIGN OF AN ACTIVE RIGIDITY JOINT[1]

1. Introduction

Within the realm of airframe design, there falls a class of vehicles known as 'morphing aircraft'. This type of aircraft is capable of macro-scale shape change in flight, aimed at creating multiple, highly functional operating points. Many devices, including adjustable ailerons, flaps, and slats, fall into this category. With the aid of modern engineering materials however, new attention has been given to more radical morphing maneuvers such as span, wing twist, and camber change, all in an attempt to more efficiently control aerodynamic parameters than can current-day commercial aircraft. The Wright Brothers knew that much could be gained by borrowing shape change concepts from biological fliers such as bats and birds, and as such designed wings that could twist in order to experiment with different flight parameters. Now, with better materials technology, this concept can be extended beyond determination of operating points for single mission vehicles, and instead to expanding a flight envelope to cover multiple aerodynamic regimes. This may allow a vehicle to be designed capable of functioning not just as a high-endurance or fast-dash vehicle but perhaps as both, depending on mission demands.

Many concepts have been proposed for actuating these morphing vehicles. Variable geometry truss mechanisms have been developed in bench models, along with tensegrity structures and devices employing both linear and rotary DC actuators

[1] From Manzo, J. and Garcia, E., "Methodology for design of an active rigidity joint"; reprinted by permission of the Journal of Intelligent Material Systems and Structures.

(Moored and Bart-Smith, 2005; Abdulrahim and Lind, 2004; Wiggins *et al.*, 2004). These mechanisms are generally complex due to their redundant coupling of actuators and structural members, their mechanical linkages, and their design methodologies, the latter especially true for tensegrity structures. Morphing mechanisms are generally weight-intensive, expanding geometric capabilities but compromising flight-worthiness in terms of payload capacity or range. This tradeoff typically results in designs that perform shape change well in bench-top models, but that are completely impractical. Further, the mechanisms generally rely on a very simple basic physics principle: apply a force about a large enough moment arm to cause a rotation or torque with some consequent movement. This concept is demonstrated in the design of the HECS wing as well as the Lockheed Martin morphing concept vehicle, among countless others (Manzo *et al.*, 2005; Love *et al.*, 2004). Morphing often requires the use of tendons or bulky rotational actuators to accomplish this, and although mechanisms can be highly effective at prescribing shape change, their drawbacks in terms of flightworthiness provide few practical applications.

Because the morphing actuator doubles as both rigid load-bearing element and structural manipulator, energy demands on morphing structures are both high and constant, as power is constantly required even to keep a mechanism in its nominal unmorphed state. Solutions range from heavy or bulky mechanical locking mechanisms to stepper motors or worm gears that cannot be back-driven, all of which increase take-off weight. One must rethink the design to eliminate the need for external morphing members mounted to a host structure, and instead to incorporate the actuation into the structure itself to reduce necessary space, weight, and power requirements.

In this situation, it is desirable to consider the use of compliant structures, which are thin flexible elements that may include sensory or actuation elements for high authority, low profile shape change. These types of structures have applications in many fields of joint and arm manipulation, including manufacturing, ambulatory robotics, and the devices used for gripping and haptic sensing in the medical industry (Kota *et al.*, 2005). Such compliant structures, which make use of flexures as the primary rotational element, allow for large scale kinematic shape change on very compact and low wear host structures (Vehar *et al.*, 2004). Compliant structures are typically used on high precision structures due to their well-behaved kinematics (Trease *et al.*, 2005), but rarely possess the embedded actuators necessary to create motion from within the structure itself. Work is being done on distributed actuation and sensing within the compliant framework (Trease and Kota, 2006), but discretely mounted actuators have provided the primary means of prescribing motion.

Now that materials such as piezoelectrics, shape memory polymer, and shape memory alloy are available, composite structures with embedded actuation have been developed that demonstrate properties of the ideal compliant element. Such composites can function as actuators, or as elements with variable rigidity, or both. Devices of this nature have been used for flutter control in active structures (Lazarus *et al.*, 1996), and shape memory alloy has been embedded into plate structures to alter mode shapes, effective stiffness, and sag due to gravity (Rogers *et al.*, 1991; Maji *et al.*, 2004, Kim, 2006).

A compliant composite element such as this is proposed in the form of an 'Active Rigidity Joint', which is thermally activated and passively rigid in ambient conditions. The Active Rigidity Joint is embedded with both strain actuators and elements of

variable elastic modulus to control both stiffness and deflection, removing the common design guideline of actuators mounted externally to the compliant structure (Lagoudas *et al.*, 1997; Chaudhry and Rogers, 1993). Instead, this joint acts both as a self-contained actuator and actively deformable structural element, possessing high stiffness in its passive state but allowing both a reduction in stiffness and the ability to actuate to a particular shape when energized. In doing this, the joint consumes no power during the passive phase, and minimizes the weight and complexity required for a morphing mechanism. The joint can be inserted along hinge joints of a skeleton to replicate biological movements without the complexity of surrounding musculature, or can be used in any situation to reduce complex rotary actuators to simple compliant mechanisms. It moves one step beyond mimicking the biological structure, as the hinge joint will now contain its own actuators in a discrete package. An analysis on the thermomechanical behavior of this joint from first principles by the method of Wang and Rogers (1991) is modified and expanded to describe its kinematics and actuation envelope in terms of its material properties and external loading, and proves that the joint is a viable next step in compliant joint design.

2. Active Rigidity Joint Design

The function of the Active Rigidity Joint is to transition quickly between geometrical configurations through actuation such that the start and end conditions are stiff in bending and require no power consumption to maintain rigidity. The compliant joint morphs between passive, cooled configurations in finite time intervals, blending structure with actuating element. Furthermore, due to a symmetric design about the centroidal axis, the joint can function as a bimorph actuator, such that bending can be achieved in both directions as needed.

To create a structure capable of both adjustable bending stiffness and actuation on demand, a careful arrangement of materials is proposed. The joint configuration proposed is a composite of five layers using three materials. It makes use of shape memory alloy (SMA) as face sheets along with shape memory polymer (SMP) for core material, along with nichrome wire to provide additional heating (Brown and Hodgson, 2000; Reed *et al.*, 2005). SMA is able to contract when heated above its transition temperature, and serves as a strain actuator for the structure when energized. The polymer serves as the variable rigidity element, as its elastic modulus decreases significantly when heated. The nichrome core is used to decouple the heating of the SMA from its actuation capabilities, and to increase bandwidth during the heating phase.

The primary actuation element in the joint is shape memory alloy. This material, consisting of two or more metals and chosen here in a nickel-titanium composition, demonstrates two different microstructure orientations that are affected by temperature, strain, and stress. The most compact form – austenite – is a body-centered cubic (BCC) lattice orientation formed when the temperature of the alloy is higher than its transition temperature T_H, shown as a range and discussed further in Section 2.2.2 (Tanaka *et al.*, 1995, Brinson, 1993, Mabe *et al.*, 2004). In the austenitic state, the stiffness of the material is higher than in its cooled martensitic state, and any loading beyond the yield stress will result in strain deformations as high as 10% (Brown and Hodgson, 2000; Ford and White, 1996; Brinson, 1993) with no additional increase in applied stress (see Figure 3.1A, point 2). Unloading this stress will allow the material to transition back to its BCC orientation with low strain (Figure 3.1A, point 1) in the process known as the ‘pseudoelastic’ or ‘superelastic’ effect.

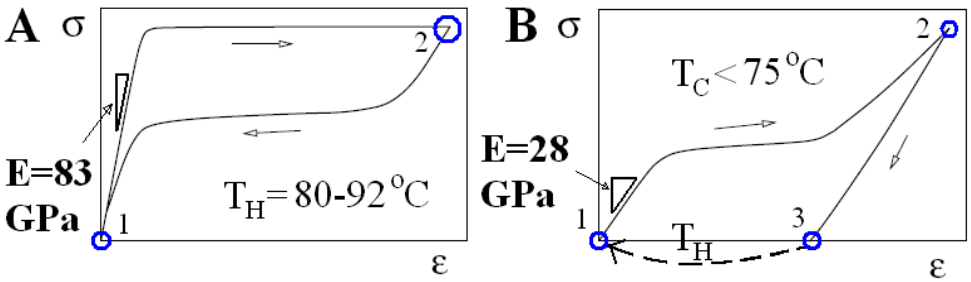

Figure 3.1 - Austenitic SMA demonstrating shape memory effect above its transition temperature (A) and compliant martensitic SMA below transformation temperature (B)

The usage of shape memory alloy in the Active Rigidity Joint makes use of its alternate mode of operation – the shape memory effect. As seen in Figure 3.1B, the cold SMA can be loaded and plastically deformed with much lower stresses to deform the material from a low strain to a high strain state after unloading, represented by the transition from points 1 through 3. These are all done at a temperature T_C below the transformation temperature, during which the SMA occurs as martensite, a monoclinic distortion with multiple variants which can be easily transitioned from the more compact twinned martensite state to an elongated, detwinned martensite configuration. The strain is recovered upon heating to T_H, shown in Figure 3.1B as the transition from detwinned martensite at point 3 back to austenite at point 1, which has the same strain value as twinned martensite once cooled. Another intermediate phase known as the R-phase exists, but it exists in low fractions and in very small temperature ranges, and therefore is not considered in this paper. For high cycle life, a deformation of 5% or less is recommended to preserve a consistent transformation strain without excessive permanent plastic strain (Miller and Lagoudas, 2001; Eggeler *et al.*, 2004).

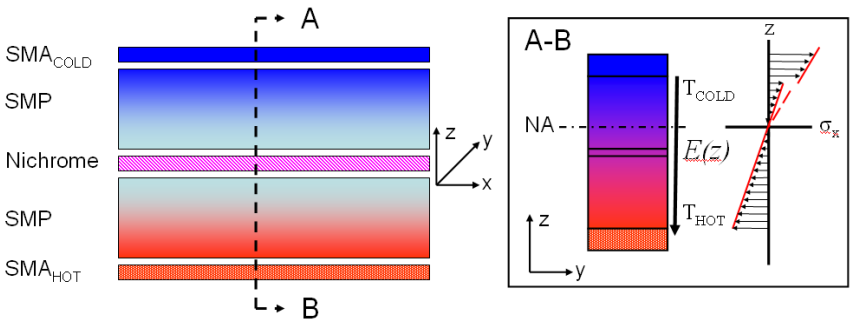

Figure 3.2 – Tri-phase Active Rigidity Joint showing morphology and temperature/stress profiles

The joint is formed by placing detwinned martensitic SMA prestrained to 5% strain at the exterior faces, with a core of SMP divided centrally by nichrome wire (see Figure 3.2), modeled as a slab rather than discrete wires embedded in a compliant epoxy for simplicity. Attachment to the host structure will still require a thin epoxy layer, which will add more complexity to the model in any real system with regard to heat transfer capabilites and mechanical response. Corrections for this adhesive layer can be added to reflect fabrication methods, but their effects on the thermal distribution have shown to be low for thin (1-3 mm thick) epoxy layers (Umezaki, 2006) and they will serve to be advantageous in further decoupling thermal from mechanical response of the SMA. Change in mechanical response with additional epoxy layers can also be reduced by keeping this layer as thin as possible, as some models fully remove the epoxy layer from mechanical response (Lagoudas *et al.*, 1997).

The SMA is heated to its transition temperature at the lower face by attaching electrodes to each end of the plate and using resistive heating at a controlled current and with a known resistance according to the heat transfer model of Section 2.2.2, forcing the transition from cooled, detwinned martensite (Figure 3.1B point 3) to its contracted austenitic phase (Figure 3.1B point 1). In the Active Rigidity Joint, as the heated SMA recovers strain by contracting along the length of the joint, it will provide

sufficient stiffness to overcome the stress induced by bending the remaining structure. This will in turn yield a net curvature along the centroidal axis towards the actuator face.

Energizing the SMA yields both a bending moment on the structure and a thermal gradient mediated by convective cooling at the upper and lower faces of the composite. In order for a rotation to occur, the structure must have a sufficiently low elastic modulus for the SMA to actually contract. To resolve this, the stiffness of the remaining structure is determined primarily by the other critical component of the Active Rigidity Joint, the shape memory polymer. This polymer has the unique property of a temperature-varying elastic modulus with recoverable strain deformations as high as 200% (Everhart *et al.*, 2004). This modulus change is due to weakening of the cross-linkages between polymeric chains within the styrene-based thermoset plastic at temperatures above the glass transition point of the polymer T_G, with subsequent reorganization and stiffening upon cooling (Cullen, 2003). The flexural modulus of the polymer can be reduced by as much as a factor of 100 when the temperature is raised sufficiently above T_G, as seen in Figure 3.3 (Liu *et al.*, 2003). Therefore, as the temperature increases from heating the SMA and nichrome and raises the SMP temperature above T_G, the polymer will develop increased compliance throughout the core of the joint. When heated, the joint will rotate given the combined contractile force of the SMA and reduced modulus of the SMP. This rotation assumes there is sufficient bending moment induced by SMA strain actuation about the neutral axis to overcome both flexural stiffness and external loading. Upon cooling, the structure can be set in its new deformed shape once the polymer cools by using the tri-phase heating technique to ensure the bending deformations are not lost during the

cool down phase. Alternatively, the flat state can be recovered by using the shape memory effect of the polymer, as described in Section 2.3.

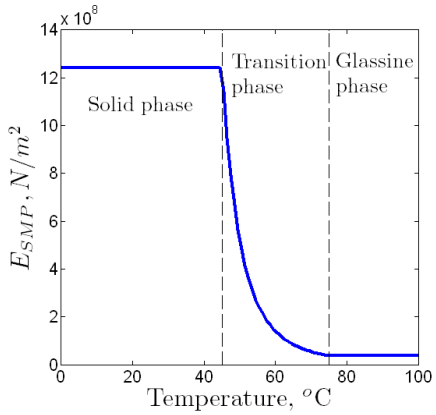

Figure 3.3 - Shape memory polymer modulus distribution with phase states

While a wide variety of polymers possess a temperature-dependent elastic modulus, the shape memory polymer has some unique properties. To understand these, a description of the chemical structure is required. While heated above T_G, the micro-crystalline bonds formed by the cross-linker melt and leave only the permanent aggregate bonds of the polystyrene matrix. This breakdown allows the polymer to be stretched to many times its original length, requiring stresses on the order of 1 MPa (Irie, 1998). Upon cooling, the polymer loses its elasticity when new micro-crystals form in the cross-linking component, fixing the deformed shape by preventing the aggregate shapes from realigning. As opposed to a metal, the polymer will be frozen at the elongated strain without providing a restoring force on the environment, provided that the temperature is kept within the solid range of Figure 3.3. Once reheated above T_G, the micro-crystals break down and the polymer returns to its original shape, recovering the strain that was frozen in place by the earlier loading and providing a weak (0.5-1.5 MPa) recovery stress (Irie, 1998). The strain recovery fraction is dependent on the initial strain value, but for strains under 20%, nearly all of

the strain can be recovered (Cullen, 2003). SMP can therefore withstand many loading cycles in its glassine phase with repeatable strain values and without degradation to its mechanical properties. Though this strain recovery is not unique to SMP, it is selected for two different applications; first, it serves as the variable rigidity element with known properties, and second, the recovery stress generated during realignment can be used to reset the joint to its flat configuration and acts as a weak biasing force to strain the twinned martensite into its detwinned variant, as discussed in Section 2.3.

As the last component of the joint, the nichrome serves as a heat source to assist in raising the temperature of the polymer layers above their transition temperature T_G without overheating the SMA actuator. This allows greater control of the thermal profile and enhances the longevity of the SMA, which loses cycle life with excessive heating above the transition point (Brown and Hodgson, 2000). It is primarily an artifact of the need to decouple the two roles of the SMA as both actuator and heat source, and as such could be replaced with other heat generating elements if needed. It also serves as an elastic element, however, and is necessary to provide a biasing force for restoring the austenitic SMA to its stretched state for cycling purposes, as described in Section 2.3. If the nichrome is removed, another elastic element would be required at the core, as the SMP does not provide enough restoring force through its own shape memory effect to restore the flat configuration when it is desired.

2.1. Tri-Phase Heating Process

For the joint to move between passive states, it must follow a specific thermal cycle to attain the correct mechanical properties at steps along the transformation. In the first

step, described above, the material is heated quickly by both the SMA and the nichrome layers, illustrated in Figure 3.4A. This heating uses both materials in order to maximize energy delivery to the system in the shortest period, and will ultimately yield curvature towards the contracted SMA face with high compliance in the structure due to the reduced stiffness of the SMP. During cooling, it is important to consider that one of the two heat sources – the SMA actuator – is also providing the contraction force necessary for deformation. Therefore, cooling this element before cooling the rest of the structure will cause undesirable deformations as the structure becomes back driven by flexural rigidity and external loads. The structure would simply return to its nominal state if the contractile force of the SMA actuator were removed immediately after phase one deformation had occurred, since the heated polymer offers little resistance to bending.

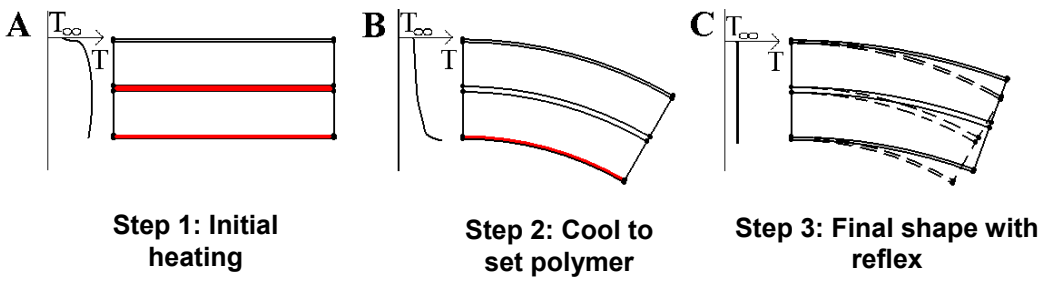

Figure 3.4 - Tri-phase heating depiction, energized elements shaded

Instead, it is desired to bring the temperature back to ambient conditions so that deflection is maintained while the temperature is reduced. This cooling path will result in a joint with high stiffness, a strong holding force against external moments, and with no energy consumption required to maintain shape. The process requires de-energizing the nichrome layer while maintaining heat on the SMA, in order to maintain the contraction on the lower SMA face until the polymer has regained enough rigidity through cooling to withstand external loading. With heating of the

nichrome disabled, the structure assumes an intermediate thermal profile (Figure 3.4B) heated only at the bottom face by the SMA and cooled convectively at both the outer faces. The thermal profile needs only to maintain heat local to the SMA actuator in order to maintain strain actuator force while allowing the majority of the polymer to cool quickly, except for polymer adjacent to the heat source. The desired thermal profile is shown qualitatively to the left of Figure 3.4B, where the temperature is at a maximum near the heated SMA and quickly decays to ambient temperature throughout the rest of the joint. Once this phase reaches equilibrium, heat from the SMA is removed and the structure is cooled completely, locking it into the final state (Figure 3.4C) with a final deflection at some value between the flat state and the phase one deflection, taking into account some bending relaxation to be minimized in the analysis below.

In these three steps, the joint can move between cooled configurations requiring zero energy input in the passive state. In order to accomplish this, a few requirements must be satisfied. First, if the heat were to propagate through the entire composite and heat the 'cold' SMA layer at the opposite face sufficiently to reach austenite, both upper and lower faces would contract, and compression would occur rather than bending. This requires that the temperature of the upper face be kept well below (>10 ^{o}C) the 90 ^{o}C transition temperature T_H of the material, or more specifically, the starting transition temperature A_s' of the unloaded SMA as described in Section 2.2.2. Second, it is crucial that the glass transition point of the polymer (T_G = 60 ^{o}C) be exceeded by at least 15 ^{o}C throughout the core in order to decrease the stiffness enough for initial contraction, so long as it avoids the melting region that occurs well above 150 ^{o}C (Cullen, 2003). The material properties of the SMA and SMP happen to let these two issues coalesce in a 5 ^{o}C temperature range, wherein the junction between shape

memory polymer and SMA is within the polymer's glassine phase onset but below the trigger for SMA contraction. This temperature range avoids pure compression and allows for generation of a bending moment induced on the structure by the SMA actuator.

As mentioned above, it is important that the actuator moment from the austenitic SMA about the neutral axis be greater than the sum total of external loads and counter-moment applied by the rest of the structure in resistance to bending. Otherwise, the system can be back-driven by the external loads, and heating the SMA will not yield contraction but will instead plastically deform or fail. Furthermore, after overcoming all of the loading and therefore allowing the SMA to contract and induce bending in the structure, it is important that the final deflection is substantial (defined as percent camber, the ratio of change in tip deflection to joint length and ideally 5-10%). Increased camber will increase the necessary moment the actuator must apply to overcome structural stiffness, making it important not only to overcome external load and maintain shape but to deform the structure beyond the nominal state, with increased resistance as camber increases.

The layering of the joint strongly influences the behavior during a full cycle of actuation. This behavior includes tip deflection, speed of response due to modifying thickness of heat generating elements, and holding force or resistance to external moment. Some of these effects are confounding, however. For example, increasing the thickness of the nichrome layer will speed the thermal process, but will increase the structure's stiffness to the point where little or no deflection can be generated by the SMA. It is therefore necessary to analyze the interactions of these effects to determine the capabilities of the joint as a complete system, in order to minimize such

quantities as power consumption for a single actuation cycle and maximize such properties as passive stiffness and tip deflection or camber.

2.2. Strain-Energy Model

Simple models for induced strain actuators have been proposed to represent the contribution of a patch actuator as a moment couple at the ends of the patch dependent on a fixed strain value independent of structure stiffness (Gaudenzi and Barboni, 1999). These types of models are useful for describing piezoelectrics as patch actuators, and have been successfully demonstrated in numerous works in both one-dimensional (Chaudhry and Rogers, 1993; Kapuria, 2001) and two-dimensional cases (Sullivan, Hubbard and Burke, 1996; Lim and Lau, 2005) for use in vibration suppression or isolation, sag compensation, and tip manipulation. In this application however, SMA actuator strain is constrained by the structure upon which it is laminated, acting not just as a moment couple at ends of the patch but also with strain continuity at the laminate interface. To resolve this issue, a method is proposed to incorporate the variation of actuator strain with system resistance. By the method of Wang and Rogers (1991), the system can be decoupled into two components – the SMA actuator and remaining structure. An Euler-Bernoulli beam with ideal bonding between layers is assumed, taking the form of a cantilevered beam with structure bonded at both ends to avoid shearing forces at the tip of the beam. A conservation of strain energy forms the basis for the analysis, and purely elastic deformations are assumed for the SMP, nichrome, and upper SMA sheet, which are all well within their elastic regimes for the deformations to be encountered (less than 5% for the SMP, 3% for others due to strain distribution). The polymer is elastic up to at least 25% strain (Abrahamson *et al.*, 2002; Wilson *et al.*, 2005) when in its heated phase and up to 5%

in its cooled phase (Gross and Weiland, 2007), making it very well suited to this application.

2.2.1. Phase One: Initial Heating

In the first part of the analysis, actuation due to heating the structure with the lower SMA element and the nichrome core is considered. At the end of this phase, the joint will have deformed to its peak value, but this does not reflect the complete transformation. The following section regards the model for an intermediate deflection value that can be used to predict maximum deflections, stiffness, and response time. This stage of the model describes the behavior at the end of step 1 in Figure 3.4, whereas the final deflection after cooling is found in Section 2.2.3.

The free strain of the SMA actuating layer is Λ, although this strain can only be achieved without loading. When subjected to resistance from the remaining structure in the form of bending stiffness, a scaling constant K must be used, such that the actuator takes on a functional strain $\varepsilon = K\Lambda$. The unknown K is a function of the linear strain distribution of the remaining system, with a maximum of $K\Lambda$ at the SMA actuator/structure boundary and a minimum of zero strain at the upper face.

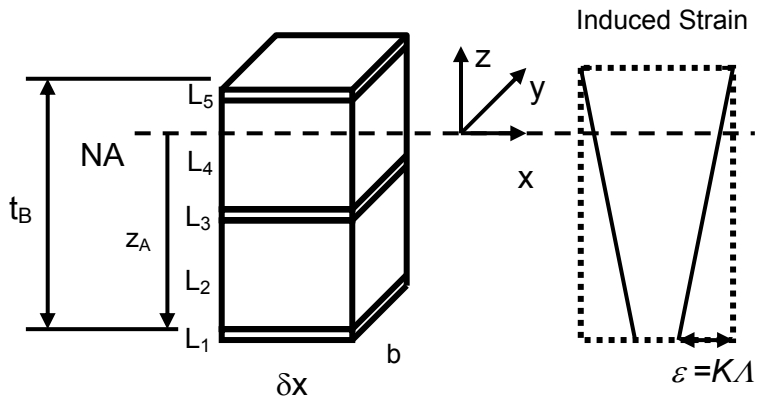

Figure 3.5 - Label convention and strain distribution

The strain on the actuator is the difference between free and induced strain, and is expressed as

$$\varepsilon_A = \Lambda - \varepsilon = (1-K)\Lambda \tag{1}$$

such that the actuator, which is contracted when heated under zero external stress, is placed in tension by the stiffness of the neighboring component layers resisting the compressive deflection. This desired contraction Λ is prescribed by the temperature to which the SMA is heated as well as its material properties, and is controlled to be within the practical bounds for high cycle life of the SMA (5% chosen, for 10^5-10^6 cycles). The moment applied by the actuator on the structure is therefore the product of the force applied by the SMA actuator times its distance from the neutral axis:

$$M_A = z_A L_1 b \sigma_A = z_A L_1 b E_A (1-K)\Lambda \tag{2}$$

where the subscript 'A' represents the SMA actuator, and a subscript 'S' will represent remaining structure. The counteracting moment applied by the structure as a consequence of deformation is

$$M_S = \int_{-Z_A}^{t_b - Z_A} \sigma_S z b_S dz \tag{3}$$

which is the moment about the neutral axis, and by examination of the strain distribution, can be rewritten as

$$M_S = \lambda K b_S \Lambda \tag{4}$$

$$\lambda = \frac{\int_{-Z_A}^{t_b - Z_A} E(z)\varepsilon(z) z dz}{K\Lambda} \tag{5}$$

The resultant λ is now a function of the temperature-varying elastic modulus throughout the thickness of the structure (assumed identical at all cross-sections along the length due to insulated thermal properties on all but the upper and lower faces), which can be approximated by a thermal model as based on the heating path discussed in the next section. The modulus distribution of the polymer can be modeled using the method of Tobushi *et al.* (2001):

$$E = \begin{cases} E_G \, e^{a\left(\frac{T_G - T}{T}\right)}, & T_G - T_W \le T \le T_G + T_W \\ E_{COLD}, & T < T_G - T_W \\ E_{HOT}, & T > T_G + T_W \end{cases} \tag{6}$$

with glass transition temperature T_G = 60 °C, a windowed temperature range T_W = ±15 °C around T_G in which the elastic modulus of the polymer has a logarithmic dependence on the temperature, and elastic modulus E_{COLD}=10(E_G)=100(E_{HOT})=1.24 GPa, as shown in Figure 3.3 (Tobushi *et al.*, 2001; Cullen, 2003). This, and material properties for both SMA and nichrome (Brown and Hodgson, 2000), can be used to generate the corresponding modulus distribution to solve for λ in Equation (5).

By sum of moments on the cross-section, combining Equations (2) and (4) with an external moment yields

$$K = \frac{z_A b E_A L_1 \Lambda - M_{EXT}}{\lambda b \Lambda + z_A L_1 E_A \Lambda b} \tag{7}$$

In this way, either the strain constant K can be found for arbitrary external moment, M_{EXT}, or the maximum moment tolerated by a particular deformation $K\Lambda$ can be determined. The beam deflection is approximated by the Euler-Bernoulli model:

$$\frac{d^2 w}{dx^2} = \frac{M(x)}{EI_{YY}} \tag{8}$$

with sign conventions as in Figure 3.5. For the simple case of the cantilevered beam with an external moment and no transverse loading, this simplifies to the following:

$$w(x) = \frac{M_S x^2}{2EI_{YY}} \tag{9}$$

Using I_{YY} found by the method of equivalent sections (Shames, 1975) for an arbitrary material within the composite, tip deflection can be found representing attainable operating points with regard to external load and element thicknesses.

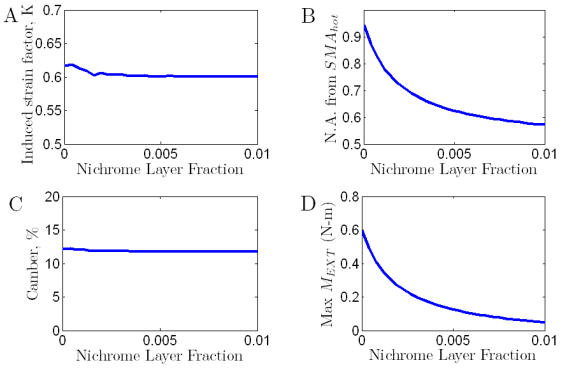

Figure 3.6 - Strain factor K, neutral axis (from actuator), tip deflection vs nichrome fraction

The results of phase one heating for a joint of dimensions 1" long by 0.5" wide by 1/8" thick (25.4 mm by 12.7 mm by 3.2 mm) are shown in Figure 3.6 for a variation in nichrome layer thickness as it pertains to neutral axis location (Figure 3.6B) and, more importantly, to maximum external moment tolerance (Figure 3.6D). The induced strain factor *K* was not allowed to decrease below a value of 0.6 in this simulation (Figure 3.6A), corresponding to a 3% contraction at the lower face of the joint, and generating a consistent tip deflection of around 12% camber for all cases tested (Figure 3.6C). In this configuration, the percentage composition by volume of nichrome can reach up to 2% (<1% needed for adequate heating within 1 second) before the stiffness of the structure prohibits any deflection. More importantly, while the Active Rigidity Joint may be able to deform to 12% camber, at higher nichrome fractions the system can't handle any external moment, indicating a low enough bending capability that the joint becomes back driven and therefore impractical. In order to maintain usefulness, a significant holding force must be retained, at least on

the order of 0.5-1.0 in-lb (0.056-0.112 N-m) of available torque for the 1" (25.4 mm) long structure.

This cutoff value for nichrome fraction indicates the edge of a curve bounding structure stiffness with large holding force in the presence of external moments, tip deflection, and response speed. While the nichrome fraction could be increased to speed heat delivery, the deflection would be compromised in order to withstand any loading. It is desirable to optimize many of these quantities to generate the most functional joint capable. Functionality could refer to fast thermal response due to more powerful heat sources, to maximum tip deflection, to maximum holding force when actuated in the presence of high external loads, or to any combination of these factors. As such, the Active Rigidity Joint can be tailored to the user's needs by selecting design criteria and optimizing the composite layering to meet desired goals.

The model of Equations (1)-(9) is also applicable to a laminated beam of alternative configurations; for example, the SMA layer can be moved internally to the structure rather than at the face by modifying the strain distribution of Figure 3.5 for use in Equation (5). The nichrome can also be replaced or supplemented with any other elastic elements, and the SMP can be replaced with a thermoplastic if the memory effect used in Section 2.3 is not desired, changing only the distribution of elastic modulus throughout the thickness in Equation (5).

2.2.2. Thermal Considerations

During phase one heating, a thermal model is used to determine the temperature profile throughout the thickness of the joint from first principles (Bejan, 1993). It is

desired to shape the profile such that the temperature of the polymer is raised above its transition temperature (assumed 75 ^{o}C for full compliance), that the upper SMA face sheet has not yet reached the onset of its transition regime to avoid a pure compression mode, and that the lower SMA face sheet has moved through its full transformation temperature range. When heating the SMA to austenite, the start and finish temperatures are determined not only by the alloy composition, but also by the applied stresses (Huang, 1998; Tanaka *et al.*, 1995; Troisfontaine *et al.*, 1999). Following the method of Liang and Rogers (1990) and removing the thermal strain term (Manzo, 2006), the transition to austenite is determined by the set of equations

$$\begin{aligned} &\sigma - \sigma_0 = E(\varepsilon - \varepsilon_0) + \Omega(\xi - \xi_0) \\ &\xi^{M\to A} = \frac{\xi_0}{2}\cos\left[\frac{\pi}{A_f' - A_s'}\left(T - A_s' - \frac{\sigma}{C_A}\right)\right] + \frac{\xi_0}{2} \\ &C_A(T - A_f') < \sigma < C_A(T - A_s') \end{aligned} \tag{10}$$

where Ω is the phase stress tensor, ξ the martensite fraction, C_A the slope of the stress-temperature curve for austenitic SMA, and A_s' and A_f' the austenite start and finish temperatures respectively. The term C_A is quoted as 13.8 MPa/^{o}C by Brinson (1993), and so, for SMA selected with a no-load activation temperature of 80 ^{o}C assumed as A_f', a range of start and finish temperatures exist that are functions of the loading on the SMA, as predicted by the Clausius-Clapeyron relationship (Troisfontaine *et al.*, 1999). Working close to the yield stress of the SMA at 172 MPa (25 ksi), the stress-adjusted finish temperature A_f' is increased to 92 ^{o}C, with A_s' 5-10 ^{o}C below this value (Tanaka *et al.*, 1995; Zak *et al.*, 2003; Brown and Hodgson, 2000). So, for the unheated SMA sheet at the upper face which will be subjected to low stress/strain conditions as in Figure 3.5, the temperature must be kept around 75 ^{o}C (below A_s' at low stress) or lower to be certain no austenite is formed. On the opposite face, the

heated SMA under high stress must be able to reach at least 92 ^{o}C for a full transformation to austenite while under load.

The ideal solution would resemble a profile shaped like that accompanying Figure 3.4A, where the temperature is above each material's transition point at all but the upper SMA layer. For the steady-state solution, the resistive heating method of a standard thermal analysis yields the coupled equations

$$\begin{bmatrix} h+\frac{k_1}{L_1} & -\frac{k_1}{L_1} & \frac{k_3}{L_3} & -\frac{k_3}{L_3} & 0 & 0 \\ 0 & -\frac{k_2}{L_2} & \frac{k_2}{L_2}+\frac{k_3}{L_3} & -\frac{k_3}{L_3} & 0 & 0 \\ -\frac{k_1}{L_1} & \frac{k_2}{L_2}+\frac{k_1}{L_1} & -\frac{k_2}{L_2} & 0 & 0 & 0 \\ -\frac{k_1}{L_1} & \frac{k_1}{L_1} & -\frac{k_3}{L_3} & \frac{k_4}{L_4}+\frac{k_3}{L_3} & -\frac{k_4}{L_4} & 0 \\ -\frac{k_1}{L_1} & \frac{k_1}{L_1} & -\frac{k_3}{L_3} & \frac{k_3}{L_3} & \frac{k_5}{L_5} & -\frac{k_5}{L_5} \\ -\frac{k_1}{L_1} & \frac{k_1}{L_1} & -\frac{k_3}{L_3} & \frac{k_3}{L_3} & 0 & h \end{bmatrix} \begin{bmatrix} T_A \\ T_B \\ T_C \\ T_D \\ T_E \\ T_F \end{bmatrix} = \begin{bmatrix} \frac{q_1L_1}{2}+\frac{q_3L_3}{2}+hT_\infty \\ \frac{q_3L_3}{2} \\ \frac{q_1L_1}{2} \\ \frac{q_1L_1}{2}+\frac{q_3L_3}{2} \\ \frac{q_1L_1}{2}+\frac{q_3L_3}{2} \\ \frac{q_1L_1}{2}+\frac{q_3L_3}{2}+hT_\infty \end{bmatrix} \quad (11)$$

Table 3.1 - Thermal properties used in phase one analysis. Ranged values indicate different configurations tested

q_1=1.17x10^8 W/m^3	q_3=1.54x10^8 W/m^3		
k_1=18 W/m-K	k_2=k_4=1.7 W/m-K	k_3=12 W/m-K	k_5=8.6 W/m-K
L_1=L_5=4.6x10^{-2} mm	L_2=L_4=1.6 mm	L_3=1.52x10^{-4} mm – 0.071 mm	

Here, q_i is the volumetric heat generation rate for a particular layer, k_i the thermal conductivity, T_∞ the ambient temperature, $T_A, \ldots, T_F$ the junction temperatures as shown in Figure 3.7, and h the convection coefficient. This is derived from the classical models (Bejan, 1993) for resistive heating with convective boundary conditions:

$$q_i = \frac{I_i^2 R_i}{vol_i} \tag{12}$$

$$h\left(T_{face} - T_\infty\right) = \sum_{i=1}^{m} q_i'' \tag{13}$$

$$q'' = \frac{k_j}{L_j}\Delta T \tag{14}$$

Here, the quantity I_i of Equation (12) represents the current sent to each heating element with resistance R_i. The model is concerned with the net heat flux through a surface q_i'' representing the contribution from each heat generating element, either by convection in Equation (13) or by conduction in Equation (14). Energy is added to the system using a simple resistive heating model for the nichrome and SMA layers, with current input varying at different points in the heating/cooling cycles and described at the end of this section. The convection coefficient is determined by free stream parameters for the particular application chosen, modeled in this paper as 80 W/m^2-K. This convection coefficient strongly influences the system bandwidth, as higher values represent a stronger forced cooling coefficient that can reduce the uncontrolled cooling stage of the actuation from a few seconds to well under one second for the size and shape of joint considered. The junction temperatures T_A,…, T_F can be shaped by varying the heat input from both the nichrome layer and the SMA layer to generate a profile similar to Figure 3.4A. The shape of the thermal profile is shown in Figure 3.7, with relative transition temperatures labeled qualitatively (not to scale). Heat generating elements yield a parabolic thermal profile affected by the overall boundary conditions, while passive thermal elements are strictly linear, affected by their thermal conductivity alone (assumed insulated on all but top and bottom faces). The SMA transformation regimes, marking the start and finish temperatures A_s' and A_f' separated

by 5 ^{o}C as described above, show the different stress-adjusted ranges below which the SMA is fully martensite and above which the SMA is fully austenite. It is therefore important that the upper face stay below the entire boxed range, and that the lower layer stay above the entire range, in order to ensure the proper phases. The upper face temperature boundary could be higher if the loading increases, while the lower face threshold temperature is assumed to be a known quantity as based on the yield stress of austenite. These quantities present a conservative estimate, and as such will form the minimum 17 ^{o}C temperature gradient necessary between the face sheets.

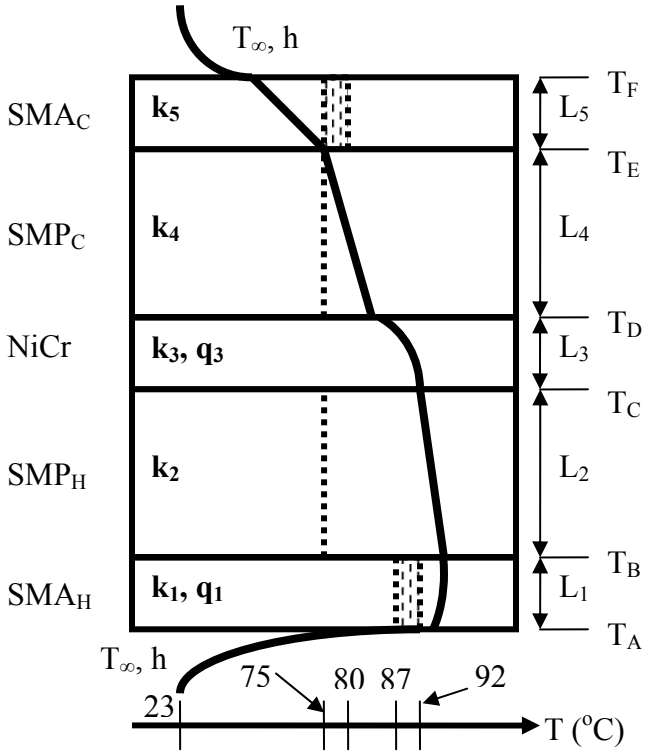

Figure 3.7 – Approximate thermal profile during phase one heating and terminology used in Equation (11), along with relative transformation temperatures shown as dashed lines or boxes

The volumetric heating rates q_1 and q_3 are affected by the electrical resistance and current sent to each source, as in Equation (12). Since the structural analysis

investigates the role of increasing the thickness of the central heating element, it is important to note its effect on response time. As nichrome fraction is increased, more power can be delivered as long as volumetric heat generation q_3 is held constant. The results are shown for various nichrome fractions in Figure 3.8 for an open-loop case where the temperature is not restricted once it reaches the threshold temperature. Neglecting the steady-state solution and looking at time to the 75 ^{o}C threshold, it is apparent that the rise time to the maximum desired temperature at junction T_E (from Figure 3.7) decreases significantly with increasing nichrome thickness. For 0.25% nichrome fraction, the system requires around 0.5 seconds and doesn't reach the desired temperature, whereas with 0.50% fraction it takes only 0.2 seconds, decreasing to approximately 0.05 seconds for 2.4% nichrome fraction. In order to reach the proper temperature, closed-loop control would have to be implemented with temperature sensing.

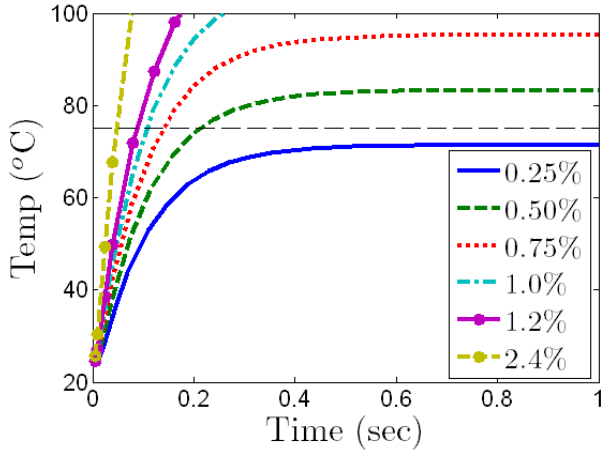

Figure 3.8 – Open loop rise times of temperature T_E with variation of nichrome fraction by volume with fixed volumetric heating rate q_3, desired to reach 75 ^{o}C (dashed line) in minimum time

The time required to heat the structure is greatly influenced by varying the thickness of the nichrome heat source, although it is important to consider the effects of

changing the thickness. Increasing the thickness of the nichrome layer affects load-carrying capacity by increasing structural stiffness, as described previously. It is best to keep the nichrome thickness low, and to instead increase power sent to the heat sources to increase bandwidth. A balance must be drawn however, as sending more power to the nichrome rather increasing the amount could potentially cause damage to the polymer by excessive heating local to the heat source, which reaches temperatures of around 120 ^{o}C in some configurations. This poses a challenge for control system delay as well, as temperature control may not be precise enough to vary the power effectively and to protect the components from overheating. Careful selection is therefore required both for the nichrome fraction and the heating rate it receives to ensure safe operation with useful deflection capabilities.

Another confounding effect might be the activation time of the SMA sheets, which may reach transition temperature before the full lattice reorientation occurs (Boyd and Lagoudas, 1996, Briggs and Ostrowski, 2002). If this were the case, the material would not actuate immediately in response to reaching the critical temperature, and faster heating times would lead to wasted energy while the SMA continues to contract after having reached its transition temperature, invalidating the analysis. To determine this would require further modeling of the SMA bandwidth and strain rates, such that increasing nichrome thickness to speed transformation should be secondary to maximizing deflection and passive stiffness.

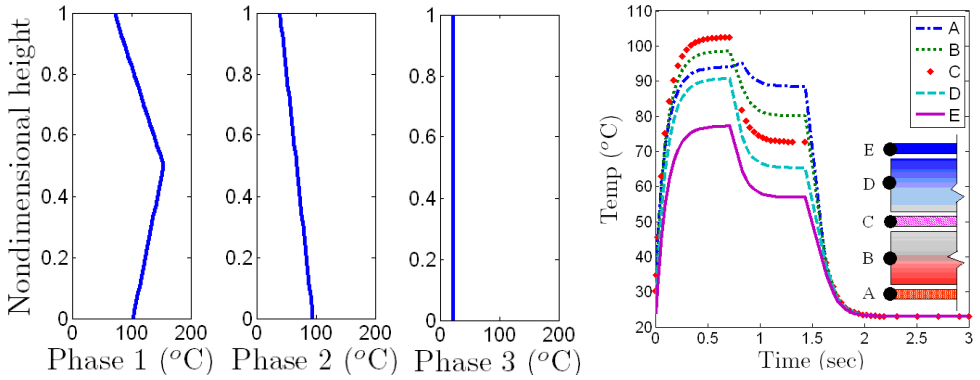

Figure 3.9 - Thermal time history across depth, where 0 is heated SMA actuator face, at end of each phase (left 3 snapshots) and at points A-D for full actuation (right plot)

The response time of a typical configuration (nichrome fraction 0.50% by volume) is shown in Figure 3.9, which shows the temperature distribution in two ways. The left three charts are snapshots of the temperature profile across the thickness of the joint at the end of each of the phases. The curves were generated by a thermal model in ANSYS as predicted by the heat transfer model of Equations (12)-(14), using known properties for the resistance of the two heating elements, along with the thermal conductivity and heat transfer coefficient for the system. The system is broken into three steps following the tri-phase process of Section 2.1; in the first, power is sent to the SMA and nichrome to exactly reach the 92 ^{o}C temperature required for full transformation of the heated SMA to austenite while keeping the upper face at exactly 75 ^{o}C. In the second step, the nichrome no longer receives power, and the current sent to the lower SMA sheet is increased to keep the temperature near the 90 ^{o}C transformation point at the bottom and below 60 ^{o}C at the upper face. This gradient represents the largest variation in temperature possible for this configuration, although the inclusion of an adhesive epoxy layer between SMA and host structure could increase this to bring the polymer temperature down further into its fully rigid temperature range below 45 ^{o}C, as epoxies have low thermal conductivity coefficients.

The last plot in Figure 3.9 shows the time history at five points along the depth of the joint as modeled by ANSYS – within the heated SMA (A), within the lower polymer layer (B), the nichrome core layer (C), the upper polymer layer (D), and at the upper cooled SMA (E). The temperatures at steady state, reached at approximately 0.8 seconds in the first step, 1.5 seconds in the second step, and by 2.2 seconds in the third step in the tri-phase process, follow the heat transfer models of Equations (12)-(14) to within 2 degrees at all points. This is based on careful tailoring of the current delivered across the ends of the SMA sheet, starting at a value of 0.85 A and increasing in the second step to 1.6 A before being de-energized completely in the final cooling step. Of note is the fact that the temperature at point (E) is kept at or below the start transition temperature A_s' of 75 ^{o}C at all times, while the temperature of the polymer is allowed to cool in the uppermost region while still maintaining the proper temperature on the actuator (point A). The 2-3 ^{o}C spike in the heated SMA is a result of increasing the current the SMA receives when the nichrome is de-energized, and can be eliminated in a real system with more than two open-loop control steps. Though not currently ideal, the general trend following that of Figure 3.4 is present, and a full actuation from ambient flat state to a morphed, cooled state can be accomplished in less than 2 seconds.

2.2.3. Tri-Phase Model

The structural calculations of Section 2.2.1 reflect a joint that has only been heated, and has not yet undergone the cooling phase described in steps 2 and 3 of Figure 3.4 and at their thermal profiles described above and shown in Figure 3.9. In order to calculate the final tip deflection at the end of step 3, where the structure is again consuming no energy and is at ambient temperature, another step is incorporated into

the model. This step accounts for restorative corrections when the polymer is cooled and SMA actuator strain has been removed. This follows a reverse process from that of Section 2.2.1, as the camber is now decreasing, and the SMA and nichrome are now being relieved of stress by relaxing their curvature. The polymer, having been deformed after breaking down the micro-crystals within the SMP through heating, is now stiffened during cooling. Once the system is cooled, the SMA actuator force is removed from the system and the stiffness of the elastic nichrome core is no longer compensated for by the actuator, such that the structure relaxes its curvature by bending towards the neutral axis. The SMP develops a tensile stress resisting this relaxation until an equilibrium point is reached between the polymer stress holding the structure in a curved state and the remaining structural contributions acting to return the structure to the flat state. In essence, the polymer now replaces the heated SMA as the strain actuator while the remaining materials relieve strain energy by bending towards the nominal flat state. The SMP deforms from a high compressive strain with no stress to an elongated shape with high tensile stress in its final state due to the elastic response of the other elements to initial deflection.

Taking the strain state at the end of the heating phase as initial conditions of the cooled phase, a new temperature profile can be found by solving Equation (11) with new heat generation conditions. Specifically, the core heating q_3 is reduced to zero as in Figure 3.4B, followed by reducing q_1 to zero as in Figure 3.4C, either in one step between fully heated and fully cooled as an approximation or in more discrete steps if a more precise solution is desired. Using the properties of the composite with cooled temperature profile, the method of transformed cross-sections is again applied to find the new neutral axis location at each point in time, adjusting the centroid as the polymer increases in stiffness and as the cooled SMA is transformed back from

austenite to the less stiff martensite state after the final cooling step. Balancing the moments of the nichrome and SMA developed by the initial stress conditions about the new neutral axis against the stiffness of the polymer, the final equilibrium moment distribution and corresponding deflection of the joint can be found.

To model this, another scaling parameter γ is introduced, representing the fraction of lower surface strain that is relieved after compensation by the polymer bending back to the flat state, ranging between 0 and K (see Figure 3.10, step B). By superposition of the original strain distribution with the contribution of a counter-rotation about the new neutral axis (Figure 3.10, steps A and B), the final equilibrium point can be determined (Figure 3.10, step C).

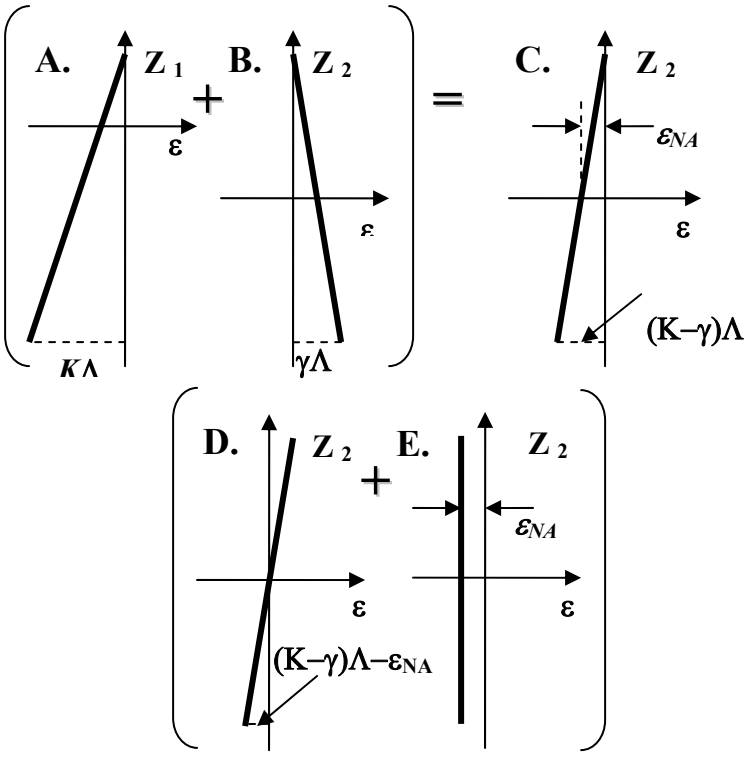

Figure 3.10 – Strain distributions showing recurve contribution (B) during phase 3 cooling, added to initial deflection during phase 1 heating (A), to yield a reduced amplitude strain distribution (C). The final distribution can be decomposed through superposition into a pure bending moment (D) and an axial compression (E)

The end result is a reduction in the strain along the thickness from the deformed shape created in the heated phase, yielding bending relaxation towards a flat shape. In addition to a bending moment about the neutral axis, the assumed strain distribution will induce a compressive force on the system, as can seen by the decomposition of the final strain distribution into two components: strain in direct linear proportion to distance from the neutral axis representing pure bending (Figure 3.10D), and the constant offset ε_{NA} apparent in the actual strain distribution to achieve zero strain at the neutral axis (Figure 3.10E). The compressive axial force P_{eq} is the integral of the elastic moduli of the layers times the depicted strain, ε_{NA}. These results are consistent with Wang and Rogers (1991) for the case of a unimorph strain actuator patch, which applies a moment while simultaneously inducing an axial force and is similar to the bimorph Active Rigidity Joint because only one actuator is energized at a time during operation. In certain applications, this axial force may be useful and should be a quantity to maximize. For the configuration and application of the Active Rigidity Joint described in this paper, however, the compression is of secondary concern, and will not be considered further.

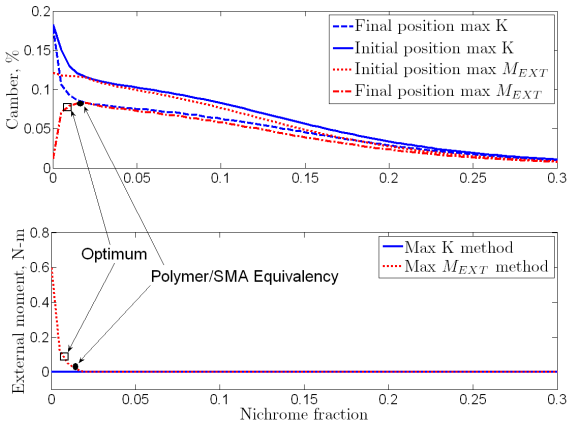

Figure 3.11 - Initial and final Active Rigidity Joint deflections about neutral axis for various loading configurations (upper plot) and maximum external moment at this deflection (lower plot)

The results for both the heated (intermediate) and cooled (final) deflections are shown in Figure 3.11, showing tip deflection in the cases of both maximizing K (max deflection) with zero external moment and maximizing M_{EXT} toleration with fixed K of 0.6 (3% SMA contraction). Both the initially heated and final cooled positions (Figures 3.4A and 3.4C, respectively) are plotted as nichrome fraction is varied, where nichrome acts as the stiffest elastic element and therefore will greatly decrease ability to deform under any load. What can be seen is that the external moment that the joint can tolerate, or the holding force of the cooled joint, quickly drops to zero as the stiffness of the nichrome core increases. This drop-off actually reaches the point where the joint will either be back driven or will demonstrate zero deflection with any external moment beyond a nichrome fraction higher than 2% by volume. This fact illustrates how critical it is to choose a design point that can not only overcome the expected internal stiffness encountered by large deflections, but also has high resistance to external forcing and a strong holding force upon cooling.

It is interesting to note the final deflection of the joint in varying configurations. Without external loading (max K method), the polymer is capable of providing sufficient rigidity to prevent significant recurve to the flat state, but with maximal loading for the smallest nichrome fraction examined, the polymer cannot tolerate the high loading and will deform back to the nominal state to account for the stress it experiences. This is due to the discrepancy between the stiffness of the austenitic shape memory alloy and the cooled shape memory polymer. The heated SMA is significantly stiffer than the rigid cooled polymer, such that when in the heated state, the contracted SMA may be able to overcome a certain amount of bending stiffness, whereas upon cooling, the stiff polymer is insufficient to retain all of the deflection that the austenitic SMA had prescribed without significant recurve. The effect is seen

at nichrome fractions below 1.5%, but increasing the nichrome fraction to remove this effect will also decrease holding force of the Active Rigidity Joint, as only 0.15 in-lb (0.017 N-m) external torque can be tolerated at this point, a value that drops to zero for higher nichrome fractions. On Figure 3.11, this is represented by a divergence between the initial position at the end of heating and the final position at the end of the cooling phases, having no net deflection upon cooling as nichrome fraction approaches zero, where structure stiffness is low and the joint is being completely back-driven by external loading. The point at which this effect disappears is marked as the polymer/SMA equivalency point in Figure 3.11, which is also near the onset of the back-drivable range.

A reasonable combination of retained deflection after cooling and holding capability in the presence of external loading occurs at nichrome fractions in the range of 0.5-1.0%. At this composition, the structure allows for a significant deflection upon cooling on the order of 8% camber, as well as a reasonable external moment capacity between 0.44 and 1.12 in-lb (0.05 and 0.127 N-m). The composition chosen depends on whether the user needs large rotations with weak external forces or smaller rotations with larger external forces, and therefore provides a framework for selecting a testbed configuration. In essence, nichrome thickness can be determined by moving along a force-speed-displacement curve for joint operation depending on desired response, where speed is strongly influenced by heat delivery through the nichrome, as in Section 2.2.2. Determining the relative costs for these three parameters will determine where along the curve in Figure 3.11 to operate when selecting composite layer thicknesses.

2.3. Flat Shape Recovery

While the joint is designed for use as a bimorph, one problem that might be encountered is the fact that after contraction of one of the SMA face sheets, the joint will not be able to restore itself to the nominal (flat) configuration. Contracting the opposing face sheet would then compress the structure to a straight beam 95% of its original length, and no further actuation would be possible. This situation can be avoided by making use of the shape memory advantages from both SMA and SMP, along with the rigid nichrome layer.

The resetting phase for transforming the SMA from cooled, twinned (contracted) martensite to detwinned (elongated) martensite is usually accomplished with a bias spring or some other restoring force. Since relying on external loading is undesirable, the internal forces of the joint can be used instead. This can be accomplished by an additional heating configuration beyond the tri-phase process of Figure 3.4. The nichrome core can be heated exclusively to bring the temperature of the joint to 75 ^{o}C at the junction of SMP and SMA, symmetrically as in Figure 3.12B. This will break down the micro-crystals of the SMP that hold the joint in its contracted shape as in Figure 3.4C, allowing compliance. It is at this point that three contributing factors will work together to restore the joint to its flat configuration, as in Figure 3.12C. The first and most significant of these is the earlier compression of the nichrome sheet to strain values of up to 2.5%, as seen in the strain distribution of Figure 3.5. For the same reasons that the joint will reflex as it cools in step 2 of the tri-phase process, the nichrome relieves compressive strain and provides a biasing force acting to stretch the twinned martensite into detwinned martensite until a balance of forces is reached. This is assisted by the second contributing factor – the shape memory polymer, which

can use its shape memory properties once heated and no longer subjected to the compression from the lower SMA to provide a recovery stress of 0.5-1.5 MPa (Irie, 1998; Liu *et al.*, 2003). The recovery stress is weak compared to the 2,000-5,000 MPa stress generated by the nichrome core however, as the nichrome at a thickness ratio of 0.25% is under 200 N compressive force, while the SMP can provide a maximum of 60 N force given its thickness. This is one of the problems with attempting to use the shape memory effect of the polymer to any real advantage in a laminate structure; the SMP recovery stress is about 1/100 that of SMA, making it much more useful as a variable rigidity element than as a component with useful shape memory effects. Still, the SMP provides up to a 23% contribution to the restoring force.

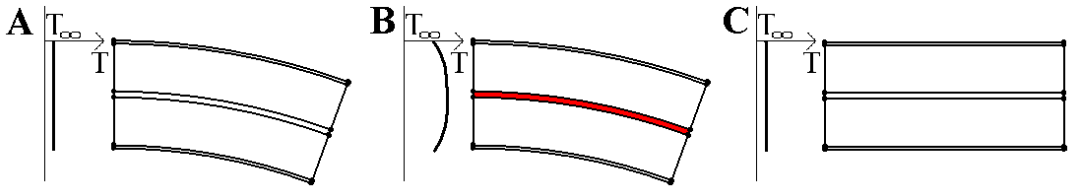

Figure 3.12 - Resetting the flat shape by energizing the nichrome core, starting from the final cambered state with reflex as in Figure 3.4C

The third effect which may serve to restore the joint is the two-way shape memory effect (TWSME), in which shape memory alloy which has been cycled under load develops a tendency to not only contract to an austenitic shape under heating, but also to return in part to its detwinned martensite configuration upon cooling (de Blonk and Lagoudas, 1998; Mabe *et al.*, 2004). The two-way effect has been shown to recover up to 4% of the contracted strain under the proper conditions, although a more realistic value is in the range of 2.5-3% after thermal cycling. If this effect were to be used, the SMA would have to be trained under specific conditions before use, and would require a composition with low amounts of cold working (20% or less) and high annealing temperatures (400 ^{o}C or higher) in order to allow plastic strain to accumulate – a

necessary condition for the development of the two-way effect (Miller and Lagoudas, 2001). While this two-way effect may not be enough to trigger the transition back to the fully flat configuration, it could be used as a contributing factor. The primary driver of this resetting phase is still the nichrome element, or any rigid elastic element placed at the core if nichrome were to be replaced. To trigger the transition from twinned to detwinned martensite, a stress of 70 MPa is required to exceed the yield strength of the cold SMA, requiring a force of only 40 N for the SMA thickness considered. This can be readily achieved with the nichrome, and perhaps even exclusively with the shape memory effect of the SMP if the quoted recovery stresses can be validated in laboratory conditions.

While this heating path will restore the flat shape, it may not be necessary for resetting the SMA to its detwinned configuration in multiple cycling applications. Antagonistic actuation of the tri-phase technique by energizing the upper SMA plate creates an adequate temperature profile without compression of the lower face to induce the same memory effects in the lower SMP layer and permit any two-way effect in the cooled lower sheet that may be built into the system.

3. Analytic Model Validation

Before fabrication is considered, verification of the model can be achieved using finite element simulations. Using the ANSYS finite element solver, a thermomechanical model was developed using known and assumed material properties, capable of phase one actuation, i.e. still in its heated state. Simple stress-strain relationships for the austenitic and martensitic phases of SMA were used, and a negative coefficient of thermal expansion was employed to generate contraction upon heating for the SMA

sheet. Taking one face of SMA and the nichrome core as resistive heating elements with the same volumetric power dissipation as that used in the analytical model, along with identical thermal boundary conditions, the temperature profile was matched within 4 degrees at every junction of the composite between models. Also, to avoid shear conditions at the free end, a block of high stiffness and low (<1% net contribution) mass was added to ensure Euler-Bernoulli planar section beam assumptions throughout the beam length, as seen in the meshed configuration of Figure 3.13.

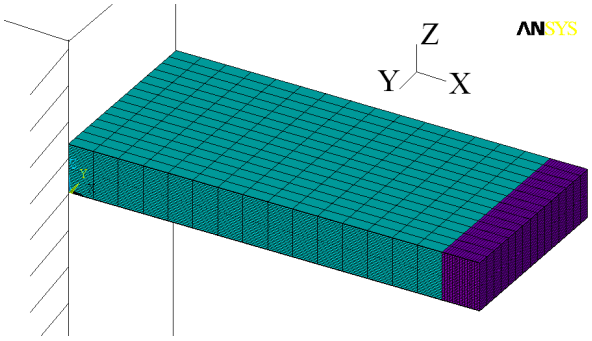

Figure 3.13 - Cantilevered beam showing mesh and massless tip segment (darker section)

The composite geometry was matched to analytical model conditions, and the case with no external moment was modeled. What can be seen from the results of Figure 3.15 is that the strain distribution is linear throughout the thickness, and that there is a much smaller stress contribution from the heated SMP than from the stiff elastic nichrome layer. Though still within the elastic regime, the SMP stiffness is low enough in its heated state to contribute very little to the net structural moment M_s of Equation (3). The strain distribution matches that of the assumed system fairly well, as seen in Figure 3.16, which is a section view of the strain distribution of Figure 3.15, far away from stress concentration effects at the tip. These concentration effects are

not modeled, but are assumed to have only a small contribution to the final deflected state of the joint.

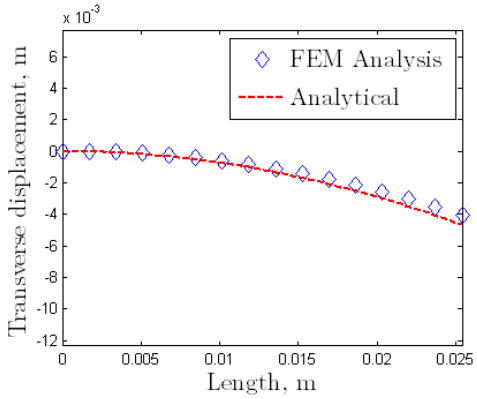

Figure 3.14 - FEM/Analytical model comparison

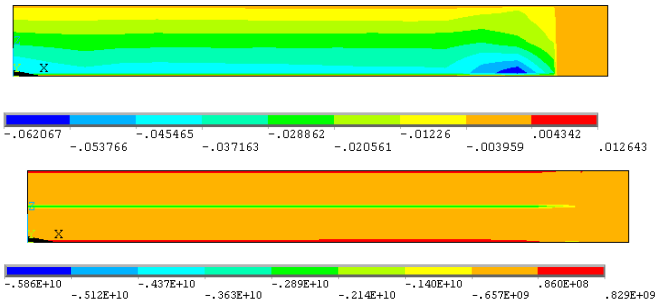

Figure 3.15 - Strain distribution (top) and stress distribution (bottom) for FEM Active Rigidity Joint model

The resulting deflection curve *w(x)* at the neutral axis is shown in Figure 3.14 for the full joint at a nichrome layer fraction of 0.24%, slightly below the optimum point established in analysis and seen in Figure 3.11. There is a discrepancy of approximately 2% between analytical and FEA methods, with the analytical model over-predicting deflection. This may be due to shearing within the heated SMA layer that isn't addressed by the analytical method, which explains the discrepancy in strain distribution along the Z-axis for the SMA seen in Figure 3.16, or from difficulties in

approximating the behavior of the polymer and the shape memory effect of the SMA in the FEM code.

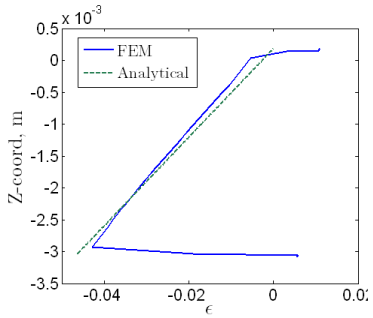

Figure 3.16 - Comparison of strain distribution for both models

4. Conclusions

The proposed model uses strain energy methods to demonstrate actuation between two passive states for conveying both bending moment and transverse deflection as based on layer thicknesses and structural properties. Using the tri-phase method to shape the heating paths of the composite layers, it can be shown that upon cooling, the joint can be set rigidly in place with a prescribed maximum deflection of up to 20% camber and capable of withstanding a significant load – on the order of 1 in-lb (0.113 N-m) for a 1" (25.4 mm) long joint - at cambers of up to 10%. This actuation can be achieved within two seconds, and perhaps significantly faster if the SMA actuates as fast as it can be heated. With the capabilities afforded by this concept, systems can be designed with Active Rigidity Joints implemented in discrete locations along a skeleton, or they can be used in longer sections for a continuous curvature with greater deflection. In either application, no additional actuators are required to develop rotation by this compliant structure, allowing for greater use of available space and total weight of the system. Though not as well suited to high bandwidth control, systems with a finite

number of large scale actuations suited to 0.5-2 Hz operation stand to benefit greatly from the Active Rigidity Joint's passive rigidity and active compliance.

The strain energy model can be used to define a modified force-speed-deflection curve, in the sense that a thicker nichrome layer allows expedited power delivery and hence less time to compliance, but does so at the expense of reduced deflection and holding force in the presence of external loads. Due to inherent transformation lag, it is more important to select a composite structure with large tip deflection and high stiffness over fast response time, assuming that energy requirements will be low due to the joint's beneficial passive properties.

The analytical solution was compared against a finite element model for phase one heating and was consistent to within 2%. The FEM code confirms that the strain distribution solution used by the analytical method is consistent with actual behavior, and allows for visualization of the thermal profile to shape the heating inputs for faster actuation. Through cautious layering configurations, the composite structure can minimize recurve and avoid being back-driven by high external loads. The thermal activation is performed in such a way as to make use of the beneficial modulus variation of both the shape memory polymer and SMA sheets without damage to their structures through overheating, as the temperature profile is closely tailored to the transition points of these materials. In the end, the purpose of the mechanism for each application will determine joint length, layer thicknesses, and presence of additional materials for sensing or insulation. Regardless of these additions, however, the model proposed will be valid as long as the temperature profile described by the tri-phase heating process can be maintained, making it a powerful means of analyzing the spectrum of Active Rigidity Joint configurations for a wide range of applications.

REFERENCES

1. Abdulrahim, M., and Lind, R. 2004. "Flight Testing and Response Characteristics of a Variable Gull-Wing Morphing Aircraft." AIAA 2004-5113. AIAA Guidance, Navigation, and Control Conference and Exhibit, Providence, RI, Aug. 16-19.
2. Abrahamson, E., Lake, M., Munshi, N. and Gall, K. 2002. "Shape memory polymers for elastic memory composites." *AIAA* 2002-1562. AIAA Structures, Structural Dynamics & Materials Conference, Denver, CO, April 22-25.
3. Bejan, A. 1993. Heat Transfer. New York: John Wiley & Sons, Inc.
4. de Blonk, B. and Lagoudas, D. 1998. "Actuation of elastomeric rods with embedded two-way shape memory alloy actuators." *Smart Materials and Structures* 7: 771-783.
5. Boyd, J. and Lagoudas, D. 1996. "A Thermodynamic Constitutive Model for Shape Memory Materials: I. The Monolithic Shape Memory Alloys." *Int. J. Plast.* 12: 805-842.
6. Briggs, J., and Ostrowski, J. 2002. "Experimental Feedforward and Feedback Control of a One-Dimensional SMA Composite." *Smart Materials and Structures,* 11: 9-23.
7. Brinson, L. 1993. "One-Dimensional Constitutive Behavior of Shape Memory Alloys: Thermomechanical Derivation with Non-Constant Material Functions and Redefined Martensite Internal Variable." *Journal of Intelligent Material Systems and Structures* 4: 229-242.
8. Brown, J. and Hodgson, D. 2000. Using Nitinol Alloys. Shape Memory Applications, Inc.

9. Chaudhry, Z. and Rogers, C.A. 1993. "Enhancing Induced Strain Actuator Authority Through Discrete Attachment to Structural Elements." *AIAA* 31 (7): 1287-1292.
10. Cullen, S. 2003. "Thermomechanical Properties of Shape Memory Polymers." SAMPE Conference Proceedings, Long Beach, CA, May.
11. Eggeler, G., Hornbogen, E., Yawny, A., Heckmann, A. and Wagner, M. 2004. "Structural and functional fatigue of NiTi shape memory alloys." *Mat. Sci. Engr. A* 378: 24-33.
12. Everhart, M., Stahl, J., Traxler, E. and Havens, E. 2004. "Shape Memory Polymer Configurative Tooling." Proc. SPIE Volume 5388, 87: 87-94.
13. Ford, D. and White, S. 1996. "Thermomechanical Behavior of 55Ni45Ti NITINOL." *Acta Mater*. 44: 2295-2307.
14. Gaudenzi, P. and Barboni, R. 1999. "Static Adjustment of Beam Deflections by Means of Induced Strain Actuators." *Smart Materials and Structures* 8: 278-283.
15. Gross, K. and Weiland, L. 2007. "Flexural testing of shape memory polymers for morphing aircraft applications." IMECE 2007-43219. Proc. IMECE 2007, Seattle, WA, Nov. 11-15.
16. Huang, W. 1998. "Shape Memory Alloys and their Application to Actuators for Deployable Structures." PhD Thesis. University of Cambridge.
17. Irie, M. 1998. "Shape memory polymers", in Shape Memory Materials, ed. K. Otsuka and C.M. Wayman, Cambridge University Press, pp. 149-183.
18. Kapuria, S. 2001. "An Efficient Coupled Theory for Multilayered Beams with Embedded Piezoelectric Sensory and Active Layers." *Intl. J. Solids Struct.* 38: 9179-9199.
19. Kim, C. 2006. "A Smart Polymer Composite Actuator with Thin SMA Strips." *Intl. J. Modern Phys. B* 20: 3733-3738.

20. Kota, S., Lu, K., Kreiner, Z., Trease, B., Arenas, J. and Geiger, J. 2005. "Design and Application of Compliant Mechanisms for Surgical Tools." *Journal of Biomechanical Engineering,* 127 (6): 981-989. Technical note.
21. Lagoudas, D., Moorthy, D., Qidwaland, M. and Reddy, J. 1997. "Modeling of the thermomechanical response of active laminates with SMA strips using the layerwise finite element method." *Journal of Intelligent Material Systems and Structures* 8: 476-488.
22. Lazarus, K., Crawley, E. and Lin, C. 1996. "Multivariable High-Authority Control of Plate-Like Active Structures." *J. Guidance, Control, and Dynamics* 19 (6): 1357-1363.
23. Liang, C. and Rogers, C. A. 1990. "One-dimensional thermomechanical constitutive relations for shape memory materials." *Journal of Intelligent Material Systems and Structures* 1: 207-234.
24. Lim, C. and Lau, C. 2005. "A New Two-Dimensional Model for Electro-Mechanical Response of Thick Laminated Piezoelectric Actuator." *Intl. J. Solids Struct.* 42: 5589-5611.
25. Liu, Y., Gall, K., Dunn, M. and McCluskey, P. 2003. "Thermomechanical recovery couplings of shape memory polymers in flexure." *Smart Materials and Structures* 12: 947-954.
26. Love, M., Zink, P., Stroud, R., Bye, D. and Chase, C. 2004. "Impact of Actuation Concepts on Morphing Aircraft Structures." *AIAA* 2004-1724. AIAA Structures, Structural Dynamics & Materials Conference, Palm Springs, CA, April 19-22.
27. Mabe, J., Ruggeri, R., Rosenzweig, E. and Yu, C. 2004. "Nitinol Performance Characterization and Rotary Actuator Design." Proc. *SPIE* Volume 5388 95: 95-109.

28. Maji, A., Wegner, P. and Rochin, R. 2004. "Surface Actuation of Lightweight Mirrors with Shape Memory Alloy." *J. Aero. Eng.* 17 (2): 83-89.
29. Manzo, J. 2006. "Analysis and design of a hyper-elliptical cambered span morphing aircraft wing." Masters Thesis. Cornell University, Ithaca, NY.
30. Manzo, J., Garcia, E., Wickenheiser, A. and Horner, G. 2005. "Design of a shape-memory alloy actuated macro-scale morphing aircraft mechanism." SPIE 12th Annual International Symposium on Smart Structures and Materials, San Diego, CA, March 7-10.
31. Miller, D. and Lagoudas, D. 2001. "Influence of cold work and heat treatment on the shape memory effect and plastic strain development of NiTi." *Mat. Sci. Engr. A* 301: 161-175.
32. Moored, K. and Bart-Smith, H. 2005. "The Analysis of Tensegrity Structures for the Design of a Morphing Wing." Proc. SPIE 5764: 253-261.
33. Reed, J., Hemmelgarn, C., Pelley, B. and Havens, E. 2005. "Adaptive wing structures." Proc. SPIE 5762: 132-142.
34. Rogers, C., Liang, C. and Jia, J. 1991. "Structural Modification of Simply-Supported Laminated Plates Using Embedded Shape Memory Alloy Fibers." *J. Comp. and Struct.* 38, (5/6): 569-580.
35. Shames, I. 1975. Introduction to Solid Mechanics. New Jersey: Prentice-Hall, Inc.
36. Sullivan, J., Hubbard, J. and Burke, S. 1996. "Modeling Approach for Two-Dimensional Distributed Transducers of Arbitrary Spatial Distribuion." *J. Acoust. Soc. Am.* 99 (5): 2965-2974.
37. Tanaka, K., Nishimura, F. and Tobushi, H. 1995. "Transformation start lines in TiNi and Fe-based shape memory alloys after incomplete transformations induced by mechanical and/or thermal loads." *Mechanics of Materials* 19 (4): 271-280.

38. Tobushi, H., Hayashi, S., Hoshio, K., Makino, Y. and Miwa, N. 2001. "Thermomechanical constitutive model of shape memory polymer." *Mechanics of Materials* 33 (10): 545-554.
39. Trease, B. and Kota, S. 2006. "Synthesis of Adaptive and Controllable Compliant Systems with Embedded Actuators and Sensors." DETC2006-99266. Proc. IDETC/CIE 2006 ASME 2006 International Design Engineering Technical Conferences & Computers and Information in Engineering Conference, Philadelphia, PA, Sept. 10-13.
40. Trease, B., Moon, Y. and Kota, S. 2005. "Design of Large-Displacement Compliant Joints." Trans. ASME 127: 788-798.
41. Troisfontaine, N., Bidaud, P. and Larnicol, M. 1999. "Optimal design of micro-actuators based on SMA wires." *Smart Materials and Structures* 8: 197-203.
42. Umezaki, E. 2006. "Temperature distributions of SMA wires embedded in epoxy resin plates and heated by supplying electric current." *Journal of Intelligent Material Systems and Structures* 17: 1115-1120.
43. Vehar, C., Kota, S. and Dennis, R. 2004. "Closed-loop tape springs as fully compliant mechanisms – preliminary investigations." DETC2004-57403. Proc. 28th Biennial Mechanisms and Robotics Conference, Salt Lake City, UT, Sept. 28-Oct. 2.
44. Wang, B. and Rogers, C. 1991. "Modeling of Finite-Length Spatially-Distributed Induced Strain Actuators for Laminate Beams and Plates." *Journal of Intelligent Material Systems and Structures* 2: 38-58.
45. Wiggins, L., Stubbs, M., Johnston, C., Robertshaw, H., Reinholtz, C. and Inman, D. 2004. "A Design and Analysis of a Morphing Hyper-Elliptic Cambered Span (HECS) Wing." *AIAA* 2004-1885. 45th AIAA/ASME/ASCE/AHS/ASC

Structures, Structural Dynamics & Materials Conference, Palm Springs, CA, April 19-22.

46. Wilson, T., Small, W., Benett, W., Bearinger, J. and Maitland, B. 2005. "Shape memory polymer therapeutic devices for stroke." Proc. SPIE Optics East, Boston, MA, Oct. 23-26.
47. Zak, A., Cartmell, M., Ostachowicz, W. and Wiercigroch, M. 2003. "One-dimensional shape memory alloy models for use with reinforced composite structures." *Smart Materials and Structures* 12: 338-346.

This chapter originally appeared as:

Manzo, J. and Garcia, E., "Methodology for design of an active rigidity joint", *Journal of Intelligent Material Systems and Structures*, Vol. 20, No. 3, 2009, pp. 311-327.

CHAPTER 4

ANALYSIS AND OPTIMIZATION OF THE ACTIVE RIGIDITY JOINT[1]

1. Introduction

With the aid of active materials such as shape memory alloy and piezoelectrics, composite beams have been used to control motion with applications in vibration control, robotic manipulation, energy harvesting, and deflection sensing (Bailey and Hubbard, 1985; Lee and Moon, 1989, Dimitriadis *et al*., 1991). These structures exhibit similar deformation trends, either actuating electrically or thermally or instead sensing voltage fluctuations when driven (Smits *et al*., 1991). Active beams seldom deform to multiple, passively stable configurations without bulky external mechanical devices (Abdulrahim and Lind, 2004; Wiggins *et al*., 2004) or constant energy input (Strelec *et al*., 2003; Manzo *et al*., 2005).

Designed at the Cornell University Laboratory for Intelligent Machine Systems (LIMS), the active rigidity joint is a passively rigid deformable beam capable of large deflections. Precise layering of shape memory alloy (SMA) and shape memory polymer (SMP) as actuator and variable rigidity element, respectively, allows the thermally activated composite joint to be passively locked into different morphologies without constant energy input (Manzo and Garcia, 2009). This type of actuation has many potential uses, including applications on morphing aircraft (Kudva *et al*., 1999; Lazarus *et al*., 1997; Mabe *et al*., 2004), where large-scale shape change with low power and weight requirements are all significant design motivators.

[1] From Manzo, J. and Garcia, E., "Analysis and optimization of the active rigidity joint"; reprinted by permission of the Institute of Physics, Inc.

Because the joint contains energy dense actuators and yet is rigid enough to carry reasonable loads without being back-driven, the overall system serves two purposes. Above all it is a structural element. Unlike many active hinge joints requiring energy to hold deflection when loaded, the active rigidity joint withstands loading in both active and passive states. In addition, the joint can attain large geometry change with a very small envelope. As such, performance characterization can be viewed from the perspective of conventional actuator design (specific work capacity, energy density, energetic efficiency, etc.) as well as passive beam design (stiffness, block force).

The joint is outlined in an earlier paper (Manzo and Garcia, 2009), wherein a layering configuration is described capable of overcoming an external load, deflecting to a new curved state, and passively holding rigidity in this new state. Deflections presented using this analytical model are valid for the surface-bonded configuration studied but are not optimal – that is, maximum deflection was not achieved in the presence of large external loads with weight or size penalties. Updates to the analytical model improve accuracy given embedded actuators and thermal constraints. Surface bonded actuation is a tempting, simplistic configuration, but it will be shown that such an assembly does not always yield desirable deformations. With the improved model, optimization can assess and improve actuator performance, determining thickness and location of each joint element to maximize various key metrics. While optimal geometry has been studied for piezoelectric beam composites using visual inspection, closed-form Hessian solutions, and gradient searches (Kim and Jones, 1991; Main *et al.*, 1994; Seeley and Chattopadhyay, 1993), the complex actuation in the active rigidity joint requires alternate approaches to find optimal geometries.

2. Formulation of Problem

The active rigidity joint is a symmetric composite of actuators and structural elements in an antagonistic unimorph configuration capable of curving away from the centroidal axis in either direction. Initial configurations consist of externally-located SMA bonded to SMP, with a core of nichrome wire to heat the structure independently of the SMA. This is reflected in Figure 4.1, which shows the initial schematic at left and approximate stress distribution predicted by an Euler-Bernoulli model at right.

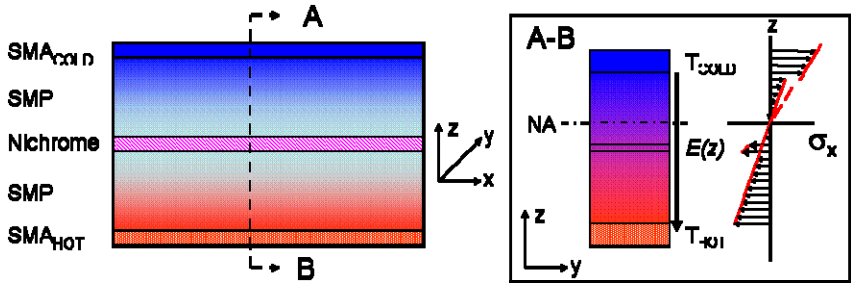

Figure 4.1 - Initial 5-layer active rigidity joint schematic and approximate stress distribution

Nichrome and SMA layers are represented as monolithic structures with thickness representing the extruded area of wire filaments used in a practical system. Through heating, the decreased stiffness of the SMP allows increased compliance for the composite, such that SMA activation yields beam rotation as the lower heated SMA layer transitions from elongated, detwinned martensite to contracted austenite. This is reflected in earlier work by the linear strain distribution of Figure 4.2 or the embedded case of Figure 4.3, with a maximum strain $K\Lambda$ at the contracting actuator and zero strain at the opposite face(s) (Manzo and Garcia, 2009). Perfect adhesion and no slip conditions at the beam edges are assumed.

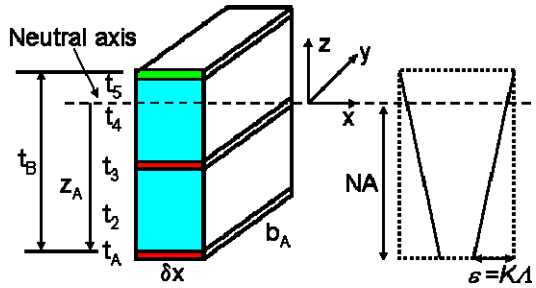

Figure 4.2 - Schematic showing conventions and induced strain distribution

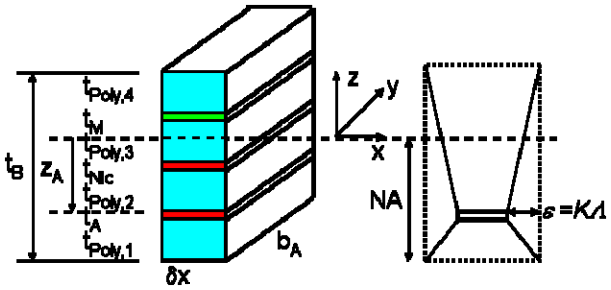

Figure 4.3 - Schematic allowing actuator to be non-surface bonded

The model of Manzo and Garcia (2009) following Wang and Rogers (1991) sums moments about beam neutral axis, labeled 'NA', in determining bending response to an externally applied load. Strain on the actuator and actuator moment applied to the structure are expressed respectively as:

$$\varepsilon_A = \Lambda - \varepsilon = (1-K)\Lambda \tag{1}$$

$$M_A = z_A\, t_A\, b_A\, \sigma_A = z_A\, t_A\, b_A\, E_A\, (1-K)\,\Lambda \tag{2}$$

where ε is the tensile strain, Λ the free actuator contractile strain achieved through ohmic heating, E_A the actuator stiffness, and with all other terms coming from Figure 4.2 or 4.3. The parameter K represents the unknown fraction of free actuator strain contracting in the presence of structural and external moments that resists bending by elongating the SMA. Resistive moment is a found from the induced strain distribution

of the remaining structure shown in Figures 4.2 and 4.3, represented by a linear distribution for the surface bonded case or, for the embedded case:

$$\varepsilon_u(z) = \frac{z + z_A - t_b}{z_A + {}^{t_A}\!/_2 + NA - t_b}$$
$$\varepsilon_d(z) = \frac{z + NA}{z_A - {}^{t_A}\!/_2 + NA} \tag{3}$$

where ε_u represents material above the midline of the strain actuator, and ε_d represents below the actuator midline. Moment on the actuator by the structure is expressed as:

$$M_S = \lambda K b_S \Lambda \tag{4}$$

where λ is a function of a scaled strain term $\phi(z)$ nondimensionalized by free strain fraction $K\Lambda$:

$$\lambda = \int_{-Z_A}^{t_b - Z_A} E(z)\,\phi(z)\,z\,dz$$
$$\phi(z) = \frac{\varepsilon(z)}{K\Lambda} \tag{5}$$

The function $\phi(z)$ has a distribution explicitly specified by either Figure 4.2 or 4.3 based on geometry, ranging from 1 at the actuator to 0 at the non-active outer face(s). Actuator and structural element stiffness is expressed as a function of transverse location, and in numerical simulation is a function of assumed strain values such that lookup tables for complex stress-strain behavior can be used. Rearranging Equations (2) and (4) and incorporating external moment, the unknown parameter K can be found as:

$$K = \frac{z_A\, b_A\, E_A\, t_A \Lambda - M_{EXT}}{\lambda\, b_A \Lambda + z_A\, b_A\, E_A\, t_A \Lambda} \tag{6}$$

Knowing strain at the actuator layer, $K\Lambda$, joint deflection assuming constant radius arc lengths is known explicitly. This formulation shows good agreement with finite element response for surface bonded composites such as that of Figure 4.2. However, as will be shown in Section 2.3, there is disagreement between FEM and analytical results for embedded actuators, requiring further additions to this model.

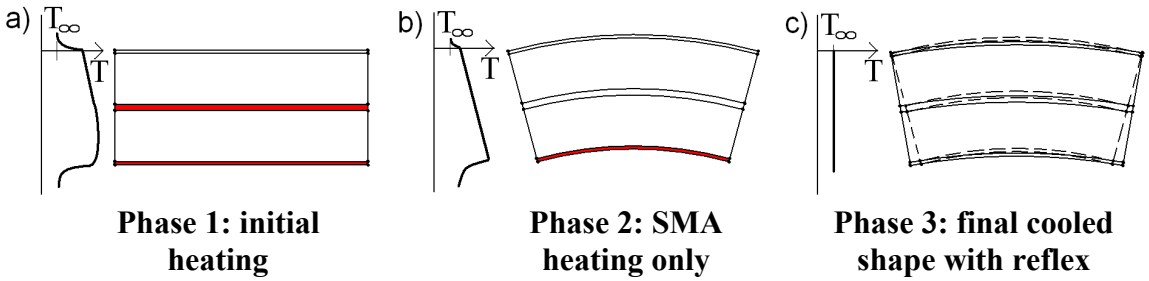

Figure 4.4 - Tri-phase cooling process for active rigidity joint

To achieve a passively rigid cooled joint after actuation, the 'Tri-Phase' process is used. Seen in Figure 4.4, the process starts by heating both nichrome and SMA layers. With the proper thermal gradient reached, the SMP becomes compliant and SMA contraction allows for deformation shown in phase two. De-energizing the nichrome allows the SMP to cool below its glassine point except local to the SMA, which must maintain high temperature to apply contractile force as the SMP cools and stiffens. Once the SMP has cooled sufficiently to carry structural loads, the SMA is de-energized, reaching passive rigidity at ambient temperature with slight reflex in phase three.

2.1. Model Improvements

As mentioned above, the model of Equations (1)-(6) works well for surface bonded configurations and also shows agreement with finite element results for a symmetric piezoelectric bimorph, with neutral axis at beam centerline and with bending symmetric about this axis. However, the active rigidity joint differs from this piezoelectric model by its asymmetric strain distribution during actuation, and also by application of induced strain at only one active layer due to antagonistic unimorph design. These distinctions lead to forces not acting about the neutral axis, leading to a mismatch between finite element and analytical results in many cases and requiring an extension to governing equations proposed by Wang and Rogers (1991) or Manzo and Garcia (2009).

To account for actuation asymmetry, a more thorough model for induced strain behavior is required. Following Huang *et al*. (2004) or Lobontiu and Garcia (2005), three constraint equations describe behavior of a multimorph beam in static equilibrium:

$$\sum M_Y = 0 \tag{7}$$

$$\varepsilon_i(z) = \varepsilon_{i+1}(z) \tag{8}$$

$$\sum P_X = 0 \tag{9}$$

Equations (7)-(9), respectively, state that the sum of moments in the X-Z plane must be zero, that interface strains must be continuous, and that the sum of forces in the X-direction must equal zero. In the initial model of Manzo and Garcia (2009), only the first two of these equations are satisfied. Whereas the symmetric bimorph has forces

automatically in balance, for active rigidity joint asymmetric actuation the assumed strain distribution of Figures 4.2 or 4.3 is incorrect. Nonzero strain at the upper joint face is required, determined by simultaneously solving Equations (7)-(9). A revised strain distribution is shown in Figure 4.5, which relaxes the zero strain constraint at the upper, passive joint face.

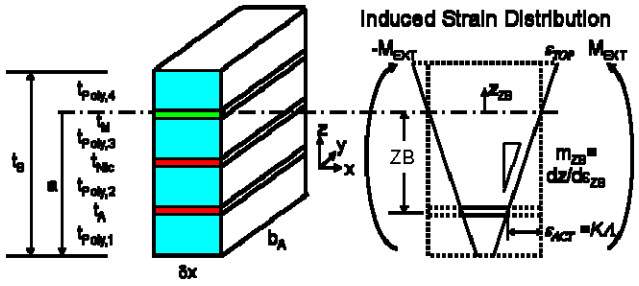

Figure 4.5 - Active rigidity joint with new strain distribution model

Unlike Figures 4.2 or 4.3 or Equation (6), the strain distribution has two unknowns, ε_{ACT} and ε_{TOP}, representing strain at the midline of the active element and at the opposite joint face, respectively. Strain is also now strictly linear through the joint, making more intuitive sense but requiring the additional equation and unknown.

The axis through which zero strain occurs is no longer the stress-adjusted centroidal (neutral) axis but is instead determined by the strain distribution in Figure 4.5. The new zero bending datum line, labeled z_{ZB}, is determined through solution of Equations (7)-(9) once ε_{ACT} and ε_{TOP} are known. This zero bending line is a simplification inherent the Euler-Bernoulli model as opposed to the full elasticity solution, combining compressive and bending loads acting on the beam into a single quantity of interest. It has been referred to as the torque neutral axis by Weinberg (1999), because composite bending action acts about this line. In reality, there is a bending moment about the neutral axis, a compressive force in the longitudinal axis as in Wang and

Rogers (1991), and shear through the thickness due to induced strain. Simplification to the torque neutral axis is in good agreement with both FEA results and existing composite models, as shown below. The datum z_{ZB} can be either inside or outside the joint based on loading.

The solution process is as follows: assuming strains ε_{ACT} and ε_{TOP} through an iterative process outlined in Section 2.2.2, the location of z_{ZB} is found by geometry. Forces and moments on the structure given assumed strain distribution can be found, taken about datum z_{ZB} with strain $\varepsilon(z_{ZB})$. External moments shown in Figure 4.5 are applied as pure couples. Force or moment imbalance informs subsequent iterations for ε_{TOP} and ε_{ACT} until equilibrium is achieved. Force and moment balance equations are:

$$\int_{STRUCT} b(z_{ZB})E(z_{ZB})\varepsilon(z_{ZB})\,dz_{ZB} = \int_{ACT} b(z_{ZB})E_{ACT}(z_{ZB})\varepsilon_{SMA}(z_{ZB})\,dz_{ZB}$$
$$\varepsilon_{SMA} = \varepsilon_{ACT} - \Lambda, \qquad E_{ACT} = E_{ACT}(z_{ZB}, \varepsilon_{SMA}) \tag{10}$$

$$M_{EXT} + \int_{STRUCT} b(z_{ZB})\,E(z_{ZB})\varepsilon(z_{ZB})z_{ZB}\,dz_{ZB} = \int_{ACT} b(z_{ZB})E_{ACT}(z_{ZB})\varepsilon_{SMA}(z_{ZB})z_{ZB}\,dz_{ZB} \tag{11}$$

with actuator stiffness E_{ACT} a strain-dependent quantity seen in Figure 4.6. The subscript '*STRUCT*' refers to passive joint layers and '*ACT*' refers to active layer(s), which in this work refers to the lower SMA and which follows the austenitic SMA stress-strain curve of Figure 4.6. Free actuator strain with zero loading, Λ, must be subtracted from the assumed strain distribution, as shown in Equation (10), to express total strain on the SMA ε_{SMA}, distinct from ε_{ACT} as it represents tensile strain on the active SMA layer rather than compression on neighboring layers.

As seen in Figure 4.6, stiffness of both austenitic and martensitic SMA is nonlinear, requiring a lookup table expressing stress-strain behavior for use in Equations (10) and (11). Austenite and martensite material curves refer to temperatures above phase finish temperatures A_f and M_f, respectively. Stiffness below strain values of 0.36% is assumed constant, and above this a piecewise linear function relating stress and strain is used. Loading hysteresis is indicated with directional arrows. Properties are based on simplified results of studies by Huang (1998), Ford and White (1996), and Zak *et al*. (2003), and neglect cyclic effects and two-way shape memory effect. Equation (10) can be adapted to include more complex models, though this is beyond the scope of analysis. Hysteresis effects are not needed during the heated phase of operation, where SMA stress is constant based on flexural and predetermined external loads. Iterations move along the stress-strain curve only to determine stress and strain distributions satisfying Equations (10)-(11). While a more thorough solution process could include additional time steps accounting for hysteresis during cooling and unloading of the SMA wire, instead we have chosen to model only heated and cooled deformation 'snapshots' represented by Segments 'A' and 'C' in Figure 4.6.

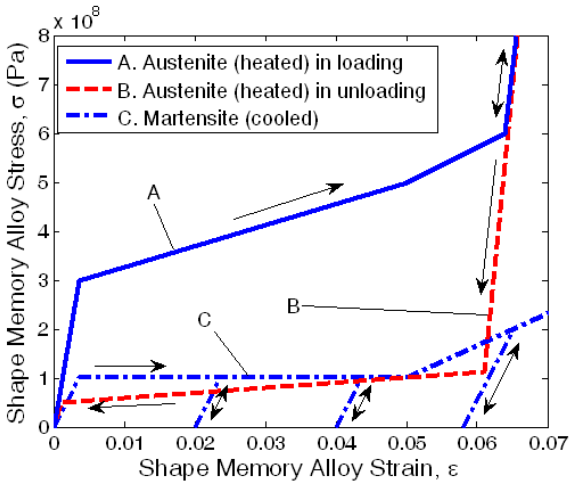

Figure 4.6 – SMA stress-strain behavior used in Equations (10) and (11) showing hysteresis

Another important point is that external moment cannot be added after calculating strain response due to SMA stress-strain nonlinearity. Calculations for ε_{ACT} and ε_{TOP} require all SMA stress contributions to be known a priori. This is also noted by Chaudhry and Rogers (1994), and is a significant change from many piezoelectric beam models considering only load transmission from piezo strain actuator to beam substrate in determining deflection, referred to as "effective moment" by Kim and Jones (1991). These models often disregard external loading effects on actuator behavior (Crawley and de Luis, 1987; Delas *et al*., 2007).

The cooled solution uses a simplified model with initial conditions representing strains after heating as in Figure 4.4a. Strain distribution at the end of phase one (Figure 4.5) is prescribed by ε_{TOP} and ε_{ACT} found by solving Equations (10)-(11) through iteration. New parameters $\varepsilon_{TOP,C}$ and $\varepsilon_{BOT,C}$ describe final strain distribution. The bottom SMA layer now has martensitic (cooled) stiffness behavior, and the SMP has stiffness 60-100 times greater below its glassine temperature T_G than above it (Liu *et al*., 2003, Atli *et al*., 2009). The structure cools and reflexes, relieving nichrome and SMA stress governed by:

$$\begin{aligned} F_{SMP} + F_{SMA,ACT} &= F_{STRUCT} = F_{SMA,COLD} + F_{NIC} \\ F_x &= \int b\left(z_{ZB,C}\right) E_x\left(z_{ZB,C}\right) \varepsilon_x\left(z_{ZB,C}\right) dz_{ZB,C} \end{aligned} \tag{12}$$

$$\begin{aligned} M_{SMP} + M_{SMA,ACT} &= M_{STRUCT} + M_{EXT} = M_{SMA,COLD} + M_{NIC} + M_{EXT} \\ M_x &= \int b\left(z_{ZB,C}\right) E_x\left(z_{ZB,C}\right) \varepsilon_x\left(z_{ZB,C}\right) z_{ZB,C}\, dz_{ZB,C} \end{aligned} \tag{13}$$

$$\begin{aligned}
\varepsilon_{SMP} &= \varepsilon_{COLD}\left(z_{ZB,C}\right) - \varepsilon_{HOT}\left(z_{ZB,C}\right) \\
\varepsilon_{SMA,ACT} &= \varepsilon_{COLD}\left(z_{ZB,C}\right) - \Lambda \\
\varepsilon_{STRUCT} &= \varepsilon_{COLD}\left(z_{ZB,C}\right)
\end{aligned} \tag{14}$$

for the balance of forces, balance of moments, and strain representations, respectively. In Equations (12)-(14), there are now three groups of elements – '*SMP*', '*SMA,ACT*', and '*STRUCT*' – representing the SMP matrix, previously active SMA (now cooled and inactive), and remaining structure. This remaining structure consists of nichrome and opposing (cold) layer of SMA used in antagonistic operation, which both serve as elastic elements resisting deformation at all points in the Tri-Phase actuation cycle. Force and moment definition for an arbitrary layer '*x*' is also listed in Equations (12) and (13), with unique stiffness and strain distributions integrated over their thickness. The reference datum used is a cooled zero bending line, $z_{ZB,C,}$, determined by the assumed strain distribution upon final cooling and found through iteration following Section 2.2.2.

Strain representations of Equation (14) for each element are unique in cooling, because initial conditions for these materials are dependent on loading history. Because SMP creates negligible recovery stress on the order of 0.1 MPa (Atli *et al.*, 2009; Otsuka and Wayman, 1998), its deformations while rubbery (heated) induce no stress or strain on the joint once glassine (cooled). Therefore, SMP strain in the cooled phase is expressed as difference in strain from the end of heating (ε_{HOT}) to the end of cooling (ε_{COLD}). In contrast, the SMA layer activated during heating will continue to resist extension when cooled, but will follow martensite stress-strain behavior rather than austenite. Stress-inducing strain in this SMA layer is the difference between final cooled strain and free strain value Λ. Strain values for

remaining structural materials (nichrome, antagonistic SMA) carry over from the heated phase, so their strain is simply ε_{COLD}.

2.2. Solution Process

To solve for joint deflection, Equations (12) and (13) are used in an inverse process from the conventional approach for multimorph actuators. Because SMA stiffness is load dependent and non-constant, Equations (7)-(9) cannot be expressed as a matrix and inverted to find strain values following Lobontiu and Garcia (2005). The active rigidity joint only allows direct solutions for very low (<0.36%) SMA strains where stiffness is constant. Instead, strains are found through an iterative process, assuming values for ε_{ACT} and ε_{TOP} and modifying them until Equations (9)-(10) are satisfied. First, a closed-form solution following the method of Lobontiu and Garcia motivates this iterative process and validates the above model for a simplified case with small strain values. This process is akin to measuring active rigidity joint deflection in the heated phase only.

2.2.1. Small-Strain Model

Even for small strains, the need for iterative solutions as well as the necessity for the zero bending axis can be shown. Neglecting for a moment the difference between martensite and austenite, a perfectly symmetric joint can be formed from an isentropic core of thickness t_S with SMA layers of thickness t_{ACT} surface bonded to upper and lower faces, and with only one layer active at a time, similar to the piezoelectric antagonistic unimorph of Weinberg (1999). To solve Equations (7)-(9) explicitly for deflection, SMA stiffness is assumed constant. While the stiffness neutral axis lies

along the joint midline due to symmetry, actuation is no longer symmetric about the neutral axis. Instead, only the lowermost element of the three-layer composite is active, while the remaining two layers resist deformation. This changes the force balance on the structure, requiring Equation (9) unlike the symmetrically loaded bimorph. Datum z_{ZB} as in Figure 4.5 is chosen instead of the neutral axis about which to sum moments and forces, such that integrals no longer use absolute coordinates about the midline but reference z_{ZB}, determined by strain distribution. The location of this line is an unknown quantity found by solving for ε_{TOP} and a distinct ε_{BOT}. For small strains this can be determined directly, because stiffness E_{ACT} is constant. The defining equations are:

$$\frac{E_{ACT}}{2m_{ZB}}\left(-4t_{ACT}a-2t_{ACT}^2-2t_S t_{ACT}\right)-E_{ACT}t_{ACT}\Lambda=\frac{E_S}{2m_{ZB}}\left(t_S^2+2t_S t_{ACT}-2t_S a\right) \quad (15)$$

$$\frac{E_{ACT}}{3m_{ZB}}\left[z^3\right]_{-a}^{-a+t_{ACT}}-\frac{E_{ACT}\Lambda}{2}\left[z^2\right]_{-a}^{-a+t_{ACT}}=\frac{E_{ACT}}{3m_{ZB}}\left[z^3\right]_{t_S+t_{ACT}-a}^{t_S+2t_{ACT}-a}+\frac{E_S}{3m_{ZB}}\left[z^3\right]_{-a+t_{ACT}}^{t_S+t_{ACT}-a} \quad (16)$$

$$m_{ZB}=\frac{t_S+2t_{ACT}}{\varepsilon_{TOP}-\varepsilon_{BOT}} \quad (17)$$

where a is the distance from the zero bending line to the bottom face of the joint, which together with slope m_{ZB} for the strain curve (both shown in Figure 4.5) is sufficient to describe strain behavior and find ε_{TOP} and ε_{BOT}. These equations are not fully expanded for brevity, though they indicate the complexity of a solution valid only for the linear regime of SMA where E_{ACT} is constant. To write a closed-form solution for even this simple model is a lengthy process, further complicated by embedded actuation, which is only valid for ε_{SMA}<0.36%, only 7% of the 5% free strain contraction available.

Finite element simulation (ANSYS 11.0) predicts deflection with a difference of less than 4% from this model, and given the constant stiffness assumption for the SMA, the theoretical model of Weinberg (1999) for an identical problem predicts a deflection accurate to within 0.1% of this analysis. More importantly, while the stiffness neutral axis is still at the midline, the axis of zero strain occurs 71% above the bottom face ($a/t_B = 0.71$) as opposed to 50%, a number in close agreement between all three solution methods. This confirms not only the distinction from assumptions of Wang and Rogers (1991) regarding upper face strain, but also the necessity for using torque neutral axis (z_{ZB}) instead of stiffness neutral axis as reference datum.

2.2.2. Iterative Solution Method

As shown above, asymmetric actuation, nonlinear actuator stiffness, and embedded actuator geometries all complicate or render impossible the closed-form solution process of Equations (15)-(16). For the case of the active rigidity joint under adverse loading, all of these conditions are true – actuator stress-strain behavior extends into a nonlinear region, only one layer is active instantaneously, and arbitrary actuator embedding is allowed. An iterative approach overcomes these obstacles similar to Ende *et al*. (2008), another case where stiffness of at least one composite layer is dependent on strain. Rather than solving for the strains of Equation (17) based on the solution to Equations (15) and (16), an initial guess for actuator and upper face strains is made. With reasonable bounds on the two values, the space of potential combinations for ε_{ACT} and ε_{TOP} or $\varepsilon_{BOT,C}$ and $\varepsilon_{TOP,C}$ is searched until the sum of forces and moments are in balance, resulting in the unique solution for strain values.

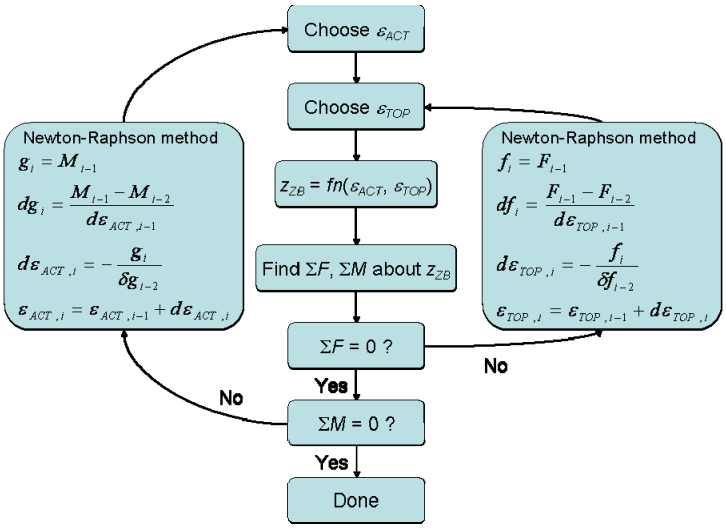

Figure 4.7 - Solution process to determine strain distribution values for active rigidity joint deflection solution

The searching algorithm, run in MATLAB, follows Figure 4.7. With an initial guess for both actuator and upper face strain, the process holds ε_{ACT} fixed and uses a Newton-Raphsson search algorithm in an inner loop to converge on a solution for ε_{TOP}. This balances the forces with a precision of 1×10^{-4} in fewer than 20 iterations. At each iteration, the location of zero bending axis z_{ZB} is prescribed by ε_{ACT} and ε_{TOP}, explicitly providing a solution for the terms a and m_{ZB} in Equations (15)-(17), or more generally allowing for nonlinear actuator stress-strain response to be used directly in Equations (10) and (11). The process is repeated in the outer loop by adjusting ε_{ACT} until balance of moments is also achieved. Uniqueness and convergence are both guaranteed given that force and moment balance equations have only one solution for linear strain distributions where all materials possess stress-strain curves with non-negative piecewise stiffness values (satisfied by Figure 4.6), regardless of material nonlinearity. In many cases, this requires between 80 and 160 total iterations for convergence.

2.3. Comparing FEM to Analysis

Finite element results compares results from the above iterative model to Manzo and Garcia (2009), which follows Wang and Rogers (1991). Simulations use ANSYS 11.0 with a layered elements for fast testing of optimized results. Four cases are tested – surface bonded and embedded strain actuators, with and without external moment applied at one end of the cantilevered beam. Although simplified material models neglecting hysteresis and cyclic effects are used, it will be shown that the new analysis accurately follows FEM simulation.

2.3.1. Simulation Conditions

Material models match analysis for nichrome, SMA and SMP thermo-mechanical properties (Brown and Hodgson, 2000; Cullen, 2003). Shape memory SMA behavior has a temperature-dependent stress-strain relationship, along with a negative coefficient of thermal expansion with 5% contraction at 90 ^{o}C and 2.5% contraction at 75 ^{o}C. Simple piecewise linear models for nonlinear elastic SMA response in the martensite (cold) and austenite (heated) phases are used, with transition models at intermediate temperatures for transient cases. The SMA is modeled with anisotropic properties, contracting only along the longitudinal beam axis to avoid three-dimensional effects. To match analysis, this model neglects SMA pre-strain and plastic deformation, cyclic actuation effects, and material shakedown. The SMP is temperature-dependent, isotropic, and elastic without storage modulus or true viscoelastic behavior, focusing on glassine and rubbery stiffness moduli. Thermal modeling regards only the heated actuation phase, represented by transition from Figure 4.4a - 4.4b.

The model makes use of SHELL91 8-node layered nonlinear shell elements allowing fast (less than 20 iterations) convergence for models of Euler-Bernoulli composite beams. The SHELL91 element can handle multilinear elasticity, large-scale deformations (elastica), and very thin layers, and are the only element type in the ANSYS 11.0 library with all capabilities required for rapid analysis of the active rigidity joint geometry. 160 elements are used with 569 nodes. Models are 1" long, ½" wide, and 1/8" thick, with 0.0015" thickness for each SMA layer and a 0.0006" thick nichrome layer – a thickness adequate to achieve thermal transition established in Manzo and Garcia (2009).

2.3.2. Simulation Results

As seen in Figure 4.8, results between simulation and analysis are in good agreement for the surface bonded case without moment, providing greater accuracy than the method of Wang and Rogers (1991). When surface bonded, a 21 degree tip angle is reached. A linear transverse strain distribution occurs across layers, structural strain at the actuator-SMP interface is 3.1%, and upper face strain is 2.2%. By comparison, the analysis of Wang and Rogers (1991) underpredicts tip angle by 3.4 degrees (16.5% error), with an actuator strain of 2.1% for ε_{ACT} (2.9% for ε_{SMA}), and fixed strain of 0% at the upper face.

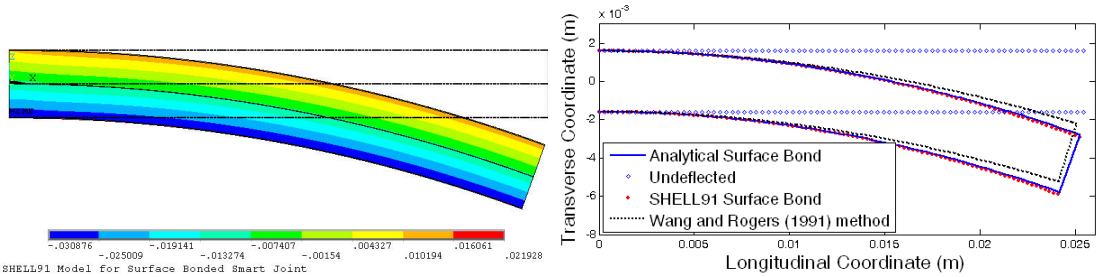

Figure 4.8 – Longitudinal strain (left) and comparison of analytical and FEM response (right) for linear elastic model of active rigidity joint with surface bonded SMA

Embedding the actuator increases deflection provided that SMA stress is below 300 MPa (as in Figure 4.6), with high stiffness at low strain and inducing large rotations due to increased SMA proximity to the torque neutral axis. Seen in Figure 4.9, embedded actuator performance is modeled more accurately with revised analysis compared with Wang and Rogers (1991). Simulation with SMA embedded to a depth of 30% half-thickness yields an upper face strain value of 2.4% with 28 degree tip angle, exceeding 1.3% upper face strain for the surface bonded geometry or 0% for either geometry following Wang and Rogers (1991). Simulation agrees well with the improved analysis, with a tip deflection difference of less than 1 degree (2% error), compared with a difference of 5.5 degrees (19% error) using the original model. In addition, zero longitudinal strain occurs 63.6% from the lower surface of the joint whereas the neutral axis occurs at 40.4% given austenite stiffness compared to martensite. This further justifies using the zero bending (torque neutral) axis in lieu of neutral axis about which to resolve forces and moments.

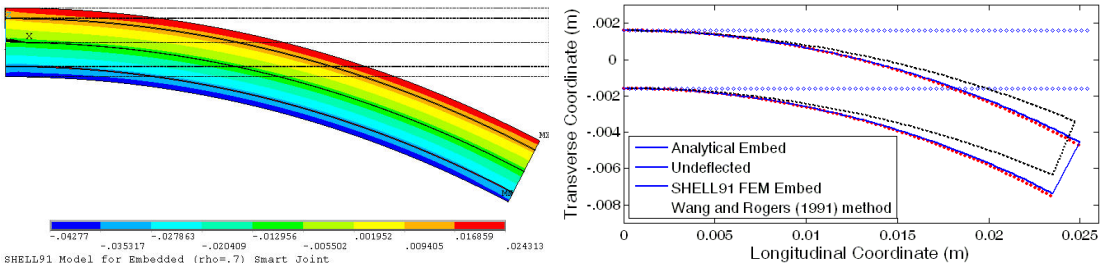

Figure 4.9 –Case with embedded actuator showing that longitudinal deflections agree closely with current analytical model, a significant difference from the previous method

Introducing external loads increases sensitivity to actuator stress and location. Results in Figure 4.10 indicate agreement between FEM and new analysis when applying a resistive tip moment of 0.2 N-m. With embedded SMA actuation, deflection is more sensitive to external moment, decreasing from a 28.3 degree tip angle without M_{EXT} to 10.9 degrees with M_{EXT}. By comparison, the surface bonded joint decreases from 20.6 degrees tip angle without M_{EXT} to 11.5 degrees with M_{EXT}. When embedded, the actuator is closer to the torque-neutral axis, and consequently generates larger deflections but with lower torques, increasing loading sensitivity. Embedding the actuator also reduces effective bending stiffness, with the more compliant SMP at the outer surface. Including external load decreases bending stiffness further, as SMA extension through loading places it in the lower stiffness regime of Figure 4.6. The SMA reaches a peak stress of approximately 450 MPa for the embedded case with M_{EXT} compared with 390 MPa for the embedded actuator without M_{EXT}, and 430 MPa for the surface bonded configuration with M_{EXT} and 380 MPa without. Compared to embedded actuators, surface bonded actuators experience lower stresses and sensitivities in response to load increase, allowing for higher SMA contraction but trading increased block force for decreased deflection.

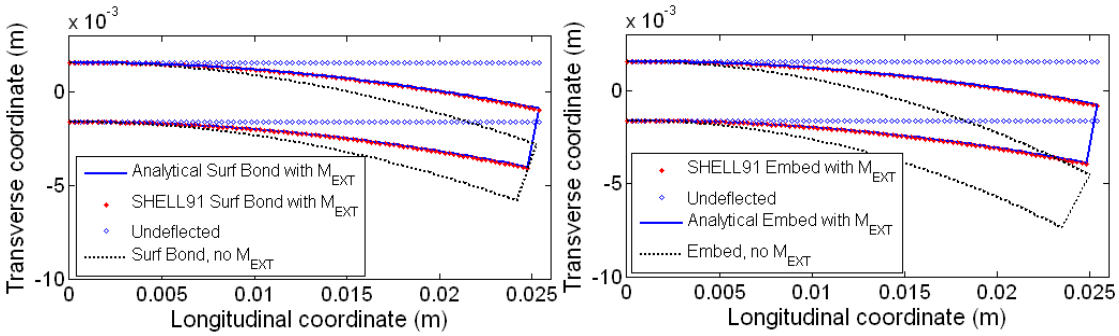

Figure 4.10 - Inclusion of an external tip moment M_Y (here -0.2 N-m) accurately predicted by analytical model for surface bonded (left) and embedded actuator (right). Absence of external moment shown, indicating deflection impact

Results in Table 4.1 show that the new analysis matches finite element results to within 5% for all cases tested. By contrast, the previous method following Wang and Rogers (1991) shows errors of more than 15% in most cases, with embedded configurations demonstrating significant accuracy penalties. Allowing nonzero strain at the upper face and using the torque neutral axis both enhance accuracy of the active rigidity joint analytical solver, although results are not exact at this time. Errors may stem from limitations of the Euler-Bernoulli model in describing strain distribution, from application of external moments as distributed forces, and from the complex thermal strain model used in FEM to simulate SMA contraction.

Table 4.1 - Comparison of finite element and analytical results for various active rigidity joint configurations

SMA location	M_{EXT} (N-m)	Tip defl. (deg), FEM Simulation	Tip defl. (deg), analysis	Difference (%)	Tip defl. (deg), Wang & Rogers (1991)	Difference (%)
Surface	0	20.6	19.8	3.9	17.2	16.5
30% embed	0	28.3	27.7	2.1	22.8	19.4
Surface	0.2	11.5	11.1	3.5	9.9	13.9
30% embed	0.2	10.9	10.4	4.6	9.0	17.4

In reality, joints are constructed using SMA and nichrome wires, rather than slabs of metal. The difference between monolithic slabs and wires has also been examined by

an additional finite element model, which is omitted for brevity. Results confirm that a wire-based FEM model with SMA and nichrome volumes equivalent to those of the slab-based model will demonstrate identical deflection response.

2.4. Analytical Results

The analytical model allows insight into deformations and block forces for specific joint geometries. The configuration presented in Figure 4.8, with surface-bonded actuation, yields a 20 degree tip angle deflection without external loading, or 11 degree tip angle with a 0.2 N-m externally applied tip moment. Deflection can be increased both by increasing the amount of SMA or by embedding the SMA within the structure. The decision is not clear-cut; embedded actuators demonstrate higher deflections but only with reduced loading as explained above, complicating selection of an ideal geometry.

To determine active rigidity joint capabilities, a parametric study can determine performance with regard to different metrics. These metrics are affected by layer thicknesses as well as actuator placement (embedded versus surface-bonded). Variation of each parameter can be studied independently, to assess convexity for simple parameters with regard to a particular cost function and therefore the utility of quadratic programming methods (see for example Reklaitis *et al.*, 1983). Holding the outer dimensions of the joint fixed, response to thickness variations of any one material with respect to any other can be inspected on a three-dimensional plot given a range of external moments M_{EXT} as in Figure 4.5. These two parameters are plotted against a cost value, in this case angular tip deflection θ_C. An alternative metric is

specific energy with a given applied external load, used in subsequent discussion and defined as:

$$J_{SE} = \frac{M_{EXT}\,\theta_C}{m} \qquad \theta_C = \theta_C\left(M_{EXT}\right) \tag{18}$$

where m is joint mass given known layer densities, θ_C is angular deflection after final cooling, and M_{EXT} is external tip moment. Assumed to operate quasi-statically in analysis, an operating frequency may be approximated at ⅓ - ½ Hz given cooling times to determine specific power, though this lacks experimental validation. Angular deflection in response to external moment and geometry changes is shown in Figure 4.11. Three cases are considered – changing the ratio of SMA to SMP, changing the ratio of nichrome to SMP, and varying location of the SMA layers. In the first and last of these cases (Figure 4.11a and 4.11c), changes with a fixed M_{EXT} clearly result in double peaks for tip deflection angle. A logarithmic plot for SMA thickness variations clearly shows non-convexity (Figure 4.11a), with qualitative changes seen in external load variation. Varying SMA location with fixed layer thicknesses (Figure 4.11c) also shows non-convexity. Response to varying nichrome fraction (Figure 4.11b) does not show a double peak in any one axis, but combination of varying M_{EXT} and nichrome thickness results in a complex topology for cost function maximum, shown as a black curve for each value of M_{EXT}. While this function is convex, optimal geometry varies with external loading, which is often non-constant. Overall, non-convexity in multiple dimensions implies that optimal solutions cannot be found using quadratic programming, as only local maxima will be discovered.

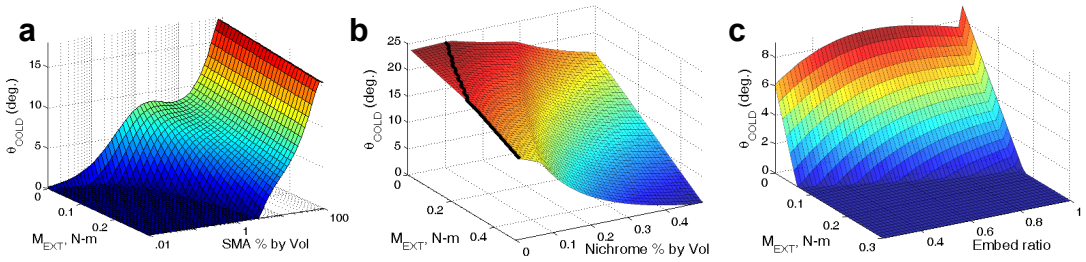

Figure 4.11 – Tip angle response to surface bonded SMA fraction (logarithmic display) with respect to SMP, 3% nichrome by volume (a). Angle response to nichrome thickness with respect to SMP, 4% surface bonded SMA by volume (b). Angle response to SMA embed ratio (1=surface, 0=center), 2.4% nichrome, 1.6% SMA by volume (c). All models assume fixed thickness, ideal thermal considerations. Solid overlaid curves track maxima at each M_{EXT}.

3. Optimization

Optimal actuator location for active composites has been investigated graphically (Kim and Jones, 1991) as above, and with closed-form solutions taking the derivative of deflection response or specific work with respect to individual geometry parameters (Main *et al*., 1994). In addition, non-linear programming such as the conjugate gradient method has been successful on piezoelectric systems (Seeley and Chattopadhyay, 1993). For the active rigidity joint, these methods prove difficult based on non-convexity in multidimensional space, and given the use of two materials in the beam substrate making actuator-to-beam thickness one of multiple optimization parameters. To resolve these issues, heuristic approaches converge on new joint configurations using multiple objective functions by searching non-convex spaces for global maxima. Since the problem deals with continuous variables (thickness of each layer is non-integer valued), optimization is better suited to simulated annealing than to genetic algorithm or tabu search methods. As will be shown, optimization

determines capabilities both for particular geometries and for the entire family of active rigidity joint actuators.

3.1. Simulated Annealing Parameters, Constraints, Metrics

Following Corona *et al*. (1987), simulated annealing tracks maximization of the cost function solution J_{opt}, starting at an initial guess $[X_0, J_0]$. The search space is defined by four variables – SMA thickness (x_1), SMP thickness (x_2), nichrome thickness (x_3), and SMA embed depth (x_4) where zero corresponds to SMA embedded along the midline and unity corresponds to surface-bonded actuators. Initial temperature T_0 requires 30 iterations out of a maximum 8,000 and allows for non-greedy (uphill) moves at the onset of optimization. Each run is repeated at least twice to confirm accuracy of each optimized state variable to within 5%. Implementation in MATLAB is similar to Goffe *et al*. (1994), tailored to parameters of the active rigidity joint with parameter bounds listed in Table 4.2. In fixed overall thickness simulations, only two out of three element thicknesses are varied, while the remaining quantity is prescribed. The initial guess is that of finite element simulation in Section 2.3.

Table 4.2 - Optimization parameters used in simulated annealing

Parameter	Boundaries	Remarks	Initial Guess
x_1: SMA thickness t_1	$1x10^{-4}$"–1/20"	Can be applied in wires or film layer	0.0015"
x_2: Polymer thickness t_2	$1x10^{-4}$"–1/16"	Should comprise bulk by volume	0.0607"
x_3: Nichrome wire 'thickness' t_3	$1x10^{-4}$"–1/32"	Wire area represented by monolithic element	0.0006"
x_4: SMA location from core	0.25 - 1	0 = SMA bonded to nichrome (near centerline), 1 = SMA at outer face	1
Total thickness	0.125"	Thickness fixed to focus on material allocation	.125"
Thermal profile	A_S = 85 ºC	Max 10 amps total (see Section 3.2)	Reached

Cost functions are summarized in Table 4.3. In certain cases one parameter does not yield enough information; for example, specific energy doesn't indicate deflection capability. Specific work and tip deflection angle are chosen as two cost functions. Rather than maximum block force, the third cost function uses a hybrid approach combining tip angle, specific energy, and external moment at maximum specific energy ($M_{EXT,MSE}$, unique from block force). This guarantees both deflection and load-carrying capabilities, since work is only produced when these are both nonzero. Weights are placed on each parameter for hybrid costs to explore new joint workspace regimes.

Table 4.3 - Cost function *J* used in optimization, along with constraints and goals

Cost function	Constraints	Rationale
1. Specific work (M_{EXT} $*\theta$)/m [J/kg]	$0<M_{EXT}<5.0$ N-m, t_B=1/8"	Provides maximum moment and displacement with minimal weight
2. Tip angle θ [deg]	$0<M_{EXT}<5.0$ N-m, t_B=1/8"	Determines boundary for how much joint can deflect with or without external loading
3. $\gamma_1*(\theta/\theta_{MAX})$ + $\gamma_2*(M_{EXT,MSE}/M_{EXT,MAX})$ + γ_3*J/kg	$0<M_{EXT}<5.0$ N-m, t_B=1/8", $\gamma_1+\gamma_2+\gamma_3=1$	Hybrid approach gives better indication of usable workspace than ($M^*\dot{\theta}/m$ or max θ alone

3.2. Thermal considerations

Thermal constraints ensure that feasible heating inputs exist to attain the thermal profile required for deflection. Improper heating can result in reduced actuation potential, excessive structural stiffness, or improper behavior due to unwanted antagonistic actuation. First, threshold temperature for passive martensitic SMA transitioning to austenite ($A_{S,PASSIVE}$) must be avoided, as exceeding this temperature at the passive SMA layer will contract the joint longitudinally rather than bending it.

Second, threshold temperature for actuated SMA to start contracting ($A_{S,ACTIVE}$) must be reached, ideally above austenite finish temperature ($A_{F,ACTIVE}$). Requirements in Table 4.4 are based on SMA with an unloaded A_F of 90 ºC. A maximum of 120 ºC prevents SMA overheating for prolonged lifespan. For the SMP, an exponential temperature-stiffness relationship given by Tobushi *et al.* (2001) predicts that stiffness is at a minimum above 75 ºC, 15 ºC above its quoted glassine transition point, and will demonstrate 90% of this stiffness reduction above 56 ºC. As increased compliance is essential for high deflection in the heated phase, raising SMP temperature as high as possible in the heated phase is critical. A maximum of 150 ºC prevents permanently melting the SMP (Cullen, 2003).

Table 4.4 – Temperature constraints for each element required for successful thermal profile

Layer	Min	Desired	Max
1. Passive SMA	0	<80	80
2. Active SMA	92	>102	120
3. SMP	56	>75	150

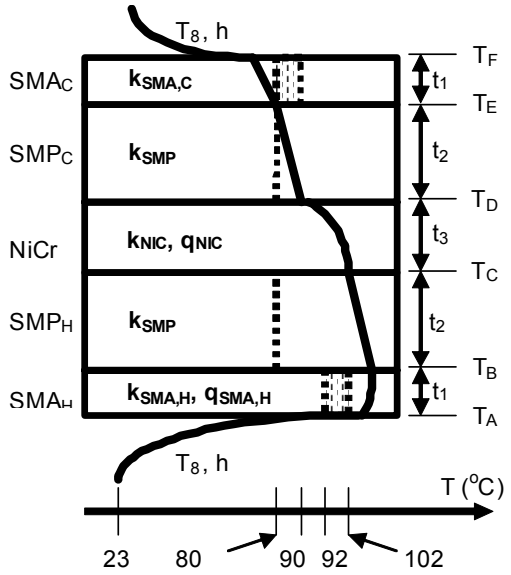

Figure 4.12 - Thermal profile for active rigidity joint showing boundaries used in optimization. Layer thicknesses follow Table 4.2, surface bonded actuator shown.

Thermal constraints are shown visually in Figure 4.12. Temperature modeling follows standard one-dimensional conduction with convective boundaries and ohmic heating (Bejan, 1993; Manzo and Garcia, 2009). Joule heating rates obey constraints of Table 4.4 and attain temperature distributions achieving proper material behaviors. Thermal profile also influences Equations (12)-(14), in that SMP modulus $E_{SMP}(z)$ is prescribed by temperature and maximum free strain Λ for active SMA follows a sinusoidal temperature dependence between $A_{S,ACTIVE}$ and $A_{F,ACTIVE}$ as in Manzo and Garcia (2009). The process allows determination of energetic efficiency given input currents, a feature not optimized in this work.

3.3 Optimization Results

Simulated annealing results show significant improvement over initial geometry guesses. Results show deviation of less than 1% of the final cost between runs, with resolution on each state variable of at least 10^{-4}. Typical convergence results are indicated in Figure 4.13, showing optimization for specific energy. Figure 4.13 tracks both the global optimum found over all iterations as well as the cost function at each optimization step, indicating that non-greedy moves are allowed more during the initial 50-75% of the algorithm and fall off rapidly above this point as dictated by temperature scheduling in optimization. Overlaid in Figure 4.13 are maxima trails for three runs with distinct starting guesses for the state variables. Convergence for these different cases shows solution robustness, as the same solution can be reached with random restarts and through different histories.

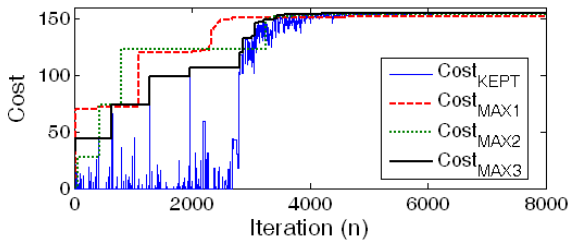

Figure 4.13 - Optimization with respect to specific work after cooled reflex, showing values kept throughout simulated annealing and tracking maximum cost found in three independent runs with unique initial conditions

Optimization results are summarized in Table 4.5, broken down by metrics of Table 4.3 and compared to results for the initial configuration of Section 2.3. Specific energy of over 150 J/kg can be reached in one configuration, a significant improvement over the initial guess at 15 J/kg, and comparable to power output of human muscle of 50 W/kg (McBean and Breazeal, 2004; Madden *et al.*, 2004) if the joint is cycled at ⅓ - ½ Hz. Volumetric analysis also points to effectiveness when compared to biological systems, with 250 kJ/m^3 for the active rigidity joint compared to 8 kJ/m^3 for muscle tissue. Optimizing for deflection achieves a tip angle of 50 degrees, improving by 150% from the initial guess. Both configurations require actuators embedded within the joint, with minimal nichrome thickness (0.08-0.16% by volume) to maximize deformation. The principal difference between geometries of Costs 1-3 is SMA composition, with 0.007" thick layers for maximum specific energy (11% by volume) and only 0.0013" thick layers for maximum angular deflection (2% by volume). Hybrid cost functions of Cost 3a-c provide combined benefits in terms of specific work and deflection, shown in the rightmost two columns of Table 4.5 to provide physical meaning to the mixing function parameters γ_1 - γ_3. Cost 3a, for example, provides over 90% of the specific work and 80% of the deflection as joints optimized solely for these purposes. Looking at both effects at once and assuming

intermediate values between the optimized geometries with the first two costs allows more versatile joint configurations.

Table 4.5 – Converged optimization solutions for various cost functions, listing state variables and cost for particular metrics. Initial guess shown at right.

	Cost function	**X_{OPT}**	**J_{OPT}**	**J| X_{INIT}**	**SE_{MAX} (J/kg)**	**θ_{MAX} (deg)**
1.	Specific energy, $SE = (M_{EXT} * \theta)$/m	[.0069"; .0555"; .0001"; .8621]	152.9 J/kg	14.7 J/kg	152.9	27.8
2.	Tip angle, θ	[.0013"; .0612"; .00016"; .4614]	50.0 deg	19.8 deg	37.1	50.0
3. $J = \gamma_1 * [\theta/\theta_{MAX}] + \gamma_2 * [M_{EXT,MSE}/M_{EXT,MAX}] + \gamma_3 * [SE/SE_{MAX}]$						
3a.	$\gamma_1 = \gamma_2 = \gamma_3 = 1/3$	[.0035"; .0589"; .0001"; .5421]	.6239	.1524	142.4	42.4
3b.	$\gamma_1 = \gamma_2 = ½$, $\gamma_3 = 0$	[.002"; .0604"; .0002"; .4742]	.5150	.1806	54.7	49.5
3c.	$\gamma_1 = ¾$, $\gamma_2 = ¼$, $\gamma_3 = 0$	[.0015"; .0609"; .0002"; .4699]	.7608	.2504	40.7	49.7

As mentioned above, optimization points to minimal nichrome thickness. Nichrome functions as an elastic core, increasing overall structural stiffness. While beneficial in reducing reflex due to M_{EXT}, nichrome also reduces SMA contraction and overall joint deflection upon cooling. Optimization favors heating provided by SMA more than by nichrome, allowing for thinner nichrome layers approaching their lower optimization bounds. Furthermore, in configurations where achieving the desired thermal profile is impossible, optimization favors incomplete SMP thermal transition to the full rubbery state over inclusion of additional nichrome, as deflection results are more sensitive to nichrome fraction than to partial SMP activation. For example, Cost 2 in Table 4.5 results in an SMP temperature of 79 ºC at the heated face of the topmost layer ($t_{POLY,4}$ in Figure 4.5) and 64 ºC at the cooled face, such that stiffness is three times higher at the upper face than in the center. Similar results are found for Cases 3a-3c, which have cold surface temperatures between 64 and 66 ºC instead of their rubbery 75 ºC.

While results of each run yield peak values for distinct physical geometries, a workspace describing force-displacement trade-offs provides more information akin to conventional DC motors and even smart material actuators such as piezoelectrics (Lesieutre *et al.*, 2004) and other induced strain actuators (Chaudhry and Rogers, 1994). Points within the force-displacement bounding curve are reachable, with block force at one end and peak displacement at the other. For the active rigidity joint, these boundaries are replaced by maximum external tip moment and maximum tip angle deflection in radians, such that the product of these quantities is still work done by the system. Unlike force-displacement curves for pure piezoelectric or SMA material, this curve represents capabilities of the entire composite beam. As such, moment-angle curves for the active rigidity joint can be extremely nonlinear, subject to varying material properties and nonlinear SMA response.

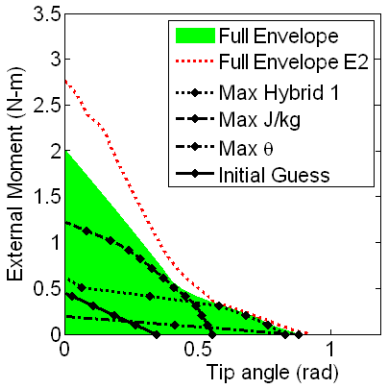

Figure 4.14 – Bounding curves for particular geometries with highlighted optimization runs (curves with markers) and representing 'families' of bounding curves for all tested geometries and for two formulations of SMP(shaded area and dashed curve).

Response curves are shown in Figure 4.14, which presents information in two ways. Curves with markers indicate performance of specific physical geometries. The four curves presented display joint response for initial guess geometry or optimized for particular costs as based on definitions in Tables 4.3 and 4.5. A marked curve

represents capabilities of a particular geometry in terms of moment-angle behavior. For example, a joint optimized for specific energy withstands a tip moment of 1.2 N-m without deflecting, or can reach a tip angle of 0.56 radians (32 degrees) without external loading. Alternatively, the joint optimized for peak angular deflection can handle a maximum of only 0.2 N-m, but can deflect the tip angle by as much as 0.88 radians (50 degrees) in the absence of loading. The second piece of information is the overall bounding region shown shaded, describing the collective family of response curves. This region represents the space of all reachable capabilities for any physical geometry with thermal constraints and those of Table 4.3, indicating reachability for deflection and loading. The model can be adapted to include new materials, shown with an additional dotted bounding region representing a different formulation of SMP more recently commercialized. Newer epoxy-based polymers such as Cornerstone Research Group's Veriflex E2 facilitate deflection when heated (lower rubbery elastic modulus) and possess higher stiffness when cooled (CRG Industries, 2009). The expanded bounding curve using Veriflex E2 yields significant improvements in force-displacement behavior, favoring stiffness and block force with increased specific work capability rather than increased tip deflection, which is more dependent on SMA characteristics.

4. Conclusions

The active rigidity joint is an actuator designed for use on active structures requiring low bandwidth, large-scale actuation with minimal size and complexity. The analytical model presented correlates with finite element results, captures embedded actuation with or without external loading, and incorporates partial thermal transitions. The analytical model of Equations (7)-(14) permits implementation of user-defined

material models to expand on the simplified model presented, providing greater accuracy in simulation results. Thermal constraints show significant impacts on practical geometries, as heating deficiencies with embedded actuators often create undesirable stiffness gradients within the joint. Simulated annealing provides a concise portrait of joint behavior despite the non-convex relationship between geometry and performance, yielding a family of responses with bounded performance given specific materials and assumptions. Tip deflections near 50 degrees for a one inch specimen are possible, while alternate geometries achieve performance similar to mammalian muscle with a smaller footprint, making the actuator well suited to biomimetic applications. With performance presented in a format similar to existing actuator technology, the active rigidity joint can be considered a viable actuator system with unique capabilities tailored to a wide range of structural applications.

REFERENCES

1. ANSYS® Academic Research, Release 11.0, Help System, Structural Analysis Guide, ANSYS, Inc., Canonsburg, PA.
2. Atli, B., Gandhi, F., and Karst, G. 2009. "Thermomechanical Characterization of Shape Memory Polymers". *J. Intell. Mater. Sys. Struct.* (20): 87-95.
3. Bailey, T. and Hubbard, J. 1985. "Distributed Piezoelectric-Polymer Active Vibration Control of a Cantilever Beam," *J. Guidance* 8: 605-611.
4. Bejan, A. 1993. Heat Transfer, John Wiley & Sons, Inc., New York.
5. Brinson, L. 1993. "One-Dimensional Constitutive Behavior of Shape Memory Alloys: Thermomechanical Derivation with Non-Constant Material Functions and Redefined Martensite Internal Variable." *Journal of Intelligent Material Systems and Structures* 4: 229-242.
6. Brown, J. and Hodgson, D. 2000. Using Nitinol Alloys. Shape Memory Applications, Inc.
7. CRG Industries. 2009. "Veriflex E2". [Online] <http://www.crg-industries.com/veriflexE2.htm> 11 Feb 2009.
8. Chaudhry, Z. and Rogers, C. 1994. "Performance and Optimization of Induced Strain Actuated Structures Under External Loading". *AIAA* 32: 1289-1294.
9. Corona, A. Marchesi, M., Martini, C., and Ridella, S. 1987. "Minimizing multimodal functions of continuous variables with the 'simulated annealing algorithm,'" *ACM Transactions on Mathematical Software* 13: 262-280.
10. Crawley, E. and de Luis, J. 1987. "Use of Piezoelectric Actuators as Elements of Intelligent Structures," *AIAA* 25: 1373-1385.
11. Cullen, S. 2003. "Thermomechanical Properties of Shape Memory Polymers." SAMPE Conference Proceedings, Long Beach, CA, May.

12. Delas, O., Berry, A., Masson, P., and Pasco, Y. 2007. "Optimizing the Thickness of Piezoceraminc Actuators for Bending Vibration of Planar Structures," *J. Int. Mater. Sys. Struct.* 18: 1191-1201.
13. Dimitriadis, E., Fuller, C., and Rogers, C. 1991. "Piezoelectric Actuators for Distributed Vibration Excitation of Thin Plates," *J. Vib. Acoust.* 113: 100-107.
14. Ende, D., Bos, B., and Groen, W. 2008. "Non-linear electromechanical behaviour of piezoelectric bimorph actuators: Influence on performance and lifetime". *J. Electroceram* DOI 10.1007/s10832-008-9459-5.
15. Ford, D. and White, S. 1996. "Thermomechanical Behavior of 55Ni45Ti NITINOL", *Acta mater.* 44: 2295-2307.
16. Goffe, W.L., Ferrier, G.D., and Rogers, J. 1994. "Global optimization of statistical functions with simulated annealing," *Journal of Econometrics* 60: 65-99.
17. Huang, C., Lin, Y., and Tang, T. 2004. "Study on the tip-deflection of a piezoelectric bimorph cantilever in the static state". *J. Micromech. Microeng.* 14: 530-534.
18. Huang, W. 1998. "Shape Memory Alloys and their Application to Actuators for Deployable Structures." PhD Thesis. University of Cambridge.
19. Kim, S. and Jones, D. 1991. "Optimal Design of Piezoactuators for Active Noise and Vibration Control," *AIAA* 29: 2047-2053.
20. Kudva, J., Martin, C., Scherer, L., Jardine, A., McGowan, A., Lake, R., Sendeckyj, G., and Sanders, B. 1999. ''Overview of the DARPA/AFRL/NASA Smart Wing Program,'' SPIE Conference on Industrial and Commercial Applications of Smart Structures Technologies, Vol. 3674.
21. Lazarus, K., Crawley, E., and Lin, C. 1997. "Multivariable Active Lifting Surface Control Using Strain Actuation: Analytical and Experimental Results." *J. Aircraft* 34: 313-321.

22. Lee, C. and Moon, F. 1989. "Laminated Piezopolymer Plates for Torsion and Bending Sensors and Actuators." *J. Acoust. Soc. Am.* 85: 2432-2439.
23. Lesieutre, G., Loverich, J., Koopmann, G., and Mockensturm, E. 2004. "Increasing the Mechanical Work Output of an Active Material Using a Nonlinear Motion Transmission Mechanism". *J. Intell. Mater. Sys. Struct.* 15: 49-58.
24. Liang, C. and Rogers, C. A. 1990. "One-dimensional thermomechanical constitutive relations for shape memory materials." *Journal of Intelligent Material Systems and Structures* 1: 207-234.
25. Lobontiu, N., Garcia, E. 2005. Mechanics of Microelectromechanical Systems. Kluwer Academic Publishers.
26. Mabe, J., Ruggeri, R., Rosenzweig, E. and Yu, C. 2004. "Nitinol Performance Characterization and Rotary Actuator Design." Proc. *SPIE* Volume 5388 95: 95-109.
27. Madden, J., Vandesteeg, N., Anquetil, P., Madden, P., Takshi, A., Pytel, R., Lafontaine, S., Wieringa, P., and Hunter, I. 2004. "Artificial Muscle Technology: Physical Principles and Naval Prospects". *J. Oceanic Engr.* 29: 706-728.
28. Main, J., Garcia, E., and Howard, D. 1994. "Optimal Placement and Sizing of Paired Piezoactuators in Beams and Plates." *Smart Mater. Struct.* 3: 373-381.
29. Manzo, J. and Garcia, E. 2009. "Methodology for Design of an Active Rigidity Joint". *J. Int. Mater. Sys. Struct.* 20: 311- 327.
30. Manzo, J., Garcia, E., Wickenheiser, A., and Horner, G. 2005. "Design of a shape-memory alloy actuated macro-scale morphing aircraft mechanism", Smart Structures and Materials 2005: Smart Structures and Integrated Systems, March 6-10, San Diego, CA. published in: *Proc. SPIE* Vol. 5764, pp. 232-240.

31. McBean, J. and Breazeal, C. 2004. “Voice Coil Actuators for Human-Robot Interaction”. Proceedings IEEE/RSJ International Conference on Intelligent Robots and Systems, Sendal, Japan, September 28 – October 2.
32. Otsuka, K. and Wayman, C. 1998. Shape Memory Materials. Cambridge University Press, Cambridge, pg. 203-210.
33. Reklaitis, G., Ravindran, A., and Ragsdell, K. 1983. Engineering Optimization: Methods and Applications. Wiley-Interscience.
34. Smits, J., Dalke, S., and Cooney, T. 1991. “The Constituent Equations of Piezoelectric Bimorphs.” *Sensors and Actuators A* 28: 41-61.
35. Seeley, C. and Chattopadhyay, A. 1993. “The Development of an Optimization Procedure for the Design of Intelligent Structures,” *Smart Materials and Structures* 2: 135-146.
36. Strelec, J., Lagoudas, D., Khan, M., and Yen, J. 2003. “Design and Implementation of a Shape Memory Alloy Actuated Reconfigurable Airfoil.” *J. Intell. Mater. Sys. Struct.* 14: 257-273.
37. Tanaka, K., Nishimura, F. and Tobushi, H. 1995. “Transformation start lines in TiNi and Fe-based shape memory alloys after incomplete transformations induced by mechanical and/or thermal loads.” *Mechanics of Materials* 19: 271-280.
38. Troisfontaine, N., Bidaud, P. and Larnicol, M. 1999. “Optimal design of micro-actuators based on SMA wires.” *Smart Materials and Structures* 8: 197-203.
39. Wang, B. and Rogers, C. 1991. “Modeling of Finite-Length Spatially-Distributed Induced Strain Actuators for Laminate Beams and Plates.” *Journal of Intelligent Material Systems and Structures* 2: 38-58.
40. Weinberg, M. 1999. “Working Equations for Piezoelectric Actuators and Sensors”. *J. MEMS* 8: 529-533.

41. Wiggins, L., Stubbs, M., Johnston, C., Robertshaw, H., Reinholtz, C. and Inman, D. 2004. “A Design and Analysis of a Morphing Hyper-Elliptic Cambered Span (HECS) Wing,” AIAA 2004-1885, 45th AIAA Structures, Structural Dynamics and Materials Conference, April 19-22, Palm Springs, CA.
42. Zak, A., Cartmell, M., Ostachowicz, W. and Wiercigroch, M. 2003. “One-dimensional shape memory alloy models for use with reinforced composite structures.” *Smart Materials and Structures* 12: 338-346.

This chapter originally appeared as:

Manzo, J. and Garcia, E., “Analysis and optimization of the active rigidity joint”, *Smart Materials and Structures*, Vol. 18, No. 12, 2010.

CHAPTER 5

FABRICATION OF AN ACTIVE RIGIDITY JOINT[1]

1. Introduction

In applying induced strain actuation to active structures, one shortcoming is the ability to achieve user-defined rigid shapes without continuous energy expenditure (Crawley and de Luis, 1987; Abe *et al*., 1982). This shortcoming is apparent in the design of morphing aircraft, where torque tubes and rotational SMA hinges must remain energized in their deformed state (Mabe *et al*., 2004; Strelec *et al.*, 2003; Manzo, 2006). The active rigidity joint is a passively rigid actuator formed by a composite of shape memory alloy (SMA) and shape memory polymer (SMP), along with nichrome wire for additional heating (Manzo and Garcia, 2009a). Defined in this work and refined through optimization and improved modeling in an additional paper (Manzo and Garcia, 2009b), the joint uses the polymer as a variable stiffness element to allow for high compliance and facilitate SMA contraction when heated, and to hold the contracted shape without the input of energy when cooled.

The joint demonstrates significant bending capabilities, deforming from a prismatic element to a curved state with a tip deflection of 50 degrees over a one inch length without external loading (Manzo and Garcia, 2009b). The same joint can overcome a 2 N-m external tip moment with a different geometry comprised of the same materials, and in a third geometry can display specific work capabilities of 150 J/kg, with specific power comparable to human muscle when actuated at 0.3-0.5 Hz. Finite element results are in good agreement with the analysis, using monolithic slabs to

[1] From Manzo, J., Geeng, F., and Garcia, E., draft manuscript to be submitted to *Smart Materials and Structures*

represent the nichrome and SMA filaments to be used for heating and/or strain actuation.

Working closely with shape memory polymer manufacturer Cornerstone Research Group, Inc., a process for fabricating the active rigidity joint has been developed. Coupons have been successfully tested and are in agreement with analytical predictions, though with slight adaptations reflecting available materials. Finite element analysis of the changes show good agreement for the modified construction, lending credibility to the analysis presented in the earlier works.

2. Analysis

2.1. Model

The Active Rigidity Joint is composed of three materials: Cornerstone Research Group's Veriflex™ shape memory polymer as variable rigidity substrate, Dynalloy's Flexinol™ shape memory alloy for induced strain actuation, and nichrome wire as an additional heating element. It is fabricated through a molding process of wires and a resin matrix, allowing proper thermal gradients and bending action. Figure 5.1 shows a simplified version of joint cross-section and strain distribution, where wire elements are represented and modeled by monolithic slabs. In this model, the strain distribution and resultant bending is resolved by satisfying strain continuity between layers and balancing the forces and moments between elements. Force and moment balance equations are generated by integrating layerwise contributions over the joint thickness with respect to a reference datum:

$$F_i = \int_i b\,\sigma(z_{ZB})\,dz_{ZB} \tag{4}$$

$$M_i = \int_i b\,\sigma(z_{ZB})\,z_{ZB}\,dz_{ZB} \tag{5}$$

where b is the joint width and σ is the stress on a given material based on stiffness and strain. In the case of shape memory polymer, σ is temperature dependent, motivating the use of a curve fit to the stiffness-temperature characteristics of the material. The z-coordinate is taken with respect to torque neutral axis z_{ZB}, determined by checking the sum of forces and moments with different strain distributions until both are balanced. This iterative process uses Newton-Raphson convergence, and is outlined further in Manzo and Garcia (2009b).

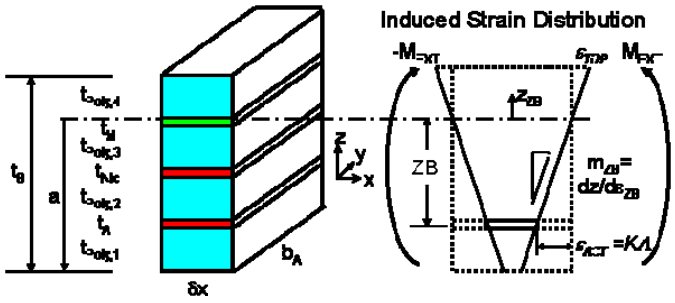

Figure 5.1 – Active rigidity joint cross section using monolithic slab representation, and corresponding strain distribution

The joint follows a three step heating and cooling process to transition between passive states, as shown in Figure 5.2. First, nichrome and SMA are both energized to achieve SMP compliance, and as ohmic heating contracts the SMA, the joint bends in response. Next, the joint is allowed to cool in a prescribed fashion by de-energizing the nichrome, allowing the polymer to cool below its glassine point except local to the heated SMA layer. Finally, the SMA is de-energized, setting the final shape at ambient temperature with a slight reflex due to residual stresses in the nichrome and antagonistic SMA layer as well as any external loading.

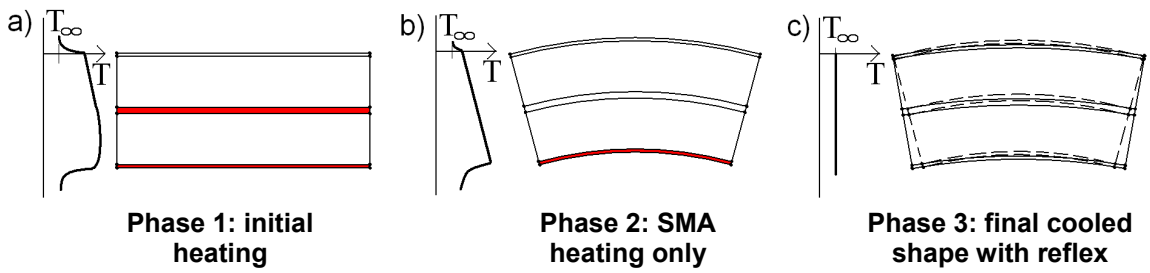

Figure 5.2 – Three phase heating/cooling process for active rigidity joint

2.2. Predicted Behavior

In order to model the behavior of the joint, the geometry and physical characteristics must be known. A summary of material properties is given in Table 5.1, quoted from the manufacturer or readily available online (Brown and Hodgson, 2000). Joints are modeled and fabricated as rectangular prismatic elements with outer dimensions 1" in length by ½" in width by 1/8" in thickness transverse to SMA actuation. The SMA is employed in the form of 2 antagonistic layers of 0.015" diameter SMA wire with eight wires in parallel for each layer. The wire layers are embedded to 50% of the actuator half-depth, or 1/32" beneath the surface of either face.

Table 5.1 – Materials description

Material	**Notes**	**Transition Temp (deg. C)**	**Stiffness (MPa)**	
			Hot	**Cold**
Veriflex SMP	Styrene formulation	75	0.24	600*
Flexinol SMA	0.015" diam. NiTi wire	80-90 (start - full)	83,000	25,000
Nichrome	28 AWG	N/A	220,000	220,000
*See Section 4.2 for detail on SMP stiffness variation				

The model presented in Manzo and Garcia (2009b) can be used to describe performance expected for this geometry joint, which consists of 4.5% SMA by volume and 1.1% nichrome by volume, and has an actuator embedded depth of 50%. Using optimization results from this earlier work as a baseline, analytical results are plotted

on the moment-tip angle plot of Figure 5.3. Results show that the unloaded joint should achieve a tip deflection of 26.6 degrees, with a block moment of 0.28 N-m (2.5 in-lbf). With a peak specific work of only 21 J/kg compared to a possible 150 J/kg for a more optimal geometry, this layering configuration may be impractical for use in active structures. However, given significant deflection capability and a layering configuration that is easy to fabricate with available materials, this configuration was chosen as the baseline for initial fabrication.

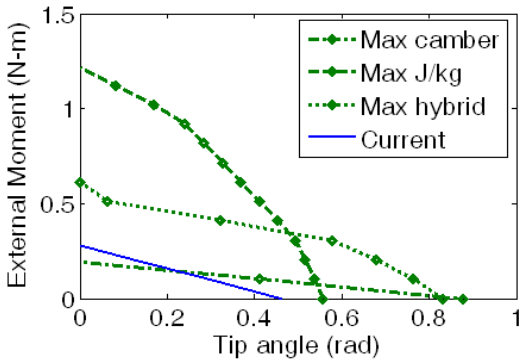

Figure 5.3 – Model characteristics from analysis along with optimized results for different geometries, following Manzo and Garcia (2009b)

3. Experiment

3.1. Specimen Fabrication

To create specimens, a closed-mold potting process is used, injecting the uncured resin around pre-placed SMA and nichrome elements and then curing according to manufacturer specifications. This process and hardware is outlined in the Appendix, and a schematic of the wiring placement in the joint is shown in Figure 5.4. Once molded, power connections to exposed SMA and nichrome wiring are attached using crimped wire ferrules, which allow for wiring the elements of each layer in series to maximize resistance. Two current sources are used to energize the SMA and

nichrome elements, with outputs found through thermal analysis to achieve the proper temperatures of 75, 105, and 80 deg. C for the SMP, active SMA, and passive SMA layers, respectively. Activation currents are dependent upon convection parameters given ambient air conditions, but range between 0.5 and 1.5 A for each layer, with total input power between 2 and 2.5 W.

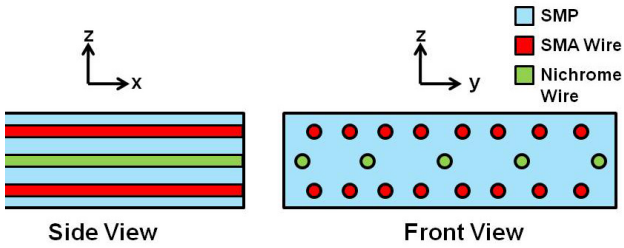

Figure 5.4 – Active rigidity joint cross section schematic showing actual wire placement within joint. In earlier models, nichrome is replaced with aluminum shims and heating is augmented by external sources

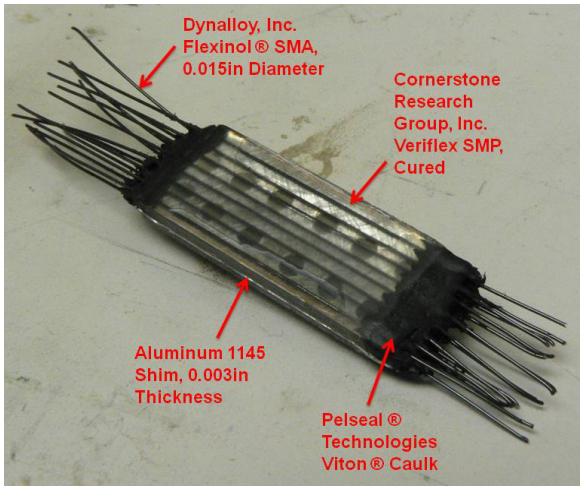

Figure 5.5 – Finished bimorph specimen with aluminum shim (wire ferrules and electrical connections not shown)

3.2. Experimental Methods

Two rounds of testing were performed in testing the joint. In the first, thermal boundaries are prescribed with idealized convection medium of free air or water to

validate the analytical model, with additional heating elements used to artificially induce the proper thermal gradient throughout the joint. Specimens in this first series of tests are only cycled one to three times before failure. In the second, the joint is placed in a wind tunnel under operationally realistic conditions, and life-cycle behavior is tested.

3.2.1. Methods for Validation Testing

To compare against the analytical model, the first round of test specimens were placed in a benchtop setup with a tailored thermal profile. The specimens were clamped in place at their upper 1/8", and electrical wiring was run to both antagonistic sides of the SMA wires. Seen in Figure 5.6, the specimens were placed in front of a grid of known geometry, and were carefully heated until the upper and lower (in the photo, the left and right) faces were at the desired temperature according to 1-D thermal models following Manzo and Garcia (2009a). Once heated, the curved geometry was determined using photogrammetry, determining the approximate bend radius and transverse tip deflection. These are both shown in the marked up image. In this phase, temperature logging was performed manually with an infrared thermometer, and voltage history was only stored for steady-state inputs.

To test both the heated and cooled deflections under ideal cases, the temperature of the entire joint was raised to above the SMP transition point before activating the SMA, maximizing the amount of heated deflection by ensuring that the resin is fully compliant and therefore has the lowest possible flexural modulus. To test the cooled deflection, the joint was cooled as quickly as possible in order to stiffen the SMP, in

some cases experimenting with a cold water bath as the SMA was de-energized in order to ensure the least amount of reflex as depicted in Figure 5.2(c).

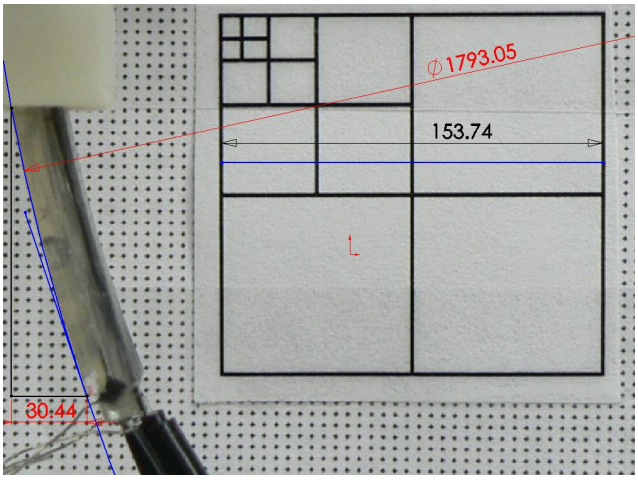

Figure 5.6 – Extracting deflection behavior via image processing

3.2.2. Methods for Life Cycle Testing

To test for long-term behavior, specimens were instrumented with thermocouples for temperature measurement and placed in a forced air environment. In this series of tests, a unimorph joint is tested instead of the full bimorph configuration, where one fully contracted SMA layer is placed close to the center of the joint to be used strictly for heating, rather than for inducing deflection. As seen in Figure 5.7, tests are performed open-loop; the power supply does not receive information from the thermocouples in this set of experiments, though related tests not discussed in this paper were conducted using a microcontroller that incorporated joint temperatures.

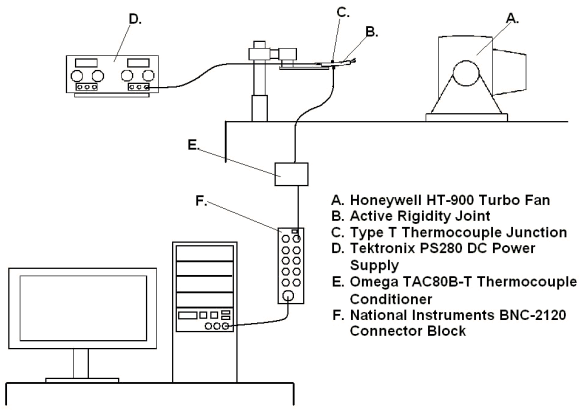

Figure 5.7 – Experimental schematic for life cycle testing

3.3. Experimental Results

3.3.1. Validation Test Results

The results of initial deflection experiments are summarized in Table 5.2. The three different samples tested were fabricated in the same mold, but had two variables affecting their differences. First, each sample had a different shim configuration used at the core of the joint – a 5 mil thick aluminum shim with 1/8" holes, a 3 mil aluminum shim with holes, and a 3 mil aluminum shim with long grooves. As the three-dimensional nature of the true system has complex, second-order effects on joint response, it was difficult to model the system response to stiffening materials of different geometries. Instead, geometries were tested experimentally, following an abbreviated FEA study not presented in this paper. These different shims were employed to tune the stiffness of the system for increased longitudinal stiffness but with minimal impact on bending stiffness. The second difference between tested specimens was that fabrication yielded specimens with variation in layer placement, as materials shifted during the molding process. As a consequence, the shim materials that were meant to sit at $0.50(t_B)$ – the midline of the joint – were shifted by as much

as 12% from their intended location. The same was true of the SMA location throughout the thickness; the desired actuator embedded depth was 50%, but variations led to a range from 55% to 72% away from the midline of the joint. A third variation not related to fabrication was the length exposed from the joint clamp, labeled *L* in Table 5.2. This length varied when specimens were removed and re-installed in the test apparatus. The model was adjusted accordingly to match experimental conditions. Assumptions and simplications used in this set of experiments are as follows:

1. The deflection is only tested after heating, not after the full tri-phase heating and cooling
2. Specimens omit nichrome wire and substitute an aluminum shim as a similarly stiff element at the midline that does not offer an additional heat source
3. Heating is achieved through a combination of the intended SMA heating and external heat sources, as the nichrome is removed from this preliminary model

The results show that deflection most closely agrees with analysis for the specimens with thinner shim materials. While aluminum shims did serve to reduce the compression and shearing modes that were seen in preliminary tests (not shown), their effects on bending stiffness showed significant mismatch with the simplified model except for the thinnest 0.003" shims that could be reliably fabricated for use in the joints. In these cases, the angular deflection after heating matched the analytical model with an error between 4 and 15% for the shim with holes, and between 7 and 10% for the shim with long grooves. The transverse tip deflection was more accurate for the grooved shim, with an error of between 1.6 and 5%, compared with an error between 33 and 66% for the shim with holes. While results offer mixed consistency,

angular tip deflection in all specimens exceeded 10 degrees in a joint less than an inch long.

Table 5.2 – Tip angle, vertical tip deflection, and bend radius experimental results of testing unimorph joints under idealized thermal conditions. Results show closer agreement when thinner shim is used.

Model Verification		**Experiment**			**Analysis**		
Sample	**L**	θ_{HOT} **(deg)**	d_{HOT}	r_{HOT}	θ_{HOT} **(deg)**	d_{HOT}	r_{HOT}
A. ρ = .608, shim at .52(t_B), .005" shim with holes	.775" .785" .833"	11.23 10.18 12.12	.100" .059" .127"	5.83" 7.07" 7.07"	23.86 24.17 25.65	.159" .163" .183"	1.80" 1.80" 1.80"
B. ρ = .722, shim at .62(t_B), .003" shim with holes	.78" .78" .78" .78"	17.06 15.7 18.62 16.14	.161" .170" .182" .147"	4.21" N/A 4.38" 4.42"	16.3 16.3 16.3 16.3	.110" .110" .110" .110"	2.65" 2.65" 2.65" 2.65"
C. ρ = .553, shim at .47(t_B), .003" shim with grooves	.845" .845" .792"	31.14 32.40 20.45*	.237" .246" .136"	1.67" 1.61" 1.83"	34.9 34.9 32.7	.250" .250" .221"	1.33" 1.33" 1.33"
*Shim buckled on final test							

A subset of data is available for the deflection after cooling, which yielded limited success. Cooling in free air did not provide adequate convection for the faces of the joint, and as a consequence, the cooled thermal profile was not achieved to allow for the deflection to be held once the SMA was de-energized. However, immersing the specimens in a cold water bath for sample 'C' allowed for some deflection to be retained, seen in Table 5.3.

Deflection yielded only 8 degrees out of a heated 20-30 degrees at the tip, which is well below the analytical model prediction of over 20 degrees deflection post-cooling. This points to two facts; first, the method of determining core temperature via infrared detection does not provide adequate information about the thermal profile. This is an

issue that was addressed through the use of embedded thermocouples in the following section. Second, the simplified, one-dimensional thermal model used in predicting the behavior of the joint may be insufficient or inappropriate, given the three-dimensional heat flow out of all joint faces and using wires instead of monolithic slabs.

Table 5.3 – Experimental deflection of specimens pre- and post-cooling

	θ_{HOT} (deg)	θ_{COLD} (deg)
A. ρ = .608, shim at .52(t_B), .005" shim with holes	11.23 10.18 12.12	~0 ~0 ~0
B. ρ = .722, shim at .62(t_B), .003" shim with holes	17.06 15.7 18.62 16.14	<0 ~0 <1 ~0
C. ρ = .553, shim at .47(t_B), .003" grooved shim	31.14 32.4 20.45	7.94 ~0 7.86

3.3.2. Life Cycle Test Results

For the next phase of tests, life cycle experimentation on a number of joint samples followed the tri-phase heating technique of Figure 5.2. A modified version of this process, representative of that used in this phase of testing, is seen in Figure 5.8. Here, SMA and the core ohmic heating layer raise the temperature to compliance, then the ohmic heating is reduced to allow the SMP to cool, and finally all power is cut to the system to allow the joint to cool fully. This process can be adjusted manually, or closed-loop using a microcontroller. In this case, the system was adjusted manually, such that there is overshoot in reaching the loaded austenite temperature of 90 C for the actuating SMA layer.

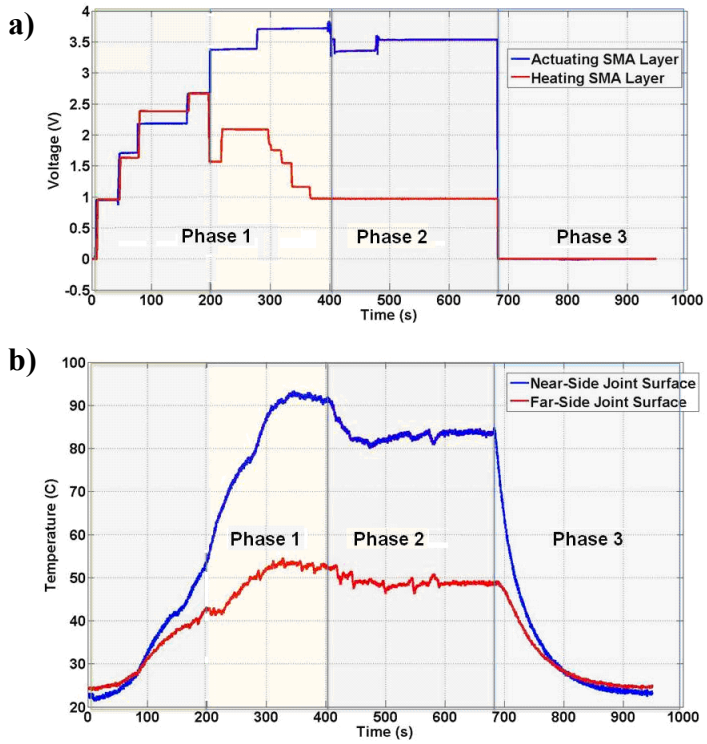

Figure 5.8 – Voltage (a) and temperature (b) time history for tri-phase heating of active rigidity joint on benchtop

Available results of cyclic testing are shown in Table 5.4. Of the 14 specimens created, 5 were suitable for actuation (complete mold, wires embedded) and were successfully actuated in the proper orientation (bending without torsion or buckling). The number of tests varied based on when the joint failed, in some cases yielding a single successful actuation and in others exceeding 20 cycles before failure. Though a full characterization of response history as a function of cycle could not be performed, it is generally the case that as the number of cycles increases, the available deflection decreases significantly, both in the heated and cooled phases.

Table 5.4 – Available results of life cycle testing for various joint specimens

Sample	Test #	θ_{HOT} (deg)	θ_{COLD} (deg)
1. B3-UNI-S1-T0-10-10-09-01	1	24.16	3.43
2. B2-UNI-SAL2-T0	1	15.14	10.00
3. B3-UNI-SAL-11-12-09	1	16.84	8.44
3. B3-UNI-SAL-11-12-09	2	**	8.63
4. B4-UNI-SMAH-11-30-09	16	2.35	0.32
4. B4-UNI-SMAH-11-30-09	17	1.06	0.66
4. B5-UNI-SMAH-02-08-10	1	18.02	4.13
5. B5-UNI-SMAH-02-08-10	2	13.82	1.28
5. B5-UNI-SMAH-02-08-10	3	24.91	5.97
5. B5-UNI-SMAH-02-08-10	4	18.00	**
5. B5-UNI-SMAH-02-08-10	5	22.65	5.93
5. B5-UNI-SMAH-02-13-10	1	21.57	0.77
** Data not recorded			

4. Discussion

A number of factors can explain the discrepancy between experiment and analysis. These are outlined below.

1. Delamination of the joint – without proper bonding techniques, SMA can delaminate from the polymer matrix. While significant delamination was not found after single cycle tests, the SMA began pulling away from the matrix after a small number (<5) of cycles. In this case, not all SMA wires will provide contraction in the joint, and the specimen will eventually fail. This delamination induced by shear is addressed in the Appendix.
2. Excess heating of the SMA or SMP – due to the inability to precisely instrument the core of the joint with a series of thermocouples, it is impossible to instantaneously know the full temperature profile of the joint during heating. This shortcoming, coupled with more complex 3-d thermal modeling than is accounted for in the 1-d model, can lead to diminishing of shape memory properties.

3. Specimen variability in joint geometry – the small scale of the joint makes performance very sensitive to mold tolerancing errors, as SMA and shim layers out of place even 0.001" can have a significant impact on bending moments generated. This is addressed in Section 4.1.
4. Specimen variability in material properties – while all parts used in the joint were commercial off-the-shelf (COTS), the SMP resin had to be assembled on-site, leading to variations in stiffness. This is addressed in Section 4.2.

In total, a number of issues are persistent in the fabrication of Active Rigidity samples. Instrumentation, precision, and material variations must all be addressed before joint performance can improve.

4.1. Geometry Variability

As mentioned above, joint layering was subject to variation for each specimen. The microscopy image of Figure 5.9 shows that for the unimorph configuration with 8 parallel SMA wires, there is slight variability in SMA placement, and the location of the wires is can not yet be precisely controlled. While the intended placement was at half of the distance between surface and centerline for a ρ value of 0.5, or 1/32" above the bottom face. In the specimen presented, the SMA averages a placement at ρ=0.544, and the shim is placed at approximately 0.45(t_B). As with the resin stiffness, although variability cannot be controlled at this time, it can be incorporated into the model in explaining joint behavior.

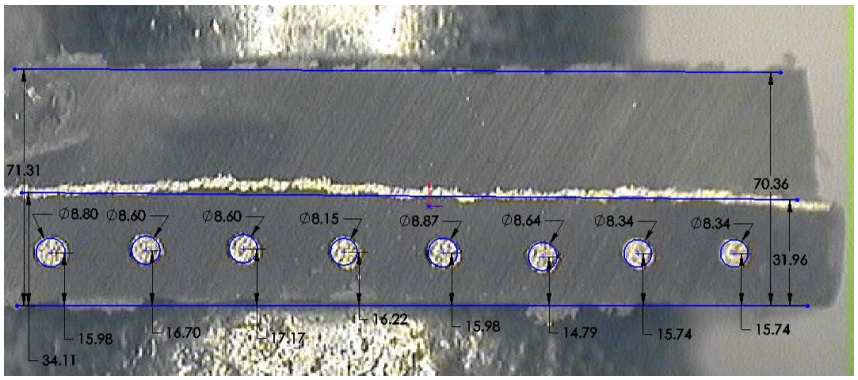

Figure 5.9 - Measuring SMA and shim location post-fabrication. Exact placement of these elements varied between specimens due to fabrication imprecision. Scale used is arbitrary; total joint thickness is 0.125”

4.2. Resin variability

Although the formulation of SMP used has a manufacturer quoted stiffness of 600 MPa in the cooled regime, the process by which the SMP is cured has significant impacts on actual sample characteristics. To confirm this and better inform the analytical model, a series of 3-point bending tests were conducted on multiple samples using an Instron MTS 858 Mini Bionix mechanical test system. Tests were conducted using available samples, and were cycled in the elastic regime at a variety of strain rates ranging from 50 mN/s to 1 N/s. The results in Table 5.5 are presented after samples have undergone an initial preconditioning, and use the standard equation for extracting flexural stiffness E_f from 3-point tests:

$$E_f = \frac{L^3 m}{4 b d^3} \tag{6}$$

where L is the support span, m is the slope of the load-deflection curve, d is the joint thickness, and b is the joint width. Results show that the bimorph specimen created on-site at the manufacturer’s facility (“CRG bimorph”) had a flexural modulus above

500 MPa regardless of strain rate, while other specimens of both pure SMP and SMP with embedded SMA demonstrated a modulus range of 222 to 436 MPa. As would be expected, the slower strain rates lead to lower flexural stiffness due to the material's viscoelastic properties.

Table 5.5 – Sample stiffness values from mechanical testing

Sample Description	**Shim Thick, Type**	**E (MPa)**	
		dε/dt = 100 mN/s	**dε/dt = 500 mN/s**
CU Unimorph 1*	.005", 1/8" holes	391	436
CU Unimorph 3**	.003", 1/8" holes	355	376
CU Unimorph 4**	.003", grooved	270	295
CU Unimorph 5**	.002", grooved	222	258
CU Pure SMP	None	295	349
CRG Bimorph	None	526	556
* Preconditioned different from other samples ** Incomplete fill (bubbles)			

Variations in material handling, precision in the mold curing process, and age of the resin are all important factors in the creation of specimens in the lab environment, which is not outfitted for the high volume of production necessary for stringent quality control. Instead, knowledge of the reduced value for flexural stiffness can be fed into the analytical model of Equations (4) and (5), providing more accurate data for the model. These modified values were used in preparing Table 5.2.

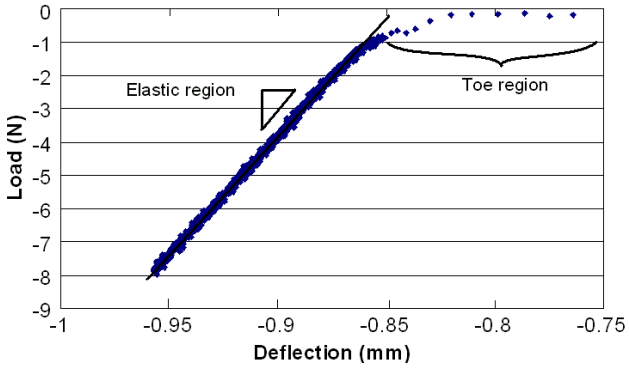

Figure 5.10 – Representative loading curve from mechanical testing of CU Pure SMP sample at 5 mN/s (chosen for display purposes only, not used in calculations), showing toe and elastic regions. Corresponding flexural stiffness at this strain rate was 138 MPa.

5. Conclusions

The Active Rigidity joint demonstrates functional performance in low cycle test environments, with consistently more than 10 degrees of tip angle deflection through heating over a 1" long specimen. Unloaded joint specimens are shown to demonstrate performance similar to a simplified analytical model using steady-state thermal and structural conditions. However, variability between samples, uncertainty in material properties, and a complex thermal model all add additional complexity not addressed in analysis, yielding experimental results that do not agree completely with predictions. A large fraction of heated deflection is lost upon cooling, requiring further study and additional refinement to determine the discrepancy sources between prediction and experiment. With greater control of fabrication processes and a more thorough analysis of material and transient thermal properties, the joint may hold potential for additional deflection more closely matching expected behavior, suitable for deployment as an induced strain actuator system.

REFERENCES

1. Abe, K., Uchino, K., and Nomura, S. 1982. "The Electrostrictive Unimorph for Displacement Control". *Jap. J. Appl. Phys.* 21: 1408-1410.
2. Brown, J. and Hodgson, D. 2000. Using Nitinol Alloys. Shape Memory Applications, Inc.
3. Crawley, E. and de Luis, J. 1987. "Use of Piezoelectric Actuators as Elements of Intelligent Structures". *AIAA* 25: 1373-1385.
4. Mabe, J., Ruggeri, R., Rosenzweig, E. and Yu, C. 2004. "Nitinol Performance Characterization and Rotary Actuator Design". Proc. *SPIE* Volume 5388 95: 95-109.
5. Manzo, J. 2006. "Analysis and design of a hyper-elliptical cambered span morphing aircraft wing". Masters Thesis, Cornell University, Ithaca, NY.
6. Manzo, J. and Garcia, E. 2009a. "Methodology for Design of an Active Rigidity Joint". *J. Int. Mater. Sys. Struct.* 20: 311- 327.
7. Manzo, J. and Garcia, E. 2009b. "Analysis and Optimization of the Active rigidity joint". *Smart Mater. Struct.* In review.
8. Olmsted, B. and Davis, M. 2001. Practical Injection Molding. Marcel Dekker, Inc. New York. Pgs. 70-71, 144-145.
9. Strelec, J., Lagoudas, D., Khan, M., and Yen, J. 2003. "Design and Implementation of a Shape Memory Alloy Actuated Reconfigurable Airfoil." *J. Intell. Mater. Sys. Struct.* 14: 257-273.

CHAPTER 5 APPENDIX

The joint mold consists of four parts – two side plates with the outer dimensions of the joint in relief, and two top plates with holes for the wires to pass through. A loom is placed behind this mold such that the SMA and nichrome wires can be aligned and properly tensioned in the mold cavity. Once wired, the mold is sealed and Veriflex SMP resin is injected into the cavity, which then cures with embedded SMA and nichrome wires. Photographs of an early generation mold in Figure 5.12 and Figure 5.13 illustrate wiring and injection processes, respectively. The mold requires alignment between loom and the cavity part set to orient wiring and eliminate air gaps and flashing.

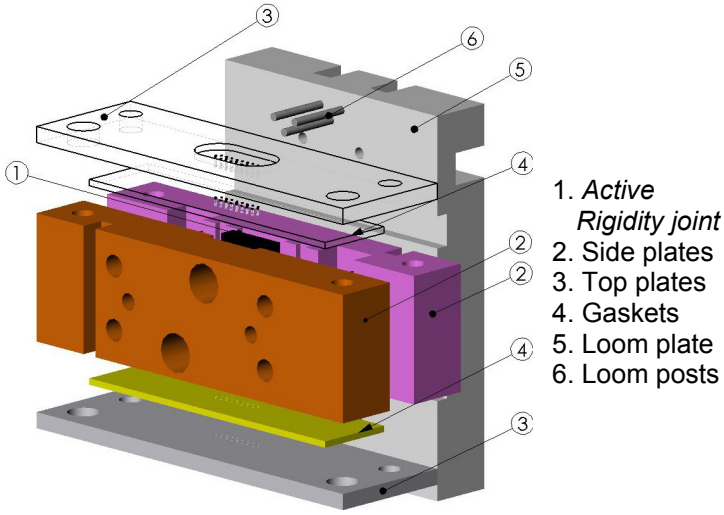

Figure 5.11 – Active rigidity joint mold parts, exploded and annotated by component

Many precautions must be taken when using the mold. SMP resin must cure in a closed mold environment, requiring no vapors to escape to achieve correct material properties. In addition, wiring of the SMA and nichrome layers must be kept both

aligned and electrically isolated from each other, requiring precise manufacture of top plates with sub-millimeter hole diameters.

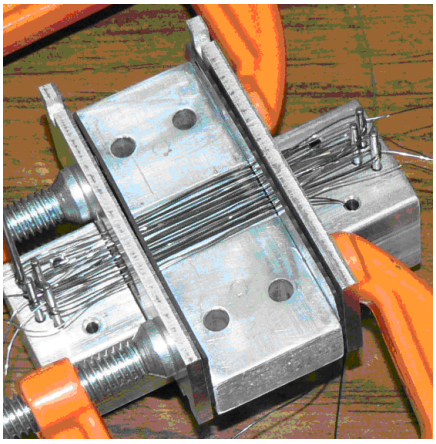

Figure 5.12 – Unsealed loom assembly for wiring active rigidity joint test specimens

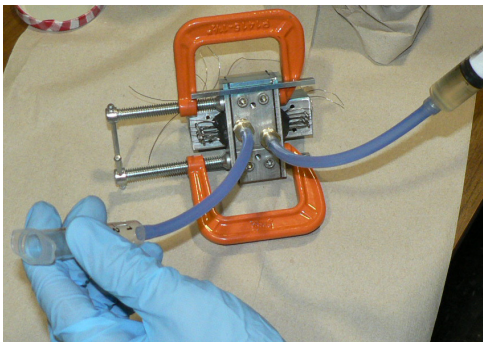

Figure 5.13 – Closed mold showing injection ports for filling active rigidity joint cavity

Resin cures over a 24 hour cycle at constant 75 deg. C. When pouring resin, it is important to prevent the formation of air bubbles. By increasing resin and mold temperature to just below the curing temperature at 70 deg. C, decreasing injection speed to 5 mL/min, and agitating the mold during filling, failed specimen output has decreased significantly (Olmsted and Davis, 2001). The progression of cured specimens is shown in Figure 5.14, tracking improvements from incomplete pours through successful results.

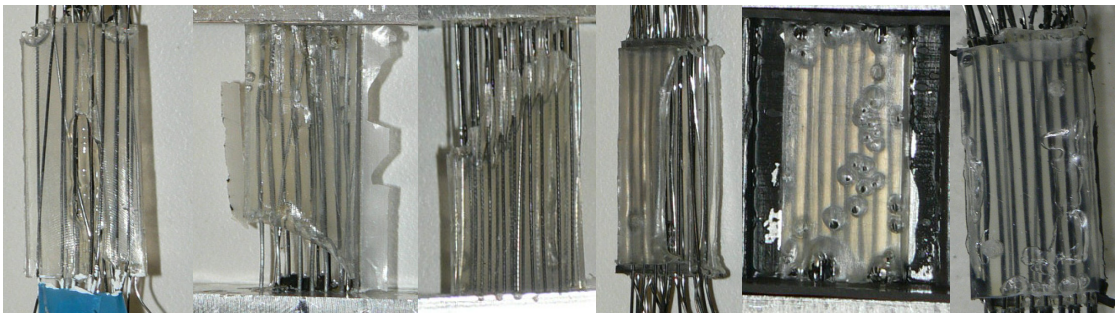

Figure 5.14 – Various problems associated with specimen creation. From left to right: wire misalignment, flashing, leakage, inconsistent filling, air bubbles, surface quality

Finite element assumption verification

Analytical models focus on solid prismatic elements, or slabs, adhered as composite layers. In reality, joint construction uses commercially available nichrome and SMA wires with cross-sectional areas matched to slab-based analytical equivalents. To consider physical assembly issues, an FEA model representative of this wire-based SMA and nichrome system is examined. Making use of the 20-node SOLID95 element given its midside nodes, and with MESH200 elements for creating finer detail on circular areas, the model is designed with a distribution of ten evenly spaced 0.010" diameter SMA wires embedded beneath the structure surface at an embedded depth of 16% half-thickness (x_4 = 0.8392), equivalent in cross-sectional area to a slab of thickness 0.0016" (x_1), with three nichrome wires of diameter 0.0113" (x_3 = 0.0006") and SMP accounting for the remainder of a 1/8" thick structure (x_2 = 0.0606"), similar but not identical to the fabricated model. Because elements no longer occur as thin sheets with aspect ratio violations, the amount of elements and nodes is reduced from a slab-based model, to 31,000 elements and 81,000 nodes. Only heated phase is predicted in this ANSYS model, and large-scale deformations are disabled.

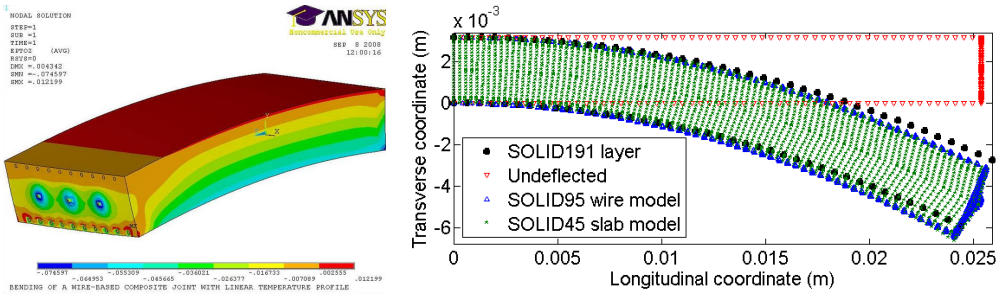

Figure 5.15 – SOLID95 wire-based model for the case of SMA and nichrome filaments embedded in an SMP matrix. Mechanical strain results (left) and deflection comparison to layered model (right)

Results are shown in Figure 5.15, comparing wire model (triangle markers, outline only) with slab-based layered (SOLID191, large black dots) and solid (SOLID45, small asterisks) models. Deflection agrees identically with the SOLID45 slab-based model in profile, confirming accuracy of the slab assumption. Analytical slab-based solution expects angular deflection of 23.6 degrees in the heated phase without external moment. By comparison, the wire- and solid slab-based FEA models both predict a tip angle of 24.2 degrees, and the similarly designed SOLID191 layered solid model predicts a tip angle of 24.5 degrees.

The wire model provides insight into delaminating forces encountered during actuation, informing construction and adhesion methods. Wire model results show local shear stresses on the polymer matrix, with shear strains on the order of 120% (50 degrees shear angle) local to the nichrome and a peak shear stress between 3 and 5.6 MPa. The high shearing angles of the wire model may prohibit composite action in the shape memory polymer by inducing delamination local to embedded wires. An increased number of smaller wires, distributed along the beam width, will reduce some shear.